N O T I C E

THIS DOCUMENT HAS BEEN REPRODUCED FROM MICROFICHE. ALTHOUGH IT IS RECOGNIZED THAT CERTAIN PORTIONS ARE ILLEGIBLE, IT IS BEING RELEASED IN THE INTEREST OF MAKING AVAILABLE AS MUCH INFORMATION AS POSSIBLE

NASA CR- 166705

8103-07
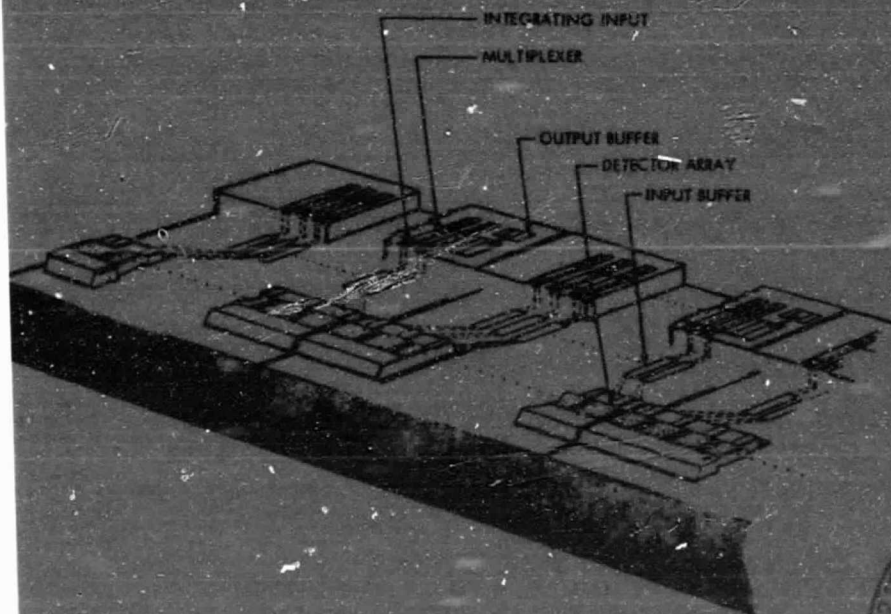
THERMAL INFRARED ARRAY

PHASE I

FINAL REPORT

- INTEGRATING INPUT
- MULTIPLEXER
- OUTPUT BUFFER
- DETECTOR ARRAY
- INPUT BUFFER

Volume I—Technical

Honeywell

THERMAL INFRARED ARRAY

PHASE I

FINAL REPORT

Volume I--Technical

26 March 1981

Prepared for

National Aeronautics and Space Administration
Goddard Space Flight Center
Greenbelt, Maryland

Honeywell

ELECTRO-OPTICS OPERATIONS
2 Forbes Rd.
Lexington, MA 02173

TABLE OF CONTENTS

LIST OF ILLUSTRATIONS

LIST OF ILLUSTRATIONS (Continued)

LIST OF TABLES

EXECUTIVE SUMMARY

The TIRA focal plane is a 1000 element linear pushbroom system, for application to LEO and SEOS imaging missions in the 10 to 12 μm band. The array is composed of many modules, each module containing 64 detector channels, with each detector coupled to a bipolar buffer which is itself coupled to a CCD readout multiplexer. The base substrate will contain the bipolar buffers and support both the (Hg,Cd)Te detectors on one side and the CCD multiplexer mounted on the other. The entire module is designed for edge butting along three sides, with one side free to attach wire bonds to the focal plane. The total width of the module, transverse to the scan direction, is 256 mils.

During Phase I of the TIRA program, the proposed module design was reviewed and revised. Two different module designs have been considered. The first and simplest design incorporates a single row of 64-(4 mil)^2 contiguous detectors. Totally evaporated leads (TELs) will be used to interconnect each detector to a bipolar buffer and the buffer to an individual CCD input. The second design requires two rows of detectors for TDI purposes, each with its own bipolar buffer and separate input channel into the CCD. The density of this configuration is double that of the first design even though the TDI operation will be performed off the module.

The recommended design configuration for the TIRA focal plane array will consists of 32 modules; the complete configuration is built by butting together two 1024 linear arrays. Each of the linear arrays are formed by edge butting 16 modules together. By staggering the modules of the two rows, the channel outages which occur where the modules are edge butted can be eliminated. Two stage TDI operation is performed by the post processing electronics, which reduces the design complexity of the focal plane. Optimal performance is expected for detectors with high impedances. For a 500 Ω detector a detectivity of 2.2×10^{10} cm-Hz$^{1/2}$/W is expected for 2 TDI at 105 K.

Both the photodiode and the bipolar buffer performance at 105 K were examined during Phase I. The model quantitatively describing diffusion and G-R current photodiode limits was revised to properly account for the three dimensional diode geometry. The absorption coefficient near the bandgap was used to better determine the alloy composition and intrinsic carrier concentration. Detailed characterizations were completed on four existing photodiode arrays having the TIRA junction area of 10^{-4} cm^2 and a range of cutoff wavelengths. Emphasis was placed on operation at 105 K. Both R_0 and I-V characteristics were fitted using our quantitative model to obtain self-consistent values of the various diode parameters. Noise spectra were taken on all diodes at zero bias and over a range of reverse biases; they were related to our quantitative model.

The measured values of R_0 for the photodiode array closest to the TIRA wavelength of 12.5 μm are about a factor of 2 to 3 lower than the 500 Ω required. Our quantitative model was used to explore various approaches to increase this diffusion limited R_0 to reach this program requirement. The analysis indicates that a value of 500 Ω for R_0 should be attainable by implementation of any one of three improvements: (1) slight increase in p side acceptor concentration, (2) increase in electron diffusion length along with geometrical modificaiton, and (3) slight reduction in operating temperature below 105 K. All three are additive. Designing the junction area to be smaller than the optical area was considered, but was shown by numerical solution of the geometrical dependence to provide no significant advantage for system detectivity. Slight reduction in the design cutoff wavelength was also considered. It was shown to increase the system detectivity due to an increase in R_0, but to provide no significant advantage in the system signal-to-noise ratio because of reduction in the collected photons.

The measured values of 1/f noise of the photodiode array closest to the TIRA wavelength of 12.5 μm are close to the program requirements. The reported correlation of this 1/f noise to the surface G-R current I_{GR} was used to suggest an upper bound to I_{GR}. Our analysis indicates that low enough G-R current may just be achieved to meet the 1/f noise specifications using our best surface processing techniques. Additional safety margin will result from implementation of any one of three improvements: (1) reduction in

8103-07

detector bias by laser trimming the buffer transistors, (2) slight increase in system chopping frequency, and (3) slight reduction in operating temperature below 105 K.

Noise voltage and noise current measurements as a function of temperature were also performed on a variety of bipolar devices, both from commercially available sources and from Honeywell standard processes. None of the devices measured both met all the noise requirements as well as the design rules for the TIRA module. However, sufficient information was gathered to indicate that a multiple emitter standard process device, with laser trimming of the emitter resistor, should be suitable for TIRA.

The thrust of the TIRA Phase I study was to design the focal plane array. However, system studies were included to investigate whether the LEO and SEOS missions would impose conflicting requirements on the focal plane design, to determine whether any specifications would result in unachievable requirements, and to insure that a sensor could be designed at a later time utilizing the TIRA focal plane design. The subsystems which were singled out as central to achieving a TIRA sensor capability were optics, system MTF, chopping (with calibration insertion), and focal plane cooling.

The conclusions resulting from these system studies are:

- A single focal plane design will satisfy both mission configurations.

- Optical designs are available which will meet the mission goals.

- MTF can be traded with optical complexity in a future study.

- A chopping mechanism can be devised which will modulate radiation to a 4 inch focal plane as well as insert two calibration sources at the required frequencies for chopping and calibration.

8103-07

- Radiative cooling technology should be suitable for a future
  TIRA sensor in either mission configuration.

- Cold shielding is not a requirement but may be desirable.

This report constitutes the technical summary of design work completed during Phase I of the TIRA contract. Phase II management and test plans, as well as cost and schedule projections are covered separately in Volume 2.

8103-07

SECTION 1
TIRA FPA DESIGN

1.1 GENERAL DESCRIPTION

The TIRA focal plane is a 1000 element linear pushbroom system, composed of many modules which will be edge-butted together. Each module will contain 64 detector channels, with each detector coupled to a bipolar buffer which is itself coupled to a CCD readout multiplexer. Figure 1-1 depicts the conceptual design for the FPA module. The base substrate will contain the bipolar buffers and support both the (Hg,Cd)Te detectors on one side and the CCD multiplexer mounted on the other. The entire module is designed for edge butting along three sides, with one side free to attach wire bonds to the focal plane. The total width of the module, transverse to the scan direction, is 255 mils.
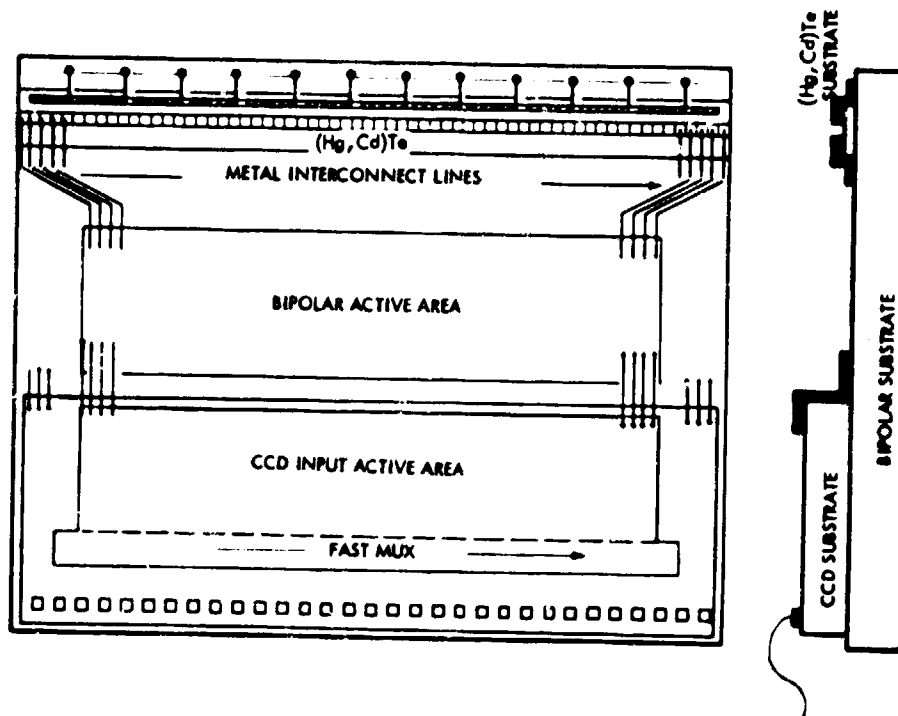
Figure 1-1. TIRA FPA Module Layout

Table 1-1 summarizes the proposed TIRA FPA design. As a design goal a (Hg,Cd)Te PV diode array of $R_0 = 500$ Ω is assumed, which is diffusion limited at 105 K. The cutoff wavelength value will dictate the degree of difficulty in fabricating actual devices of the above specifications. The diode is operated at near zero bias ($|V_b| < 1$ mV) for low 1/f noise. A common base bipolar buffer stage is proposed between the (Hg,Cd)Te array and the CCD input. The emitter resistors could potentially be laser trimmed to ensure the diode zero bias condition ($|V_b| < 0.1$ mV). Experimental data on the Honeywell bipolar transistor for integrated circuit use have shown the feasibility of such a buffer stage. The buffer output is AC coupled to the input gate of the CCD multiplexer. The gate is occasionally reset by a MOSFET transistor for DC restoration and calibration.

Table 1-1. TIRA FPA DESIGN SUMMARY

- (Hg,Cd)Te PV Diode Array

    $R_0 = 500$ Ω @ 105 K, diffusion limited

    $D^* = 2.1 \times 10^{10}$ cm-Hz$^{1/2}$/W with $\eta = 0.7$; zero bias for low 1/f noise

- Bipolar Buffer

    Common base

    Emitter resistor laser trimmed for zero bias PV

- CCD Multiplexer

    AC coupled

    Resettable gate for DC restoration

    No TDI on chip

    100 μm pitch

- TIRA FPA

    $D^* = 1.4 \times 10^{10}$ cm-Hz$^{1/2}$/W @ 105 K @ 100 Hz
    Power dissipation 140 mW/1000 elements

The initial CCD design is based on zero TDI and 100 μm pitch; two TDI can be achieved by off-chip multiplexing. The initial TIRA FPA design predicts a D^* value of 1.4×10^{10} cm-Hz$^{1/2}$/W at 105 K at 100 Hz. Total power dissipation has been calculated to be 140 mW for a 1 x 1000 detector array.

Figure 1-2 illustrates the detector performance as a function of the zero bias resistance assuming a variety of quantum efficiency values. By arbitrarily setting the TIRA FPA design goal at $D^* = 1.0 \times 10^{10}$ cm-Hz$^{1/2}$/W, Figure 1-2 graphically illustrates the margin of degradation the preamp/CCD may contribute. After a design exercise, one readily discovers that the higher the detector zero bias resistance, the smaller the noise contribution from the preamplifier.

An electrical schematic of the bipolar/CCD coupling scheme is shown in Figure 1-3. The connections represented by a circle, such as V_E, V_b, V, etc, are common to all elements in a module. Ideally, the emitter resistance is individually trimmed to ensure zero bias voltage across the detectors.

Two different module designs have been considered. The first and simplest design incorporates a single row of 64-(4 mil)^2 contiguous detectors. As indicated in Figure 1-1, totally evaporated leads (TELs) will be used to interconnect each detector to a bipolar buffer and the buffer to an individual CCD input. The second design requires two rows of detectors for TDI purposes, each with its own bipolar buffer and separate input channel into the CCD. The density of this configuration is double that of the first design even though the TDI operation will be performed off the module. These two module configurations will be elaborated upon in a later section.

The next section presents the design tradeoff using a noise model for the coupled system. Section 2.3 summarizes the design considerations for a system with two TDI stages and addresses the suitability of the modules as well. The device descriptions for the detectors, bipolars, and CCDs are given in Section 2 and are based on modeling analyses and laboratory measurements obtained from off-the-shelf devices.

1-3

8103-07
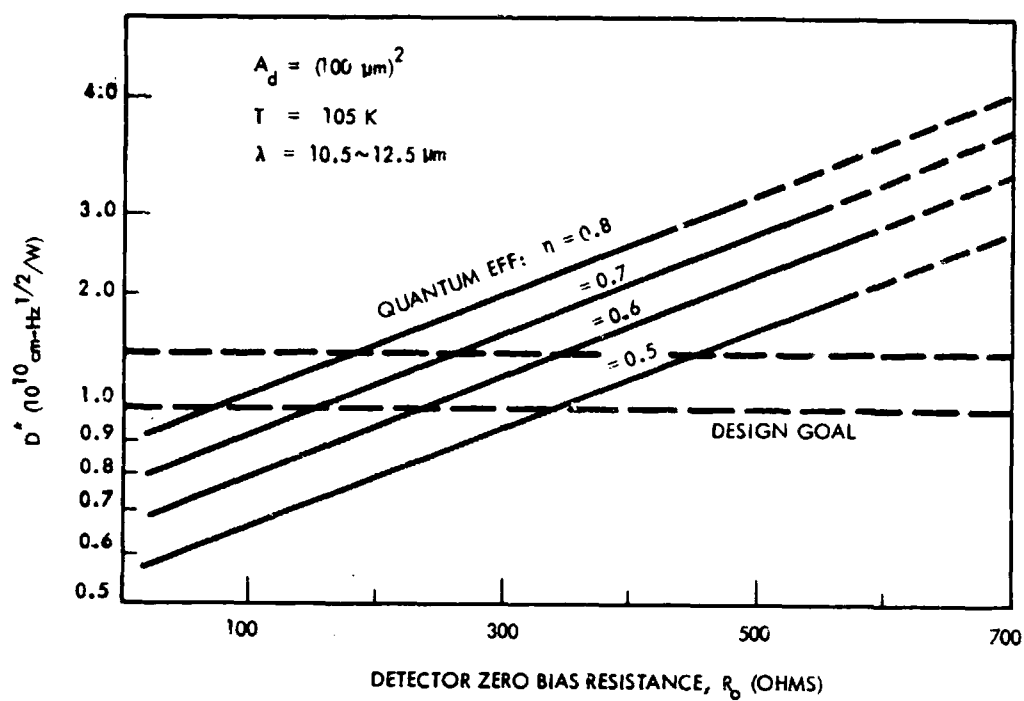
Figure 1-2.   Thermal Detectivity Versus R_0 at 105 K
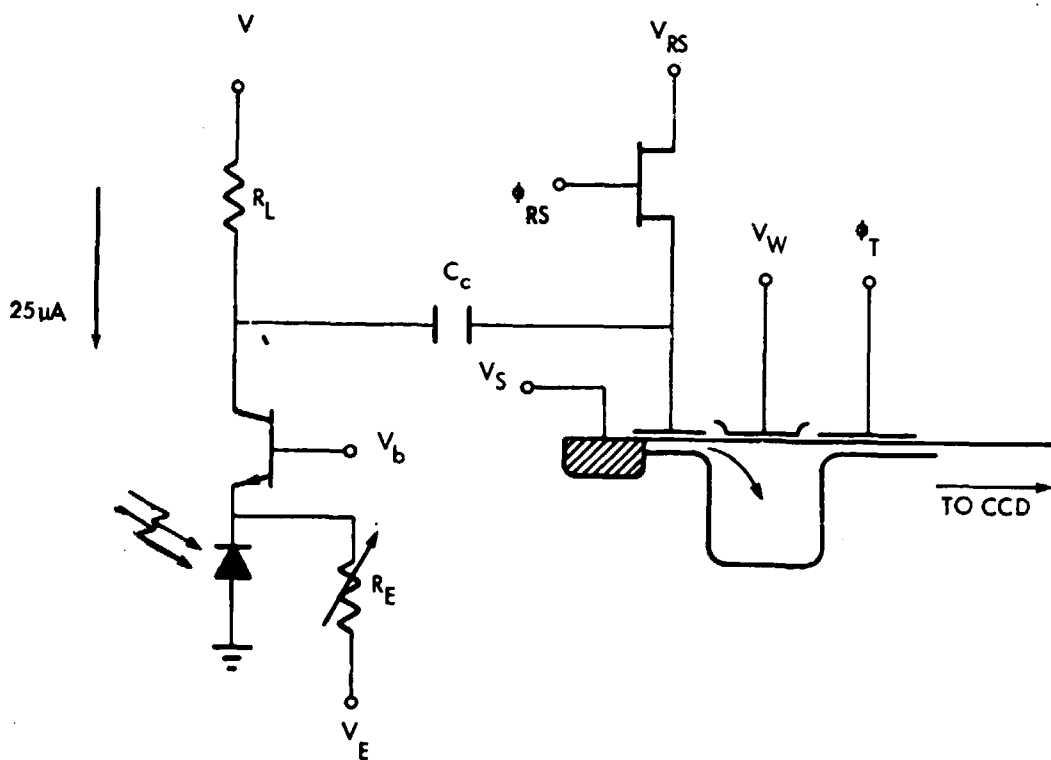
Figure 1-3.   AC Gate Coupled Input Circuit with a Bipolar Buffer

1.2   TIRA FPA DESIGN TRADEOFF

A design tradeoff for the (Hg,Cd)Te/bipolar/CCD coupled system will be presented in this section based on a model to predict performance as a function of the interrelationships of the focal plane parameters. One important measure of focal plane performance is the detectivity, which is dependent on the total noise of the system

$$D^* = \frac{R_i \, (A_d N_{TDI})^{1/2}}{i_{EQ}} \tag{1-1}$$

where

$$R_i = \frac{q \eta \lambda}{hc} = \text{current responsivity (amp/W)}$$

$$A_d = \text{detector area (cm}^2\text{)}$$

$$N_{TDI} = \text{number of TDI stages}$$

$$i_{EQ} = \text{equivalent input referred noise (amp/Hz}^{1/2}\text{)}$$

A second performance measure is the noise figure of the system, which is the ratio of i_{EQ} to the detector thermal limited noise

$$NF \equiv \frac{i_{EQ}}{i_d} = \frac{i_{EQ}}{[4kT/R_0]^{1/2}} > 1 \tag{1-2}$$

A low noise figure indicates a diode limited system.

To determine the performance measures, the equivalent input referred noise of the system must be properly modeled. This noise model is presented below and is followed by several design criteria which will be used to determine suitable focal plane parameters for a low noise figure system.

Some of the major insights obtained from the focal plane model are

- Lowering the base resistance of the bipolar buffer from 150 Ω to 50 Ω results in only a 6 to 8 per cent improvement in detectivity.

8103-07

- CCD noise figure is inversely related to the CCD operating current.

- As the load resistor R_c on the collector is increased, the CCD noise figure will decrease, resulting in a minimum system noise figure at about $R_c = 200$ k Ω.

- Without increasing the power requirement, the focal plane performance will fall off more quickly as the detector resistance decreases than would be expected for a theoretical detector.

- Low detector resistances require higher operating power for equivalent coupling efficiency.

1.2.1 TIRA Noise Model

An equivalent noise model for a single channel in the TIRA focal plane is presented in Figure 1-4. This model is consistent with a bipolar buffer whose emitter is coupled to the detector. The signal at the collector is AC gate coupled to the input MOSFET of the CCD.

The diode noise current is merely the Johnson noise generated in a zero bias detector with resistance R_0:

$$ i_d^2 = 4\ kT/R_o $$

The bipolar noise sources are separated into voltage and current noise terms which can be readily measured in the laboratory:

$$ e_B{}^2 = 4\ kT\ R_B + 2q\ I_B\ R_B{}^2 + \frac{2\ k^2 T^2}{q\ I_c} + \frac{2q\ f_L\ I_B R_B{}^2}{f} $$

$$ i_B{}^2 = 2q\ I_B + \frac{2q f_L I_B}{f} $$

1-6
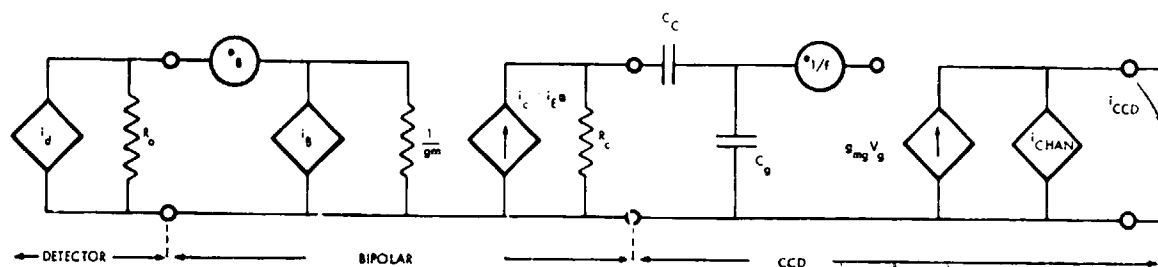
Figure 1-4.   TIRA Detector/Bipolar/CCD Input Noise Model

where:

T = temperature (K)

R_B = base resistance (Ω)

I_B = base current (amps) = I_C/β

I_C = collector current (amps)

f_L = process dependent parameter for 1/f noise

f = frequency (Hz)

     The first term in the expression for noise voltage is the thermal noise associated with the base resistance.   The next two terms are the shot noise associated with the base and collector, respectively.   The last term represents the one-over-frequency dependent noise source.   The two terms in the noise current expression are the shot noise on the base and a frequency dependent term.

8103-07   1-7

Due to the low collector currents, on the order of 40 µA, at which the buffer will be operating, the dominant transistor noise will be a voltage noise represented by:

$$e_B^2 = 4kTR_B + \frac{2(kT)^2}{q\,I_c} + \frac{2qf_L\,I_B(R_B + R_o)^2}{f} \quad .$$

(1-3)

The CCD noise sources are distinguished by a 1/f noise voltage source on the gate and a thermal noise generated across the channel.

$$e_{1/f}^2 = \frac{\gamma kT}{C_{ox}^2 A_g f^{0.84}}$$

$$i_{CHAN}^2 = 2\,mkT\,g_{ms} = 2q\,I_{CCD}$$

where

γ = Process dependent parameter which varies from 50 to 500 pF/cm^2 on Honeywell devices. Typical values are around 200 pF/cm^2.

C_{ox} = Capacitance of the gate oxide (fd/cm^2)

A_g = Area of gate (cm^2)

g_{ms} = Source transconductance. For subthreshold operator g_{ms} = q I_{CCD}/mkT, where the derating factor, m, is typically 1.2.

The equivalent noise at the diode is,

$$i_{EQ}^2 = i_d^2 + \frac{e_B^2}{R_o^2} + \frac{1}{A_i^2}\quad i_{CHAN}^2 + e_{1/f}^2\,g_{mg}^2$$

(1-4)

The current gain, A_i from the diode to the CCD channel is

$$A_i = \frac{g_m R_o\,\alpha\,R_c}{1 + g_m R_o}\left(\frac{C_c}{C_c + C_g}\right)g_{mg}$$

where

$$g_m = \left.\frac{\partial I_E}{\partial V_E}\right|_{V_B} = \text{emitter transconductance}$$

$\alpha = I_E/I_C = $ Ratio of emitter to collector current

$R_C = $ the load resistor on the collector

$C_C = $ AC coupling capacitor

$C_g = $ Gate capacitance

$g_{mg} = \dfrac{q\, I_{CCD}}{n_g\, kT} = $ CCD gate transconductance where the derating factor n_g is typically 1.6.

This noise model has been used to determine the TIRA focal plane design rules which are presented below.

1.2.2   Bipolar Buffer Design Rules

A good bipolar buffer design for TIRA depends on

1) A low bipolar Noise Figure
2) Low power dissipation

Ideally, the detector thermal noise should be greater than the noise generated by the buffer for a low noise buffer system. By ignoring the bipolar 1/f contribution, this criterion becomes

$$4kTR_o > 4kTR_B + \frac{2\,(kT)^2}{q\,I_c}$$

1-9

The inequality is satisfied for high collector currents and base resistances less than the detectors resistance. Figure 1-5 is a plot of the noise voltage contribution of the bipolar buffer as a function of collector current for
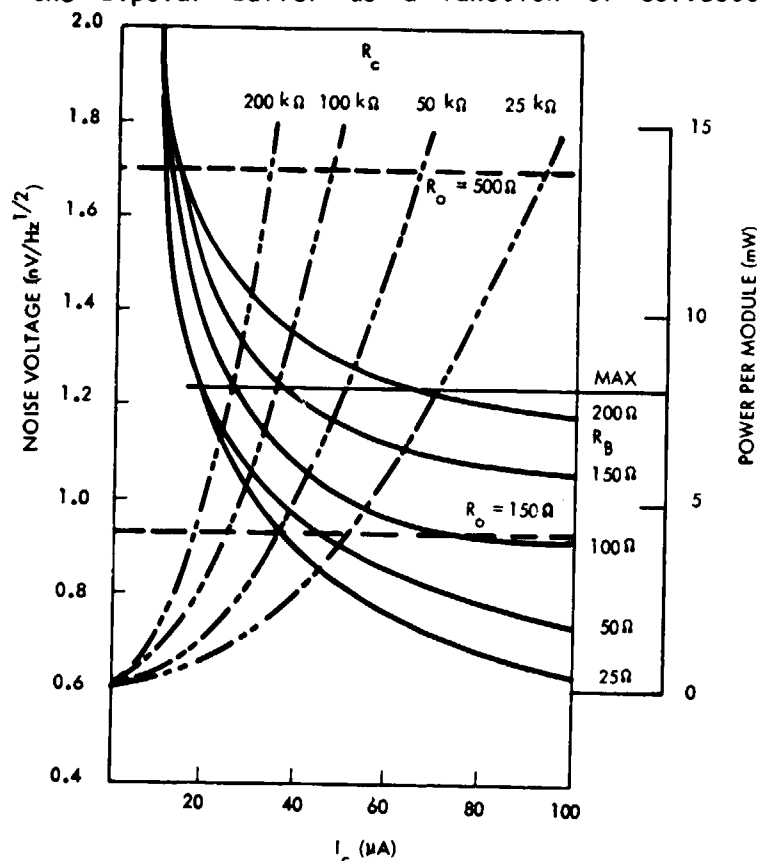
Figure 1-5. Bipolar Buffer Design Curves

different values of base resistance. At low collector current the shot noise in the emitter dominates the buffer noise, whereas at high current levels the thermal noise in the base becomes the limiting noise factor. At sufficiently high current levels the 1/f noise in the bipolar will dominate.

Also shown in Figure 1-5 are the voltage noise levels associated with a 150 Ω and 500 Ω detector. As long as the buffer noise is less than the detector noise, a good noise figure for the buffer is assured. A buffer noise figure of 1.4 indicates that the buffer noise is equal to the detector noise.

The second criterion for the bipolar buffer design must be low power dissipation; otherwise the cooling system will be unduly taxed. The major

source of power dissipation for the focal plane is due to the collector current flowing through the load resistor, R_c. A realistic upper limit for the focal plane is around 130 mW or roughly 8 mW per module containing 64 channels (260 mW for a system with two TDI stages). A plot of power dissipation for a module as a function of collector current for different values of R_c is over-layed on Figure 1-5. Note the horizontal line indicating the 8 mW power limit.

These two design criteria limit the bipolar buffer design, especially when coupled to a low impedance detector. For a 150 Ω detector the base resistance must be less than 100 Ω, but if power requirements are taken into account using a reasonable value of R_c = 50 kΩ, a base resistance of about 50 Ω is desired for a low noise buffer.

Values for R_c are determined from the CCD coupling criteria discussed in the next section. However, as a rule, the higher the resistance R_c, the lower the CCD noise figure will be, which is contrary to the desire for low power dissipation.

1.2.3 CCD Design Rules

To design a low noise CCD input stage for the TIRA focal plane the CCD noise contribution must be less than the thermal noise generated in the detector. This criterion leads to the following inequality:

$$\frac{i^2_{CHAN}}{g^2_{mg}} + e^2_{1/f} < i^2_d A^2_i$$

or

$$\frac{2n^2_g (kT)^2}{q \, I_{CCD}} + \frac{\gamma kT}{C^2_{ox} A_q f} < \frac{4kTR^2_c}{R_o} \left(\frac{I_c/I_{SAT}}{1 + I_c/\alpha I_{SAT}} \right)^2 \left(\frac{C_c}{C_c + C_g} \right)^2$$

1-11

where $I_{SAT} = kT/qR_0$ is the diode saturation current, I_c is the collector current, and I_{CCD} the current in the CCD. The terms on the lefthand side of the inequality represent the total noise voltage on the CCD gate. The terms on the righthand side represent an equivalent noise voltage as seen by the CCD due to the thermal noise generated in the detector. It would be a simple matter to make the righthand term large by increasing either R_c or I_c were it not for for the limitations placeed on the focal plane power requirements.

Figures 1-6 and 1-7 are based on the terms in the above inequality for detector resistances of 150 Ω and 500 Ω respectively. Other CCD parameters used to generate the figures are:

$$\gamma = 200 \text{ pfd/cm}^2$$
$$C_{ox} = 6.28\times10^{-8} \text{ F/cm}^2$$
$$A_g = 6.4\times10^{-5} \text{ cm}^2$$
$$n_g = 1.6$$
$$T = 105\text{K}$$
$$\alpha = 1.0$$
$$C_c/(C_c + C_g) = 1.0$$

Solid lines represent the CCD noise terms with several lines drawn to represent the channel noise at various CCD currents. As the current increasesthe channel noise contribution decrease. An upper limit to the CCD current is set by the CCD charge capacity. A realistic maximum CCD current is about 6 nA.

The dashed lines in the figures represent the detector noise as seen at the CCD input gate. The values for R_c and I_c were chosen to obtain a power dissipation of 8 mW per module. Lowering I_c levels (to ease the power requirements) will cause the equivalent detector noise voltage level to decrease, resulting in a higher CCD noise figure.

1.2.4   Optimized Designs

Judicious use of the design curves in Figures 1-5, 1-6 and 1-7 can be used to design a low noise focal plane for TIRA. To illustrate, consider a

8103-07   1-12
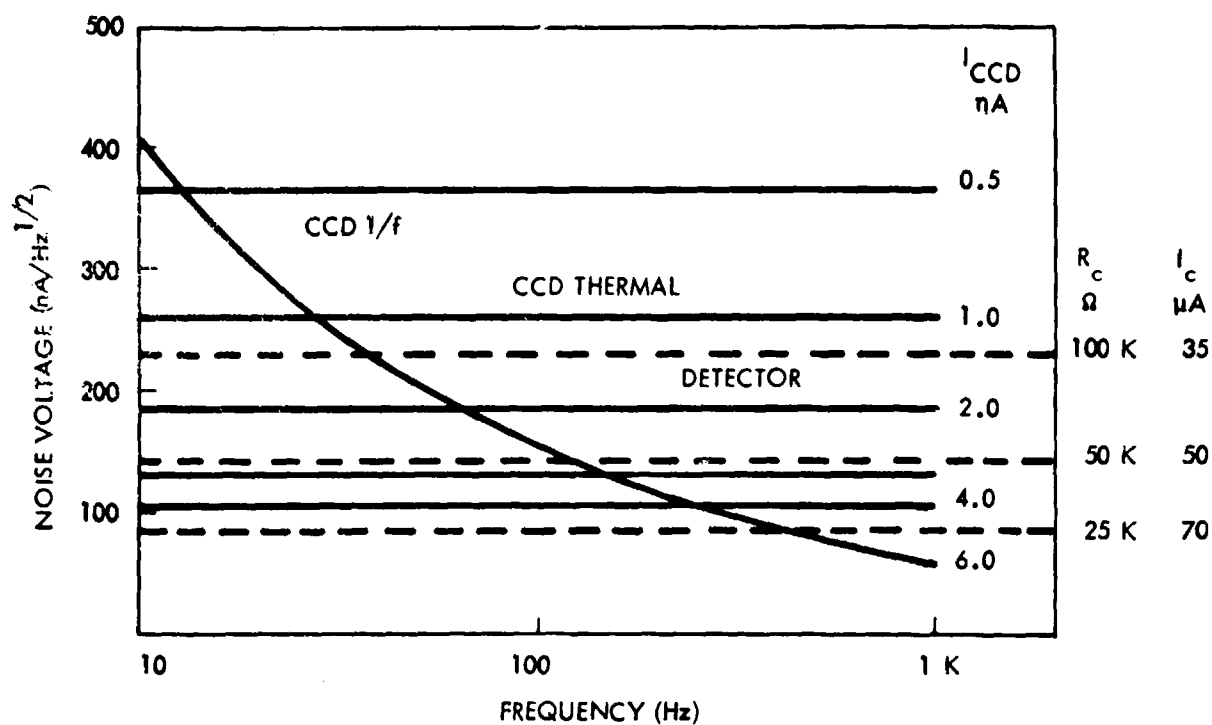
Figure 1-6. CCD Design Curve for $R_0 = 150 \ \Omega$
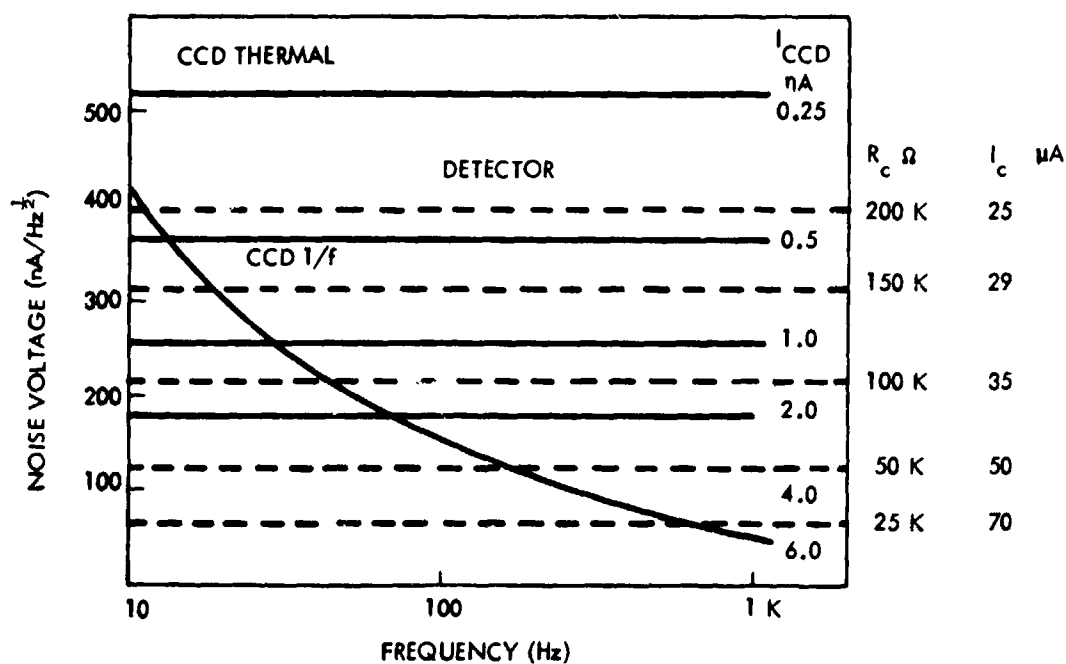
Figure 1-7. CCD Design Curves for $R_0 = 500 \ \Omega$

500 Ω detector with a 100 kΩ load resistor R_C. Figure 1-7 indicates that the CCD can operate at a current level of 4 nA for a CCD noise figure of NF_{CCD} = 1.37. The bipolar buffer design curves predict a bipolar noise figure of NF_B = 1.20 for a transistor with a base resistance of 100 Ω. The overall noise figure for this focal plane with R_0 = 500 Ω is NF = 1.52 to yield a detectively of 1.4 x 10^{10} cmHz$^{1/2}$/W. Total power dissipation will be 8 mW per 64 channel module.

In a similar fashion the design rules of the preceeding sections were used to generate the performance Tables 1-2 and 1-3 for detector resistances of 500 Ω and 150 Ω respectively. The noise figure for the CCD was determined assuming a CCD current of 4 nA and at a chopping rate of 100 Hz. The buffer noise figures are the minimum expected to limit the power dissipation to 8 mW.

The tables demonstrate that as the load resistor, R_C, increases, the CCD noise figure decreases, whereas just the reverse occurs for the buffer noise figure. The total noise figure for the coupled system, which is determined by combining the two separate noise figures, exhibits a minimum for R_C values between 100 kΩ and 400 kΩ.

Also, the lower the base resistance the better the performance of the system. However the improvement is small. Only a 6 to 8 percent improvement is achieved by decreasing the base resistance from 150 to 50 Ω. A realizable base resistance of 100 Ω is the design goal for TIRA.

Normally the theoretical detectively of the focal plane will vary inversely with the square root of the detector resistance. But as the two tables indicate, an additional degradation will result due to the coupling network, which is examplified by the total system noise figure. For a 150 Ω detector and a focal plane optimized for an R_0 = 500 Ω, using R_C = 200 kΩ, an additional 30% degradation in detectivity will be incurred due to the coupling network alone.

To circumvent this additional loss in performance due to the coupling network, additional power must be consumed by the focal plane. Again

8103-07   1-14

Table 1-2. PERFORMANCE FOR A 150 Ω DETECTOR

R_B (Ω)	R_C (kΩ)	NF_{CCD} @4.0 nA 100 Hz	NF_B	Total NF	D^*_{CHAN} ($\times 10^{10}$ cm Hz$^{1/2}$/W)
50	25	2.61	1.33	2.75	
	50	1.75	1.39	2.00	0.60
	100	1.33	1.47	1.71	0.70
	200	1.14	1.56	1.71	0.70
	400	1.06	1.74	1.78	0.67
	800	1.03	1.93	1.94	0.62
100	50	1.75	1.51	2.08	0.58
	100	1.33	1.56	1.79	0.67
	200	1.14	1.69	1.78	0.67
	400	1.06	1.84	1.8	0.64
	800	1.03	2.02	2.03	0.59
150	50	1.75	1.61	2.16	0.55
	100	1.33	1.69	1.90	0.63
	200	1.14	1.80	1.88	0.64
	400	1.06	1.93	1.96	0.61
	800	1.03	2.10	2.11	0.57

Optimum Design

$R_B = 100$ Ω $R_C = 200$ kΩ $I_C = 25$ μA   P = 8 mW/Module

$I_{CCD} = 4$nA $NF_{CCD} = 1.14$ $NF_B = 1.69$ NF = 1.78

$D^* = 0.67 \times 10^{10}$ cm Hz$^{1/2}$/W

1-15

Table 1-3. PERFORMANCE FOR A 500 Ω DETECTOR

R_B (Ω)	R_C (kΩ)	NF_{CCD} @4.0 nA 100 Hz	NF_B	Total NF	D^*_{chan} ($\times 10^{10}$ cm Hz$^{1/2}$/W)
50	50	1.90	1.13	1.97	1.05
	100	1.36	1.16	1.48	1.40
	200	1.12	1.20	1.30	1.60
	400	1.04	1.27	1.30	1.60
	800	1.01	1.35	1.36	1.53
100	50	1.90	1.16	1.99	1.04
	100	1.36	1.20	1.52	1.37
	200	1.12	1.25	1.35	1.54
	400	1.04	1.31	1.34	1.55
	800	1.01	1.39	1.40	1.49
150	50	1.90	1.21	2.02	1.03
	100	1.36	1.24	1.55	1.34
	200	1.12	1.29	1.39	1.50
	400	1.04	1.35	1.38	1.51
	800	1.01	1.42	1.43	1.45

Optimum Design

$R_B = 100$ Ω $R_C = 200$ kΩ $I_C = 25$ µA P = 8 mW/Module

$I_{CCD} = 4$nA $NF_{CCD} = 1.12$ $NF_B = 1.25$ NF = 1.35

$D^* = 1.54 \times 10^{10}$ cmHz$^{1/2}$/W

1-16

8103-07

consider the optimum design described above for the 500 Ω detector. This system achieves a coupling noise figure of 1.35. To achieve the same coupling efficiency for a 150 Ω detector I_c must be increased, causing the focal plane power consumption to nearly doubled from 8 mW to 14 mW per module.

1.3 TIRA FPA CONFIGURATION

1.3.1 FPA Configuration For 2 TDI Stages

Several focal plane configurations have been considered for TIRA to provide two stages of time-delay-and-integration (TDI). With two TDI stages the number of channel outages can be minimized. The two most promising focal plane configurations are summarized in Table 1-4. The first configuration is composed of a double row of modules with each module containing a single row of

Table 1-4. TIRA FPA CONFIGURATION FOR 2 TDI

	DOUBLE ROW OF MODULES	SINGLE ROW OF MODULES
No. of Detector/Module	64	128 - (2 x 64)
TDI Operation	Off Chip	Off Chip
Module Design	Simple	Complex - double multiplexing
Module Yield	Good	Fair
Power Consumption/Module	8 mW	16 mW
Modules/FP	32	16
Channel Outages	Minimal	Nominal
Multi-Spectral FP Compatibility	Poor	Good
Module Butting	Back edge between module rows	Two sides at ends of module
Butting Yield	Good	Fair

8103-07

1-17

detectors as shown in Figure 1-8. The second design calls for a single row of modules with each module containing a double row of detectors (2 x 64) as shown in Figure 1-9.

Both configurations are designed to have the TDI operation performed off the module by the processing electronics. However, the first configuration is expected to have the highest yield at the lowest cost because only 64 detectors are required, each with its own bipolar buffer and CCD input channel, on a 256 mil wide module. The second configuration is more complex, requiring twice as many detector channels on the same size module. Furthermore the number of channel outages can be minimized in the first design configuration by staggering the modules.

Unfortunately, it should be noted that close butting to an adjacent focal plane (with different spectral band) is more difficult with the first design since bonding wires are attached to both sides of the focal plane. On the other hand, the second design is more compatible with a multispectral focal plane system; however butting of the modules edges together becomes more complex and will reduce overall yield.

Power consumption for the two focal plane configurations will be the same. The first design uses 8 mW per module as opposed to 16 mW for the other, but requires twice as many modules in the focal plane.

1.3.2   Buttability

Minimum distance between active detector areas when two modules are butted together is crucial to TIRA focal plane structure. The minimum distance for the (Hg,Cd)Te active area to be diamond saw cut is approximately 20 μm without significantly affecting performance. Hence, a safety margin of about 80 μm of dead space must be allowed where two modules are butted together. Thus, the second configuration, which requires modules to be butted along their sides, will experience one channel dropout at each place where the modules will be butted together, for a minimum of 16 missing channels on the focal plane.

8103-07   1-18

Single Row Modules/Double Row Detectors (TDI Off Chip)
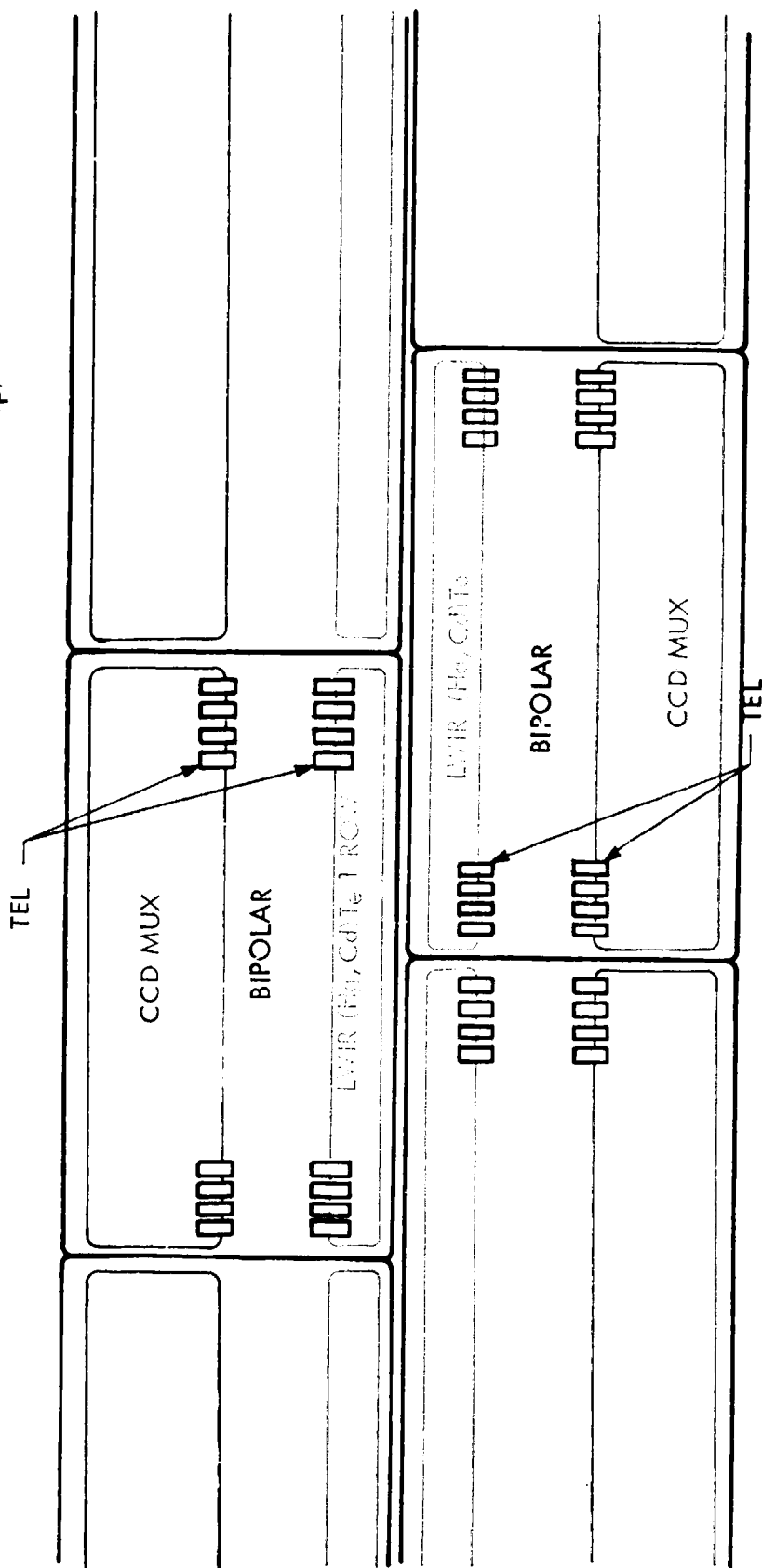
Figure 1-8. Recommded 2 TDI TIRA Focal Plane Configurations

Double Row Modules/Single Row Detectors (TDI Off Chip)

LWIR (H₉CₙTe 2 ROW)

CCD MUX
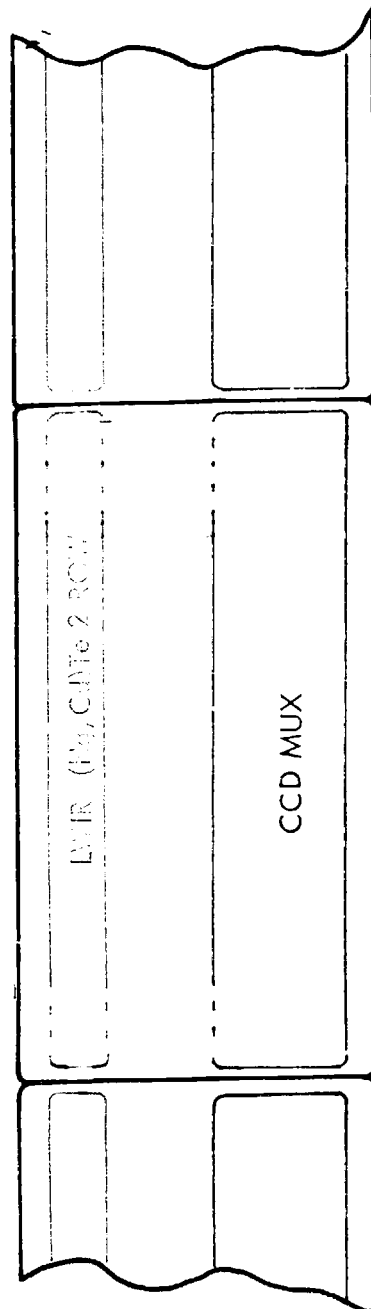
Figure 1-9. Optional 2 TDI TIRA Focal Plane Configurations

The first configuration can circumvent the butting restriction altogether. By staggering the modules with respect to one another, several detector channel widths can be allowed to separate the modules butted along their side edges; the staggered module in the second row will cover the gap. Also, since the configuration is designed for TDI operation, the separation between the two rows must be less than 10 IFOV, which is clearly satisfied by the 80 μm butting tolerance. The desire for zero channel dropout definitely favors the first FPA configuration.

1.3.3 Curved Versus Flat Focal Plane

The total focal plane length will be four inches. Depending on the final sensor optics, it may be necessary to configure the array along a curved focal plane rather than holding it flat. The curvature could be accomplished in a piecewise linear fashion, where four modules are butted together on a common carrier board, which is itself mounted onto a conformal master board. Although this approach has been considered for TIRA, Honeywell has not yet studied such a conformal focal plane system.

1.4 TIRA FPA DESIGN SUMMARY

The recommended design configuration for the TIRA focal plane array will consists of 32 modules each containing a linear array of 64 detectors contiguously arranged on 4 mil centers. The complete configurations is built by butting together two 1024 linear arrays. Each of the linear arrays are formed by edge butting 16 modules together. By staggering the modules, the channel outages which occur where the modules are edge butted can be eliminated. The base substrate for each module contains the bipolar buffer array and supports both the (Hg,Cd)Te detector array and the CCD multiplexer. TEL's will be used to interconnect bipolar buffers to the detectors and CCD inputs. Table 1-5 summarizes the important focal plane specification and lists the expected performance for a 150 Ω and a 500 Ω detector. Two stage TDI operation is performed by the post processing electronics, which reduces the design complexity of the focal plane. Optimal performance is expected for detectors with high impedances. For a 500 Ω detector a detectivity of 2.2×10^{10} cm $Hz^{1/2}/W$ is expected for 2 TDI at 105 K.

8103-07

Table 1-5. TIRA FOCAL PLANE SUMMARY

Focal Plane Configuration	2 x 1024
Number of Modules	32
Detectors/Module	64
Detector dimensions	$(4 \times 4)\text{mil}^2$
Operating Temperature	105 K

Bipolar Buffer (at 105 K)

Structure	NPN - Common Base
	Multible emmitters
β	20
R_B	100 Ω
R_C	200 kΩ implanted
R_E	3.5 - 10 kΩ Laser Trimmable
	Chrome/silicon Thin film
I_C	25 μA

CCD Multiplexer

Input Configuration	-AC Gate Coupled
	-Gate Reset MOSFET
	-Surface Channel
	-No TDI
Multiplexer	-2ϕ Buried Channel
Coupling Capacitor	3 to 5 times C_g
I_{CCD} (nominal)	4 nA
Integration Time	2.5 ms
Charge Capacity	10^8 electrons

FPA Power Requirements		280 mW
Detector R_0	150 Ω	500 Ω
Noise Figure	1.8	1.35
Detectivity (No TDI)	0.67×10^{10}	1.5×10^{10} cm-Hz$^{1/2}$/W
(2 TDI)	0.95×10^{10}	2.2×10^{10} cm-Hz$^{1/2}$/W

SECTION 2
TIRA MODULE DEVICES

2.1   PHOTODIODE DETECTORS

Recent 8 to 12 µm (Hg,Cd)Te diode development efforts have indicated that 12.5 µm cutoff diodes operating between 70 K and 105 K could have R_0A products large enough to meet the proposed detectivity D^* if operated at zero bias, assuming no photodiode 1/f noise existed. Coupling to the CCD array, however, requires that the diodes be operated at some reverse bias, resulting in considerable 1/f noise from the diodes. This diode 1/f noise is correlated with surface generation-recombination (G-R) currents which, for 10^{-4} cm^2 diodes, would limit the D^* at the suggested chopping frequency of 40 Hz. Operation of the photodiodes closer to zero bias greatly reduces the difficulty in attaining the desired surface G-R current and associated 1/f noise.

The performance of a detector is usually characterized by its detectivity D^*, which is the signal to noise ratio normalized to unit area and unit incident power. It can be expressed by

$$D^* = \frac{R_i \sqrt{A}}{i_{EQ}} \qquad (2-1)$$

where R_i is the current responsivity, A is the optical area, and i_{EQ} is the equivalent noise current density. The responsivity is determined by the quantum efficiency η and wavelength λ, and is given by

$$R_i = \frac{\eta q \lambda}{hc} \qquad (2-2)$$

where h,c, and q have their standard values.

The noise sources contributing to the equivalent noise current density are background induced noise current, Johnson noise due to the junction resistance R_0, 1/f noise $i_{1/f}$ and the noise associated with the buffer amplifier. These combine to give

$$i_{EQ}^2 = 2 \eta q^2 \phi_B A + \frac{4kT}{R_0} + i_{1/f}^2 + i_n^2 \text{ (amp)} \qquad (2\text{-}3)$$

where ϕ_B is the background flux and k is Boltzmann's constant.

2.1.1   Photodiode Diffusion and G-R Currents

Currents resulting from several mechanisms may limit n^+ on p photodiode performance for any given temperature and cutoff wavelength. Although the forward and reverse currents cancel for the mechanism at zero bias, the associated noise does not.[1] At higher temperatures performance may be limited either by diffusion of thermally generated current, bulk space G-R current, or surface G-R current. This section demonstrates how to distinguish the three currents using their characteristic temperature and voltage dependences.

At higher temperatures the dominant current arises from diffusion of thermally generated electrons from the p-side of the junction and thermally generated holes from the n-side to the junction. This so-called diffusion current is proportional to the number of minority carriers on each side of the junction. Since the volume from which diffusion current may arise is much larger on the p-side than on the n-side and the number of minority carriers is much larger, the diffusion currents for n^+ on p photodiodes are almost all from the p-side. The diffusion current I_D and zero bias impedance R_0 can be expressed in the planar approximation as:[2]

1.   A. Van der Ziel, Advances in Electronics and Electron Devices. Vol. 46, Edited by L. Marton, Academic Press (New York, 1978), p. 313.

2.   W. Shockley, Bell System Tech. J. 28, (1949).

2-2

8103-07

$$I_D = I_{SAT}(e^{qV/kT}-1) \qquad (2-4)$$

$$I_{SAT} = A_J \frac{q^2}{kT} \frac{n_i^2}{N_A} \frac{\mu_e}{L_e} \qquad (2-5)$$

$$R_0 \text{ (diff)} = \frac{kT}{qI_{SAT}} \qquad (2-6)$$

where A_J = junction area

n_i = intrinsic carrier concentration

N_A = acceptor concentration

L_e = minority carrier electron diffusion length

μ_e = minority carrier electron mobility

τ_e = minority carrier lifetime

A second current mechanism results from thermal generation and recombination (G-R) of electron-hole pairs in the region of the junction between the n and p sides which is depleted of both types of minority carriers. This so-called space charge G-R current is proportional to the intrinsic carrier concentration n_i. This G-R current and associated limitation to R_0 are given by:[3]

$$I_{GR} = I_{OGR} \frac{2 \sinh (qV/2kT)}{\sqrt{1 - V/V_{bi}}} \ f(b) \qquad (2-7)$$

$$R_0 \text{ (G-R)} = \frac{kT}{qI_{OGR}f(b)} \qquad (2-8)$$

---

3.   C.T. Sah, R.N. Noyce, and W. Shockley, Proce. IRE 45, 1228 (1957).

2-3

where

$$b = e^{-qV/kT} \cosh \varepsilon_t \qquad (2\text{-}9)$$

$$f(b) = \int_0^\infty \frac{du}{1 + 2bu + u^2} \qquad (2\text{-}10)$$

Also

$$I_{OGR} = \frac{n_i W_o A_J}{\tau_o} \frac{kT}{V_{bi}} \qquad (2\text{-}11)$$

or

$$I_{OGR} = n_i S_o W_o P_J \frac{kT}{V_{bi}} \qquad (2\text{-}12)$$

for depletion layer or surface G-R, respectively. Here V_{bi} is the depletion built in voltage, W_0 is the depletion width as zero bias, $\tau_0 = \sqrt{\tau_{no} \tau_{po}}$ is the effective depletion layer lifetime, P_J is the junction perimeter, and S_0 is the surface recombination velocity inside the depletion region where it intersects the semiconductor surface. For the most effective G-R center, at zero bias $b = \cosh \varepsilon_t = 1$ and $f(b) = 1$.

The temperature dependences of both current mechanisms are almost entirely due to the intrinsic carrier concentration. Since $R_0 A$ (G-R) $\propto n_i^2$, performance should be limited by diffusion currents at higher temperature and at somewhat lower temperatures by generation-recombination currents. Since $n_i \propto \exp(-Eg/2kT)$ the transition temperature between diffusion current and G-R current limitation is inversely proportional to device cutoff wavelength λ_{co}.

2.1.2   PHOTODIODE MODEL REVISIONS

The model based on Equations (2-4) through (2-12) can be used to quantitatively describe the photodiode performance. Two significant revisions have been incorporated into the model to provide improved estimates of the

various photodiode tradeoffs. First, the actual diffusion current coming from the three dimensional volume surrounding the photodiodes is larger than the one dimensional planar approximation estimates. This effect is shown schematically in Figure 2-1. Numerical techniques were used to solve the appropriate

TOP VIEW

$A_J = 3 \times 3$ mil^2

$A_{OPT} = 4 \times 4$ mil^2
(MASKED)

3-D DIFFUSION MODEL   JUNCTION   MASK

1-D DIFFUSION MODEL

Figure 2-1. Schematic Photodiodes Configuration Showing Three Dimensional and One Dimensional Diffusion Current Models

partial differential equation for the case of circular n$^+$ on p photodiodes in order to properly correct for the three-dimensional geometry.[4] By incorporating this solution into the model as a correction, f_{3D}, to the planar approximation of diffusion current for various p-side thicknesses, Equation (2-5) becomes:

$$I_{SAT} = A_J \ \frac{q^2}{kT} \ \frac{n_i^2}{N_A} \ \frac{\mu_e}{L_e} \ f_{3D} \qquad (2-13)$$

4. R.J. Briggs, "Geometrical Dependence of Small Area Photodiode Photocurrent and Diffusion Current," Submitted for publication to the IRIS Specialty Group on Infrared Detectors, June 2-4, 1981.

2-5

8103-07

various photodiode tradeoffs. First, the actual diffusion current coming from the three dimensional volume surrounding the photodiodes is larger than the one dimensional planar approximation estimates. This effect is shown schematically in Figure 2-1. Numerical techniques were used to solve the appropriate

Figure 2-1. Schematic Photodiodes Configuration Showing Three Dimensional and One Dimensional Diffusion Current Models

partial differential equation for the case of circular n^+ on p photodiodes in order to properly correct for the three-dimensional geometry.[4] By incorporating this solution into the model as a correction, f_{3D}, to the planar approximation of diffusion current for various p-side thicknesses, Equation (2-5) becomes:

$$I_{SAT} = A_J \frac{q^2}{kT} \frac{n_i^2}{N_A} \frac{u_e}{L_e} f_{3D} \qquad (2\text{-}13)$$

4. R.J. Briggs, "Geometrical Dependence of Small Area Photodiode Photocurrent and Diffusion Current," Submitted for publication to the IRIS Specialty Group on Infrared Detectors, June 2-4, 1981.

8103-07

As a second revision, the bandgap is not taken simply as $E_G = hc/\lambda_{co}$, where λ_{co} is the cutoff wavelength. Instead the bandgap is determined by using the quantum efficiency expression of Van de Weil for front side illumination[5] to determine the absorption coefficient at which the photodiode quantum efficiency drops to 50% of its peak value and the absorption measurements of Finkman and Nemirovski to determine the actual bandgap.[6] The equation used to describe the quantum efficiency is:

$$\eta = \frac{\alpha L_e}{\alpha^2 L_e^2 - 1} \left[\alpha L_e - \frac{\sinh\,(d/L_e) + \alpha L_e e^{-\alpha d}}{\cosh\,(d/L_e)} \right]$$

where α = absorption coefficient

L_e = minority carrier diffusion length

d = p-side thickness

For consistency, the intrinsic carrier concentration is then determined using the reported measurements of the same authors.[7]

2.1.3   Detailed Characterization of 10^{-4} cm^2 Diodes for 105 K Operation

During the phase I investigation, the model described in the previous sections was compared with data on 10^{-4} cm^2 diodes for 105 K operation. Three forms of data were taken on the same diodes: zero-bias impedance as a function of temperature (R_0 vs T), dark current as a function of applied voltage (I-V) at 105 K, and dark noise current density as a function of reverse

5. F. Van De Weil, in Solid State Imaging, edited by P.G. Jespers, F. Van de Weil, and M.H. White, pp. 47-90, Noordhoff, Leyden.

6. E. Finkman and Y. Nemirovsky, "Infrared Optical Absorption in $Hg_{1-x}Cd_xTe$," J. Appl. Phys. 50, 4356 (1979).

7. Y. Nemirovsy and E. Finkmann, "Intrinsic Carrier Concentration of $Hg_{1-x}Cd_xTe$," J. Appl. Phys. 50, 8107 (1979).

bias at 105 K. On one array, with cutoff greater than 12.6 μm at 105 K, both noise and current-voltage characteristics were also measured at several other selected temperatures.

Figure 2-2 shows the range of observed noise current density at 105 K for four elements from each of four photodiode arrays,[8] which were selected because they have the same area as required by the program. The solid lines show the theoretical wavelength dependence. For convenience, the measured noise current densities have been converted to detector detectivities using the standard equations in the figure. For the purposes of this calculation, the first and last terms in the equivalent noise current expression (Equation 2-3) have been assumed to be small. The remaining terms correspond to the white noise from a detector of impedence R_0 and the 1/f noise. The figure also summarizes the range of observed zero-bias impedances for the four arrays at 105 K.

Figures 2-3 and 2-4 represent a comprehensive analysis of the temperature dependence of R_0 and I-V data taken on one of the recently measured 12.6 μm photodiodes. Figure 2-3 compares the temperature dependence of R_0 with the model fit. This model, described in the previous section, gives values for temperature-dependent diffusion and G-R current constants, I_{SAT} and I_{OGR}. These constants are used to generate diode I-V characteristics at a given temperature. Model and experimental values are compared in Figure 2-4 at four temperatures. Neglecting leakage currents, which become dominant at low temperatures, the diode's measured I-V characteristics are well described by the theory.

Alternatively, measured I-V behavior itself can be used to determine the values of I_{SAT} and I_{OGR}. Values of I_{SAT} and I_{OGR} data at the four different temperatures were listed in Figure 2-4. These same data are plotted in Figure 2-5, along with the theoretical temperature dependences taken from the R_0 model of Figure 2-3.

---

8. Photodiodes fabricated under NASA Johnson Space Center Contract NAS9-15250, "Moderate Temperature Detector Development, Phase IV."
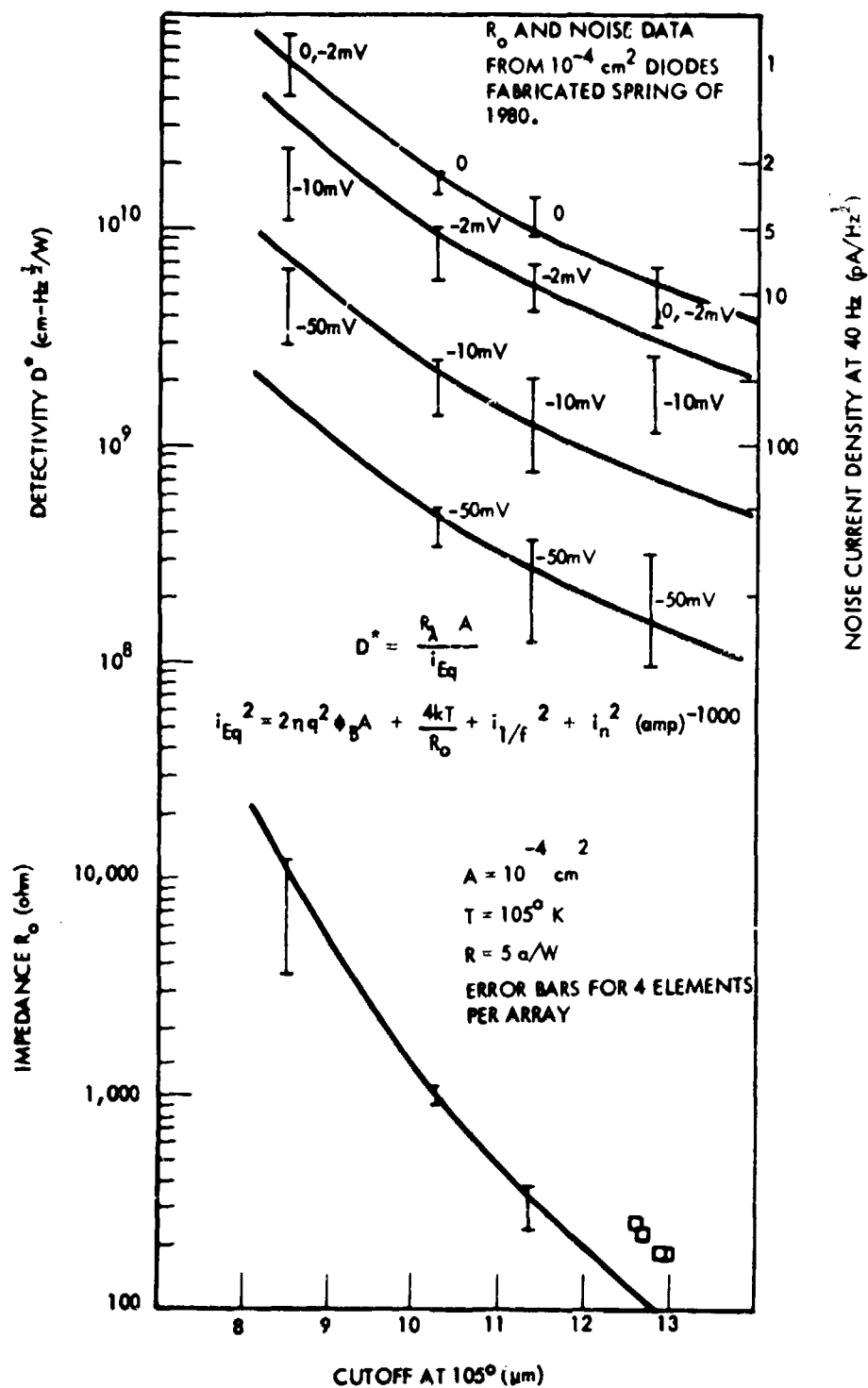
Figure 2-2. R_0 and Noise Data From 10^{-4} cm^2 Fabricated Spring of 1980. Error Bars Indicate Range of Selected Photodiodes measured.
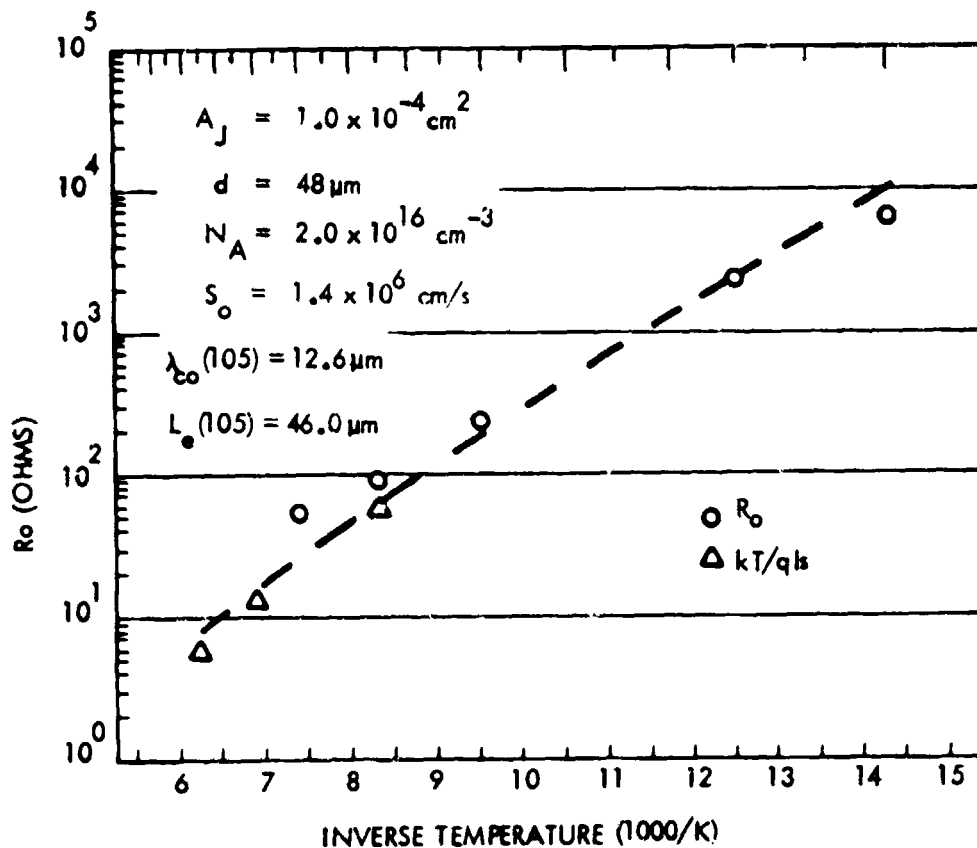
Figure 2-3. Zero-bias Impedance Temperature Dependence for 12.6 μm Photodiode with Model Parameters Indicated. Current Constants I_{SAT} and I_{OGR} Taken from This Model Were Used to Generate the Model I-V Curves of Figure 2-4.

This technique of using both the temperature dependence of R_0 as well as the diode current-voltage characteristics at various temperatures to determine the best model has been implemented on a computer for the first time under the TIRA program. This procedure provides a method of obtaining self-consistent values of diffusion length, surface recombination velocity, series resistance, and acceptor concentration. Modeling the I-V characteristics was found to be a more sensitive method to differentiate between diffusion, G-R, and leakage limited behavior than modeling only the temperature dependence of R_0. The values obtained from the I-V modeling are consistent with those determined from R_0 vs T modeling.

Figure 2-6 shows the noise spectra for a representative 12.6 μm diode at 105 K at several values of reverse bias. The various contributions are
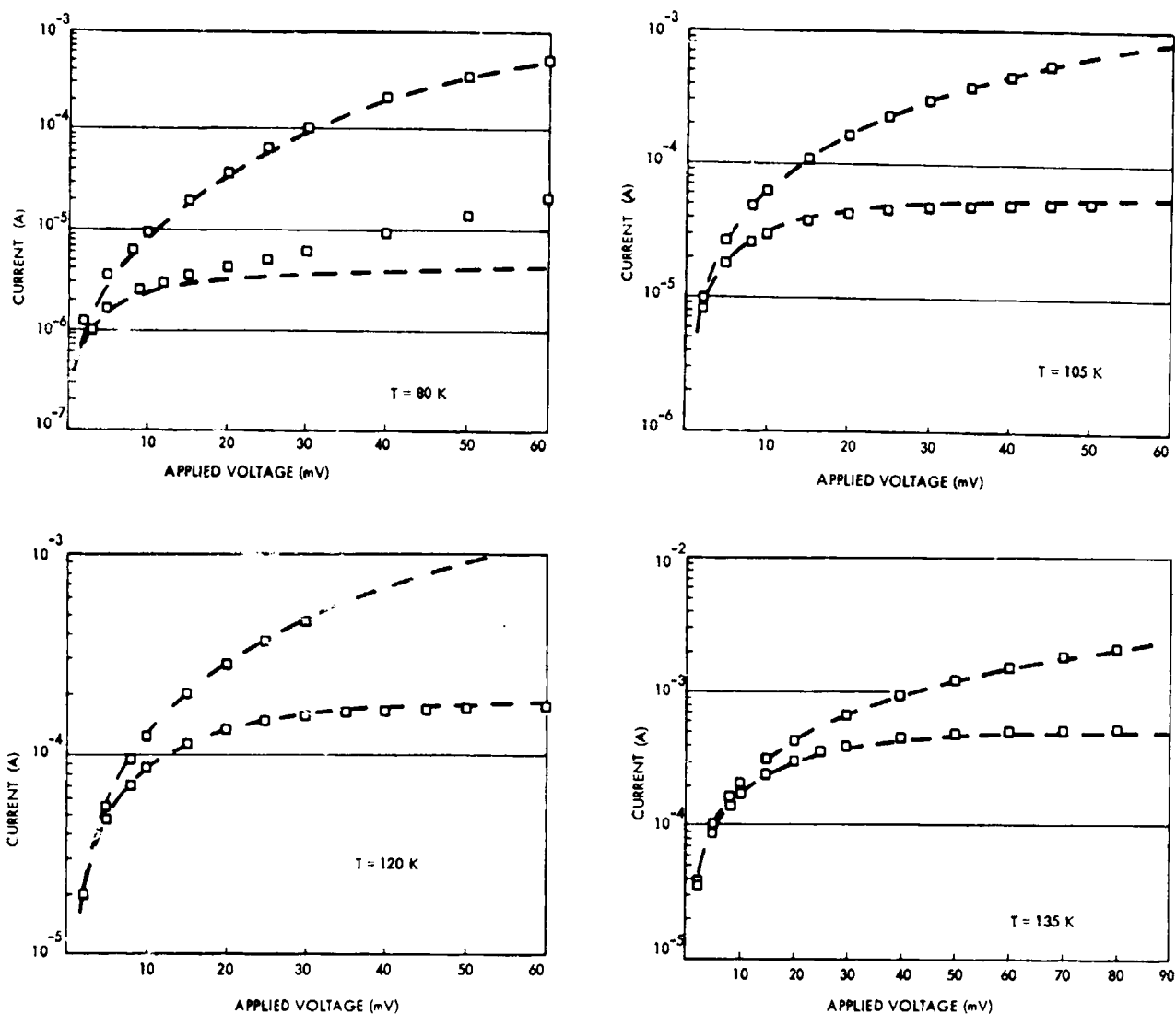
T(K)	$I_{SAT}(\mu A)$	$I_{OGR}(\mu A)$	$R_s(\Omega)$	ϵ_t	V_{bi} (mV)	$R_O(\Omega)$
80	2.27	0.539	45	0	102	2504
105	46.0	3.450	40	0	105	223
120	162.0	7.800	34	0	106	95
135	446.0	15.300	29	0	107	55

Figure 2-4. Current-voltage Characteristics for Measured 12.6 μm Photodiode
at Four Different Temperaturtes. Dashed Lines are the Model
Fits Using the Parameters Indicated
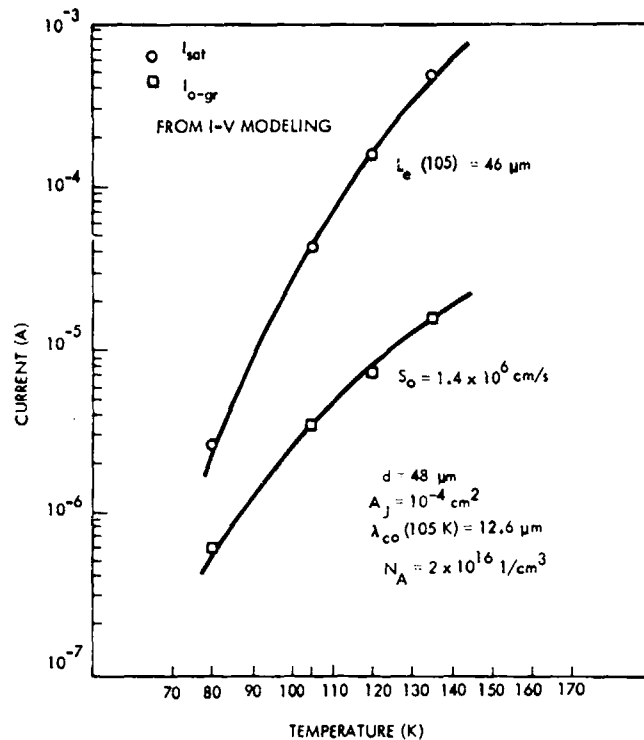
Figure 2-5. Temperature Dependence of Parameters I_{SAT} and I_{OGR} Used to Model the Current-Voltage Characteristics in Figure 2-4. Theoretical Temperature Dependences are Given by the Solid Lines.
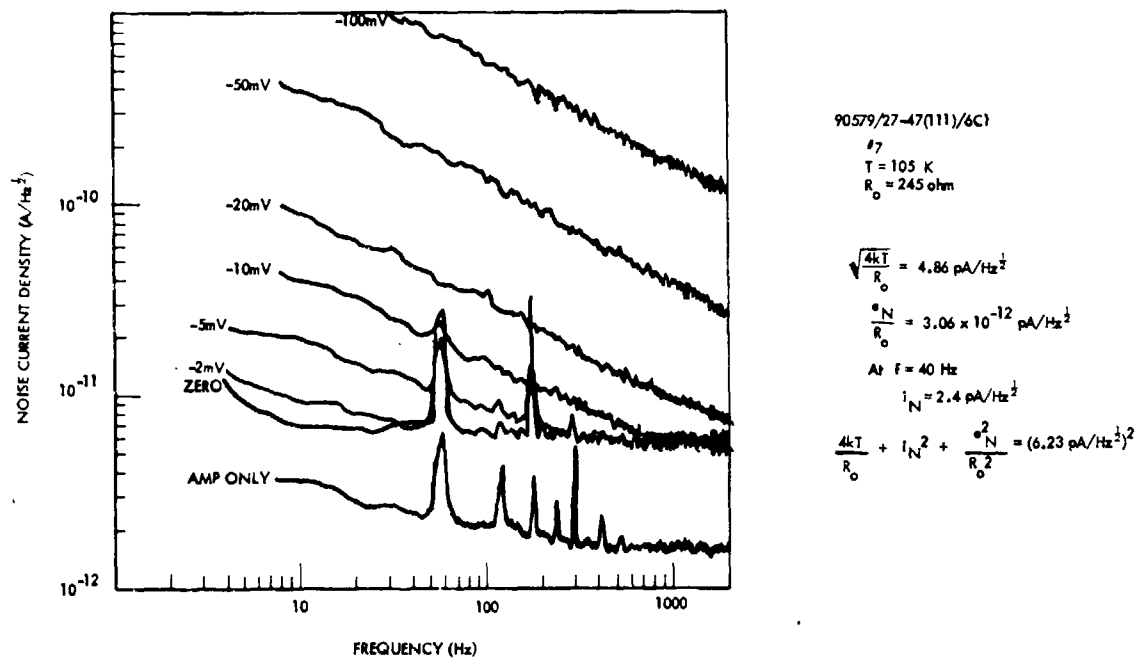
Figure 2-6. Noise Spectrum of 12.6 μm Photodiode at 105 K at Zero Bias and at Reverse Biases Indicated

indicated, and when added together in quadrature, correctly account for the observed total noise current density. Notice that the detector itself has a white noise of only 4.9 $pA/Hz^{1/2}$. Notice also that the noise is essentially independent of frequency at zero bias, but shows a definite 1/f dependence (of noise power) upon application of reverse bias. Correlation of the magnitude of this 1/f noise to the G-R current has already been reported both for 3 to 5 μm[9] (Appendix A) and 8 to 12 μm photodiodes (Appendix B).[10] Further discussion can be found in Section 2.1.4.2.

2.1.4   Photodiode Discussion and Tradeoffs

Photodiode performance at the design temperature and wavelength is limited by two mechanisms, diffusion current and generation-recombination (G-R) current. Figure 2-7 shows a schematic diagram of the n^+ on p photodiodes as well as the expressions relating diffusion and G-R current parameters to the observed I vs V and R_0 vs T characteristics used to unambiguously separate the two. At 105 K the photodiodes are dominated by the diffusion current, as shown by the temperature dependence in Figure 2-8 and the representative I-V characteristic in Figure 2-9. The 12.6 μm photodiode is modeled at 105 K by a diffusion I_{SAT} = 40.7 μA and generation-recombination of I_{0GR} = 4.2 μA and is therefore dominated by diffusion current.

2.1.4.1   Diffusion Improvement: Larger R_0 and Smaller White Noise

The model used to quantitatively describe R_0 and the corresponding white noise was used to explore how this impedance R_0 could be raised to the goal of 500 Ω. The model now properly accounts for the diffusion current resulting from the three dimensional volume surrounding the planar photodiodes. Figure 2-10 shows the value of R_0 predicted by this model as a function of

---

9.   S.P. Tobin, S. Iwasa, and T.J. Tredwell, "1/f Noise in (Hg,Cd)Te Photo-diodes," IEEE Trans. Elec. Dev. ED-27, 43 (1980).

10.   R.J. Briggs, J.W. Marciniec, P.H. Zimmerman and A.K. Sood, "Current Mech-anisms and 1/f Noise in 8 to 12 μm n^+ on p (Hg,Cd)Te Photodiodes," Inter-national Electron Device Meeting Extended Abstract, p. 496, December 8-10, 1980.

n-TYPE

p-TYPE
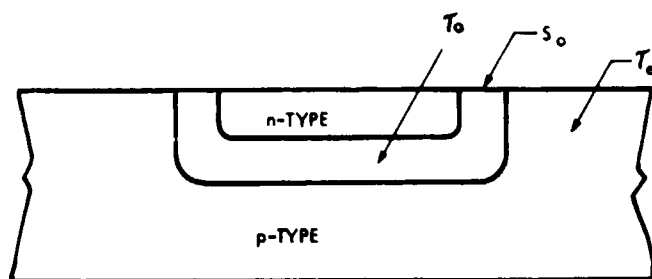
$$I = I_{SAT}(e^{qV/kT}-1) + I_{oGR}\frac{e^{qV/2kT}-e^{-qV/2kT}}{\sqrt{1-V/V_{bi}}}\, f(b)$$

$$\frac{1}{R_0} = \frac{q\,I_{SAT}}{kT} + \frac{q\,I_{oGR}}{kT}\, f(b)$$

WHERE

$$I_{SAT} = A_J\,\frac{qn_i^2}{N_A}\left(\frac{kT\mu_e}{q\,\tau_e}\right)^{1/2} = A_J\;kT\;\frac{n_i^2}{N_A}\,\frac{\mu_e}{L_e}$$

$$I_{oGR} = \frac{n_i W_o A_J}{\tau_o}\,\frac{kT}{V_{bi}}\quad\text{(BULK G-R)}\qquad OR \qquad I_{oGR} = n_i S_o W_o P_J\,\frac{kT}{V_{bi}}\quad\text{(SURFACE G-R)}$$

Figure 2-7. Schematic of n^+ or p Photodiode Limiting Mechanisms and Associated Equations

DIFFUSION MODEL

$\lambda_{co}(80K) = 13.7\,\mu m$

$\lambda_{co}(105K) = 12.6\,\mu m$

$A_J = 10^{-4}\ cm^2$

$L_e = 60\,\mu m$

$N_A = 1.4 \times 10^6\ cm^{-3}$
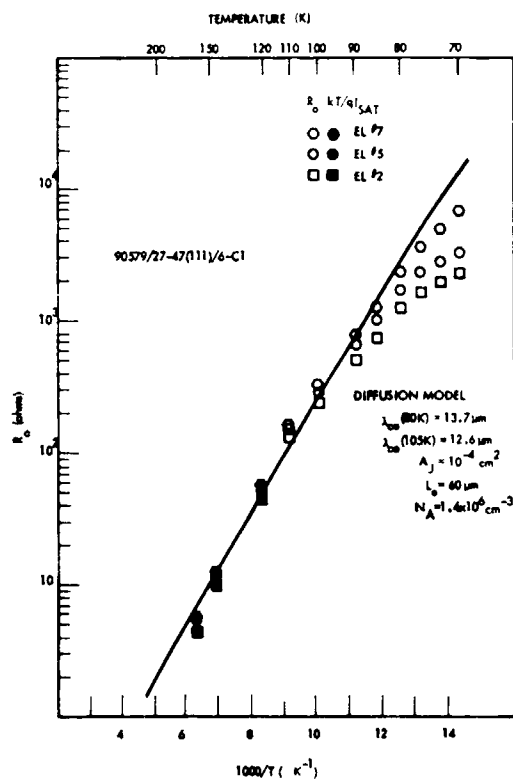
Figure 2-8. Temperature Dependence of R_0 for 10^{-4} cm^2 Photodiodes Having Cutoffs Around 12.6 µm at 105 K

2-13
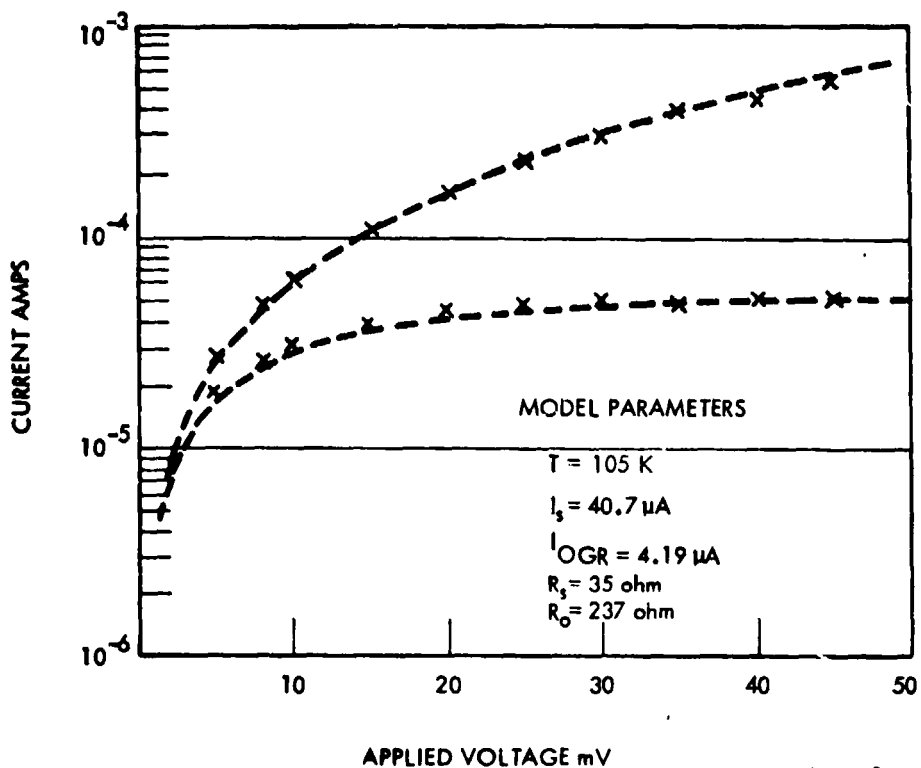
Figure 2-9. Current-Voltage Characteristic for Typical 10^{-4} cm^2 Photodiode at 105 K. Model Parameters Indicated
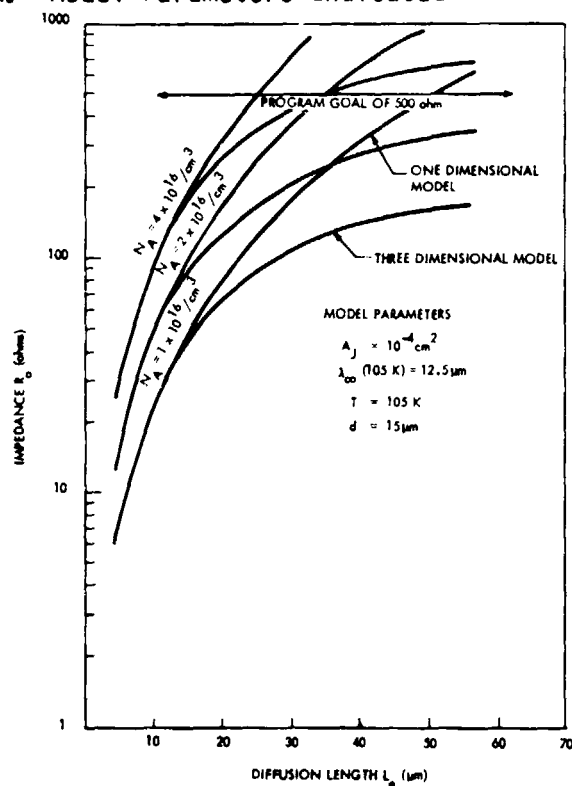
Figure 2-10. Modeled Diffusion Dependence of R_0 as a Function of Diffusion Length. Both One Dimensional and Three Dimensional Performance is Indicated for Typical Photodiode Parameters

3103-07

2-14

the minority carrier diffusion length L_e, the parameter of the material which one might hope to increase. Representative photodiode parameters are indicated. The lowest curve is for an acceptor concentration of $N_A = 1 \times 10^{16}/cm^3$, about the same used for the diodes characterized; these and in fair quantitative agreement with the measured diffusion lengths of 12 to 25 μm. The one-dimensional curve indicates how much larger R_0 would be if the diode could be converted to operate as if in a one-dimensional geometry.[11] Hence, an increase in L_e accompanied by conversion to the 1-D geometry could easily allow the program goals to be realized. Alternatively, a slight increase in acceptor concentration to $4 \times 10^{16}/cm^3$, as suggested in the figure, would allow the program goal to be reached even if the diode operation was three-dimensional.

Reduction in the photodiode junction area A_J below the masked optical area has been suggested as a method to increase the diffusion R_0 without significant loss in photocurrent.[12,13] In order to ascertain how reduction in A_J effects D*, solutions to the geometrical dependence of both photodiode photocurrent and diffusion current are required. As part of TIRA, the solutions were calculated numerically for the first time.[11] Although R_0 increases as A_J is reduced, the average photocurrent quantum efficiency η_{AVE} decreases. Figure 2-11 shows the detectivity modeled using these numerical solutions as a function of the ratoe of diode-to-mask dimensions for the case of $A_{OPT} = 10^{-4}$ cm^2 diodes. The equation describing this detectivity is:

$$D^* = \frac{(5 \text{ amp/W}) \, \eta_{AVE} \, A_{OPT}^{1/2}}{i_{EQ}} \qquad (2\text{-}15)$$

11. R.J. Briggs, "Geometrical Dependance of Small Area Photodiode Photocurrent and Diffusion Current," submitted for publication to the IRIS Specialty Group on Infrared Detectors, June 2-4, 1981.

12. A.K. Sood, J.W. Marciniec, and M.B. Reine, "8 to 12 μm Photovoltaic (Hg,Cd)Te Focal Plane Arrays," Final Technical Report, Naval Research Laboratory, Contract N00173-78-C-0145.

13. R.E. Longshore, Proc. IRIS Specialty Group on Infrared Detectors, June 12-13, 1979, p. 209.
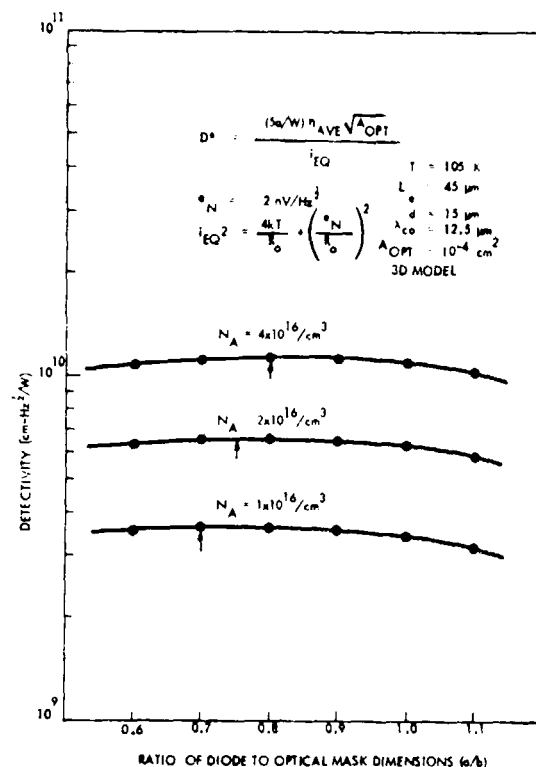
Figure 2-11. Detectivity as a Function of Diode Size for 10^{-4} cm^2 Optical Collection Area. Arrows Indicate the Maxima for Each Curve.

where

$$i_{EQ}^2 = \frac{4kT}{R_0} + \frac{e_n^2}{R_0} \qquad (2\text{-}16)$$

and the transistor buffer voltage noise is $e_N = 2nV/Hz^{1/2}$. The other diode parameters are indicated. Note both the strong N_A dependence of D^* in the figure as well as the relative insensitivity of D^* to the actual diode area chosen. No advantage in detectivity occurs by reduction of junction area. Thus, we recommend that the junction area be chosen equal to the optical area in order that the responsivity be most uniform.

Considerable increase in the diffusion limited R_0 occurs upon reduction in the cutoff wavelength. More important is the change in signal to noise (S/N). Figure 2-12 shows an estimate of the relative S/N for various choices of diode cutoff wavelength at 105 K for both a pessimistic and an optimistic value of attainable performance. As the cutoff wavelength is shortened, R_0 increases thus reducing the equivalent noise current i_{EQ}. However,

8103-07   2-16

The graph shows Signal to Noise Ratio (Arb. Units) on the y-axis (logarithmic, from 1 to 100) versus Cutoff at 105 K on the x-axis (10.5 to 13).

Annotations in figure:

R_o (12.5 µm) = 500Ω

R_o (12.5 µm) = 150Ω

T = 105 K

$$i_{EQ}^2 = \frac{4kT}{R_o} + \left(\frac{e_N}{R_o}\right)^2$$

$$e_N = 2 \; nV/Hz^{\frac{1}{2}}$$

$$S/N \; \alpha \; (\lambda_{co} - 10.4 \; \mu m)/i_{EQ}$$

CUTOFF AT 105 K
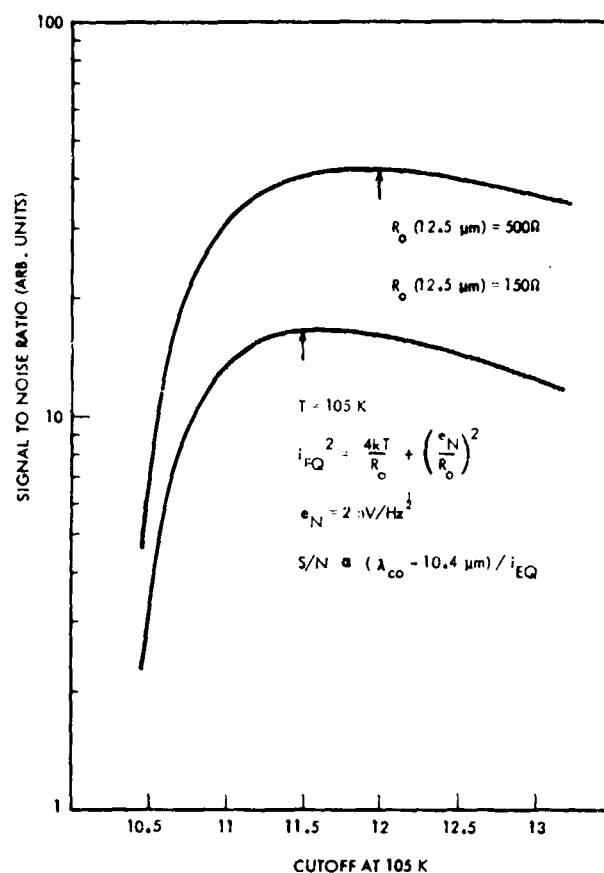
Figure 2-12.   Relative Signal-to-Noise Ratio as a Function of Cutoff Wave-
length, Assuming Uniform Thermal Illumination Longer Than 10.4 µm
Wavelength.   Arrows Indicate Approximate Maxima of Each Curve.

because the collected signal is reduced as well, the actual S/N is not a strong
function of cutoff, as indicated in the figure.   Hence reduction in cutoff
wavelength will provide no significant advantage in the S/N.

Finally, any given value of R_0 at 105 K will increase quickly if
the temperature can be lowered even slightly.   Figure 2-13 shows this strong
temperature dependence for the model parameters indicated.   Note that even a
break 5 K reduction in temperature results in 60% increase in R_0.   Hence, any
reduction in temperature is of considerable advantage to the photodiodes.

The approaches considered to increase the diffusion limited R_0 and
reach the program goal of 500 Ω are as follows:
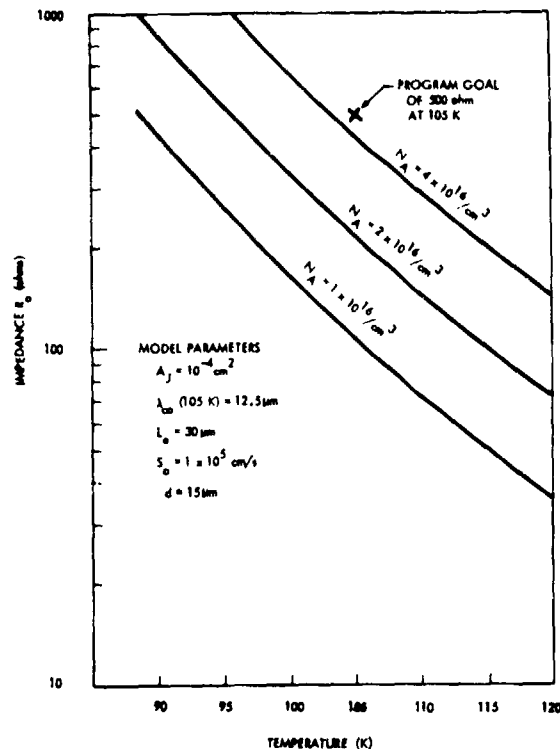
Figure 2-13. Modeled Temperature Dependence of R_0 for Typical Photodiode Parameters.

(1) Increase in L_e coupled with conversion to 1-D geometry.

(2) Slight increase in N_A to $4 \times 10^{16}/cm^3$.

(3) Choice of A_J smaller than optical area.

(4) Reduction in design cutoff wavelength.

(5) Slight reduction in operating temperature.

Our analysis indicates that R_0 = 500 Ω should be attainable by implementation of any one of considerations 1, 2, or 5 during the next phase of this program.

2.1.4.2 Generation-Recombination Improvement: Lower 1/f Noise

Proper coupling of the diodes to the CCD storage registers, even through a transistor buffer, will result in the diodes operating at some reverse bias. Figure 1-6 showed the noise current density spectrum for the same photodiode modeled in Figure 1-9. The various contributions to the observed noise current are indicated and the detector itself has a noise of only 4.9 pA/Hz$^{1/2}$. Also, the noise is essentially independent of frequency

2-18

8103-07

at zero bias but shows a definite 1/f dependence (of noise power) upon applica-
tion of reverse bias. Correlation of the magnitude of this 1/f noise to the
G-R current has been reported both for 3 to 5 μm[9] and 8 to 12 μm photo-
diodes.[10] Hence, the magnitude of the surface G-R current I_{GR} alone should
be sufficient indication as to whether low enough 1/f noise can be obtained.
This G-R current is given by:

$$I_{GR} = I_{OGR} \left[\frac{e^{qV/2kT} - e^{-qV/2kT}}{1 - V/V_{bi}^{1/2}} \right] f(b), \qquad (1\text{-}17)$$

where $I_{OGR} = n_i S_0 W_0 P_J$ (kT/V_{bi}), as suggested in Figure 2-7. Most
of the temperature and wavelength dependence is contained in the intrinsic
carrier concentration n_i. The surface quality is described by the surface
recombination velocity S_0. Here, W_0 is the depletion width at the surface,
P_J is the diode perimeter, and V_{bi} is the depletion layer built-in voltage.

The correlation of 1/f noise to I_{GR} suggests that at 40 Hz,
$I_{GR} \leq 32$ nA is required to reach a noise current of 5 pA/Hz$^{1/2}$, allowing
$D^* \geq 1 \times 10^{10}$ cm-Hz$^{1/2}$/W. Figure 2-14 shows the bias tradeoff of surface
recombination S_0 required to meet this suggested noise current density. At a
bias of 2 mV, about the tolerance to which untrimmed transistors might be
matched, values of S_0 around 3×10^4 cm/s would be required. Laser trimming
of the transistor buffer might be expected to reduce its bias variations down
to perhaps 0.2 mV, easing the surface recombination requirement by almost an
order of magnitude, as indicated in the figure. In addition, operation at
chopping frequencies larger than the 40 Hz suggested would ease the surface
recombination requirements even further, because $i_{1/f} \alpha I_{GR}/f^{1/2}$.

The values of surface recombination velocity S_0, as well as the
other parameters required to fit some of the recent Honeywell photodioes at
80 K, are shown in Table 2-1. Notice that S_0 as low as 3×10^4 cm/s is
reported.[10]

2-19

8103-07
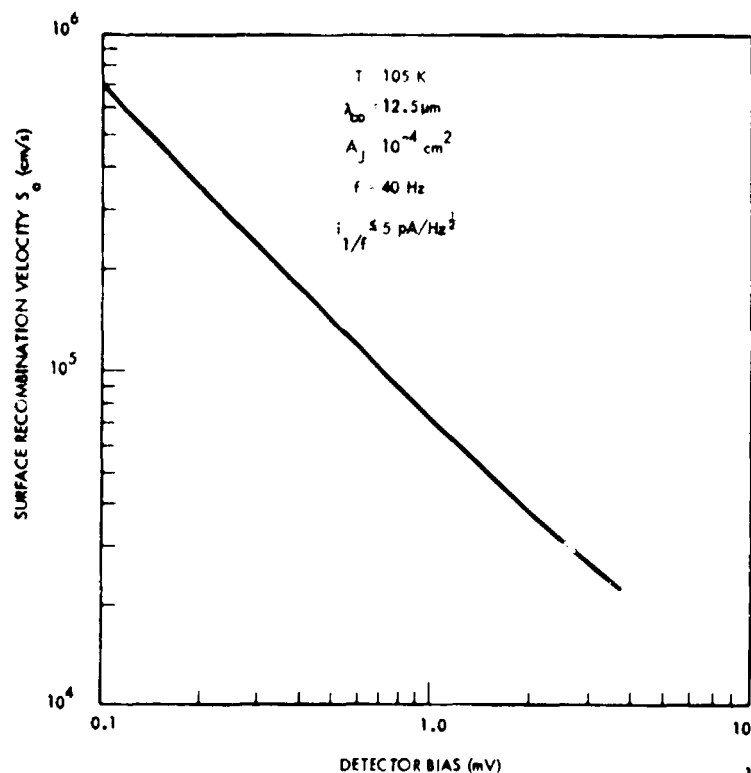
Figure 2-14. Surface Recombination Required to Meet 5 pA/Hz$^{1/2}$ Noise Current at 40 Hz, as a Function of Detector Bias.

Table 2-1. PARAMETERS DESCRIBING SURFACE IMPROVEMENT ON RECENT HONEYWELL PHOTODIODES

ARRAYS	λ_{co} (μm)	R_o	I_{SAT}	I_{OGR}	S_o	A_J
	μm	kΩ	nA	nA	cm/s	cm^2
90579/75-55(111)/5C-3B#4	9.28	170	23.5	13.2	3.5×10^5	1×10^{-4}
30779/60-60(111)/4-A2 #1	10.8	240	22	6.5	2.3×10^5	7×10^{-6}
30779/,855-110.5(111)/10-B3#22	11.0	170	38	0.84	3.0×10^4	7×10^{-6}

The discussion above indicates that the program goal 1/f noise can be achieved with some safety margin by:

(1) Use of best surface processing.

(2) Reduction of detector bias by transistor laser trimming.

8103-07

2-20

(3) Increase in system chopping frequency.

(4) Slight reduction in operating temperature.

Our analysis indicates that low enough generation-recombination current can be achieved to meet the 1/f noise specifications. Item 1 above should just be sufficient to meet the specifications. Successful implementation of any of the three other items would provide some safety margin.

2.1.4.3 Series Resistance Considerations

The proposed $R_0 A$ product of 0.05 Ω-cm^2 at 105 K for an active area of 10^{-4} cm^2 requires a diode zero bias impedance of R_0 = 500 Ω. Photodiode responsivity and thus detectivity will be degraded unless the total photodiode series resistance is small compared to R_0. Contacts to the n$^+$ side of the n$^+$ on p photodiodes having sufficiently low contact resistance can be readily made by evaporation of indium contact holes onto part of the implanted region. The spreading resistance on the n$^+$ side is not significant because of the high donor concentrations present.

The series resistance from the common p side may not be as low, however. At 105 K the resistivity of the p side for $N_A - N_D$ = 4 x 10^{16}/cm^3 is

$$\rho^{-1} = (N_A - N_D)\, q\mu_n + \frac{n_i^2}{N_A - N_D}\, q\mu_e$$

$$= (1.28 + 0.15)/(\Omega\text{-cm})$$

$$\rho = 0.70 \ \Omega\text{-cm} \tag{2-18}$$

The spreading series resistance associated with the front p side contact has been modeled as an annulus completely encircling the diode. This series resistance is relatively independent of the distance to the contact, and is given by

8103-07   2-21

$$R_S \simeq \frac{\rho}{2\pi d} \simeq \frac{0.70 \ \Omega\text{-cm}}{2\pi(15 \ \mu\text{m})} = 74 \ \Omega \qquad (2\text{-}19)$$

where p-side thickness $d = 15 \ \mu\text{m}$ has been assumed. This series resistance is low enough compared to $R_0 = 500 \ \Omega$ so that the responsivity is not significantly reduced. Hence diode series resistance should not be a problem.

2.1.5   Detector Summary and Conclusions

During phase I of this program the model quantitatively describing diffusion and G-R current photodiode limits was revised to properly account for the three dimensional diode geometry. The absorption coefficient near the bandgap was used to better determine the alloy composition and intrinsic carrier concentration.

Detailed characterizations were completed on four existing photodiode arrays having the TIRA junction area of 10^{-4} cm^2 and a range of cutoff wavelengths. Emphasis was placed on operation at 105 K. Both R_0 and I-V characteristics were fitted using our quantitative model to obtain self-consistent values of the various diode parameters. Noise spectra were taken on all diodes at zero bias and over a range of reverse biases; they were related to our quantitative model.

The measured values of R_0 for the photodiode array closest to the TIRA wavelength of 12.5 μm are about a factor of 2 lower than the 500 Ω required. Our quantitative model was used to explore various approaches to increase this diffusion limited R_0 to reach this program requirement. The analysis indicates that a value of 500 Ω for R_0 should be attainable by implementation of any one of three improvements: (1) slight increase in p side acceptor concentration, (2) increase in electron diffusion length along with geometrical modification, and (3) slight reduction in operating temperature below 105 K. All three are additive. Designing the junction area to be smaller than the optical area was considered, but was shown by numerical solution of the geometrical dependence to provide no significant advantage for

2-22

system detectivity. Slight reduction in the design cutoff wavelength was also considered. It was shown to increase the system detectivity due to an increase in R_0 but to provide no significant advantage in the system signal-to-noise ratio because of reduction in the collected photons.

The measured value of 1/f noise for the photodiode array closest to the TIRA wavelength of 12.5 μm are close to the program requirements. The reported correlation of this 1/f noise[9,10] to the surface G-R current I_{GR} was used to suggest an upper bound to I_{GR}, expressed quantitatively by the surface recombination velocity S_0 and temperature dependent intrinsic carrier concentration. Recently reported Honeywell values of S_0 were given.[10] Our analysis indicates that low enough G-R current may just be achieved to meet the 1/f nosise specifications using our best surface processing techniques. Additional safety margin will result from implementation of any one of three improvements: (1) reduction in detector bias by laser trimming the buffer transistors, (2) slight increase in system chopping frequency, and (3) slight reduction in operating temperature below 105 K.

2.2   BIPOLAR BUFFERS

The applicability of bipolar buffers for TIRA has been given conside able attention throughout this phase. The major difficulty was in determining the performance of the buffer at the 105 K operating temperature. A literature search shed little light on the subject and the few sources that were available disregarded 1/f noise sources altogether. Hence the problem was taken into the laboratory where measurements of standard off-the-shelf bipolar transistors were made at various tempertures down to 77 K. The analysis of the measurements was used to generate the requirements for the bipolar buffer given in the following section. A discussion of the actual measurements is contained in Section 2.2.2.

2.2.1   Bipolar Buffer Requirements

A linear array of bipolar transistor buffers is required to interface between the low impedance (Hg,Cd)Te detectors and a CCD readout multiplexer.

The first design requires 64 channels on a 256 mil chip allcwing about 4 mils per channel. The second design, with two rows of detectors per module, requires twice as many channels in the same space.

The bipolar buffer circuit schematic for a single channel is shown in Figure 1-3 of Section 1-1. The buffer consists of a common base NPN amplifier with a laser trimmable emitter resistor to adjust the bias voltage on the detector to zero. The characteristics of the buffer are listed in Table 2-2 for operation at 105 K.

A preliminary layout for the buffer is shown in Figure 2-15. Four octagonal emitters are used to minimize the base resistance and lower the noise figure of the buffer. Furthermore, the common base p region is connected to the isolation p+ diffusions surrounding the emitters with contact cuts made along the isolation diffusion. With this configuration it is possible to consider the substrate to be the base contact; otherwise the substrate will have to be insulated during packaging. The emitter resistors are made from chrome-silicon. The large pad areas are used to probe test the buffer and to lay totally evaporated leads (TEL's) as interconnects with the detector and CCD.

Table 2-2. BIPOLAR BUFFER CHARACTERISTICS AT 105 K

R_C	300 kΩ to 500 kΩ (750 kΩ to 1.3 MΩ at 300 K)
R_E	3.5 kΩ laser trimmable to 10 kΩ
Configuration	Common base NPN Multiple Emitters
Base Resistance	200 Ω at (300 K)
β	20 $\sim$ ($\sim$ 200 at 300 K)

2-24

8103-07

CROSS-SECTION

COLLECTOR

EMMITER

OXIDE

p

20 mils

TOP VIEW

8103-07

2-25
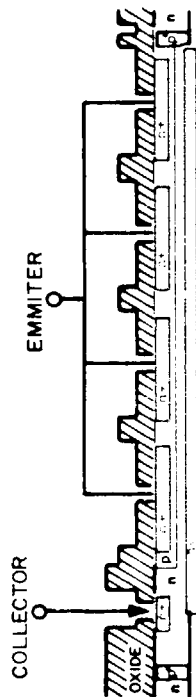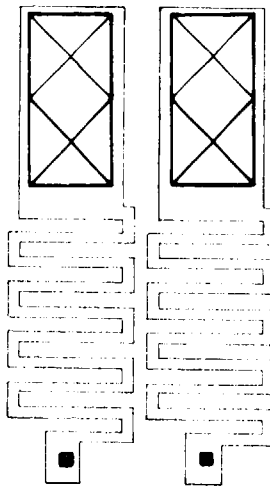
Figure 2-15. TIRA Bipolar Buffer Circuit Layout

The active area for the first design (consisting of 64 channels) can be realized with a width of 50 mils in the direction of information flow. The second, 128 channel array may be twice as wide. However the overall chip width will be about 300 mils to accommodate both the (Hd,Cd)Te plank and CCD multiplexer mounted on top.

2.2.2   Laboratory Measurement of Bipolar Transistors

Samples of several types of integrated circuit transistors have been measured for noise performance at 77, 100, 120, and 300 K. These transistors were fabricated by the Honeywell Solid State Electronics Division using a standard process for manufacturing linear integrated circuits. The results show that these transistors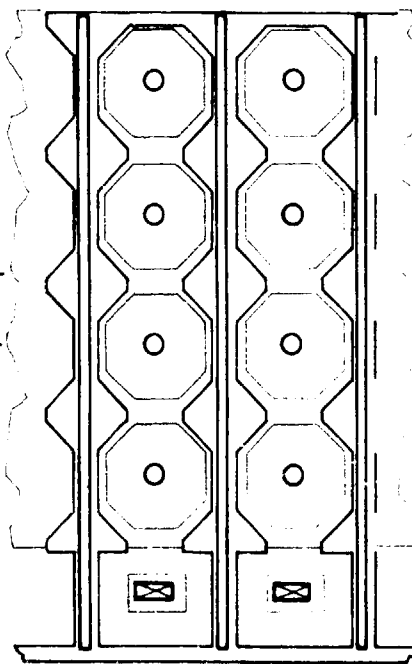 are good enough for coupling 500 Ω detectors to a CCD. With a minimal change in geometry to lower the base resistance, lower impedance detectors can be accomodated.

2.2.2.1   Description of Experimental Set-up

Figure 2-16 is a block diagram of the noise measuring setup. The device under test (DUT) is mounted in a variable temperature dewar or immersed in liquid nitrogen. The voltage amplifier operates the DUT at a constant current of 1 mA, 100 μA, or 10 μA. The output of the voltage amplifier is the noise voltage of the DUT with a gain of 200. The current amplifier measures base current and the associated noise. This scheme allows noise measurements to be performed quite rapidly and without the necessity of measuring gains to refer the noise to the input.

2.2.2.2   Types of Devices Tested

All the devices were fabricated by the Honeywell Solid State Electronics Division. We tested lateral and vertical PNP transistors, and vertical NPN devices with different geometries. The best devices at 100 K were the vertical PNP's with sufficient performance to meet TIRA requirements. However, these devices inherently have the collector connected to the substrate and are therefore unsuitable for use as common base amplifiers.
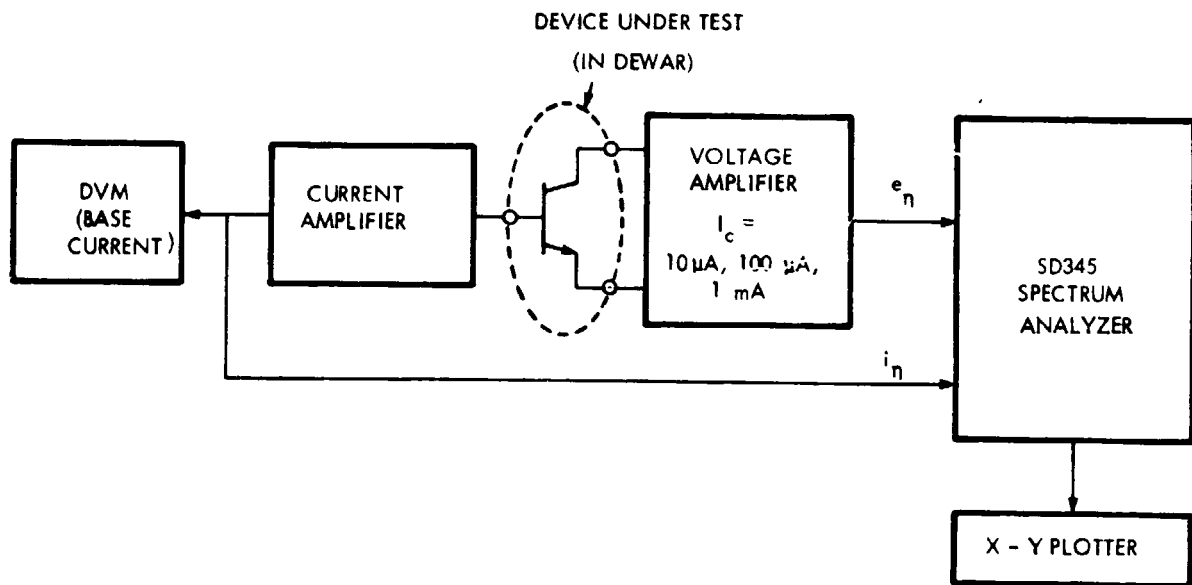
Figure 2-16. Transistor Noise Measurement Setup

The next best devices were the NPN's with 2 mil (50 μm) diameter emitters. Figure 2-17 shows the layout of these transistors. Briefly described, the fabrication process is as follows: diffuse in buried layer on p-type substrate (reduces collector resistance in NPN's, increases β in lateral PNP's); grow epitaxial n layer (forms NPN collectors, resistors); form p^+ isolation diffusions; base diffusion (NPN bases, PNP emitters and collectors, resistors); emitter diffusion. The entire chip is then passivated for surface protection. This process is typical for linear integrated circuits; many manufacturers make similar devices.

2.2.2.3 Measurement Results

Figures 2-18 through 2-21 show results of measurements on one of the 2 mil NPN's at 300 K, 120 K, 100 K and 77 K. THe solid curves are input referred noise voltage e_n in $nV/Hz^{1/2}$; the dashed curves are base current noise in $pA/Hz^{1/2}$.

8103-07   2-27
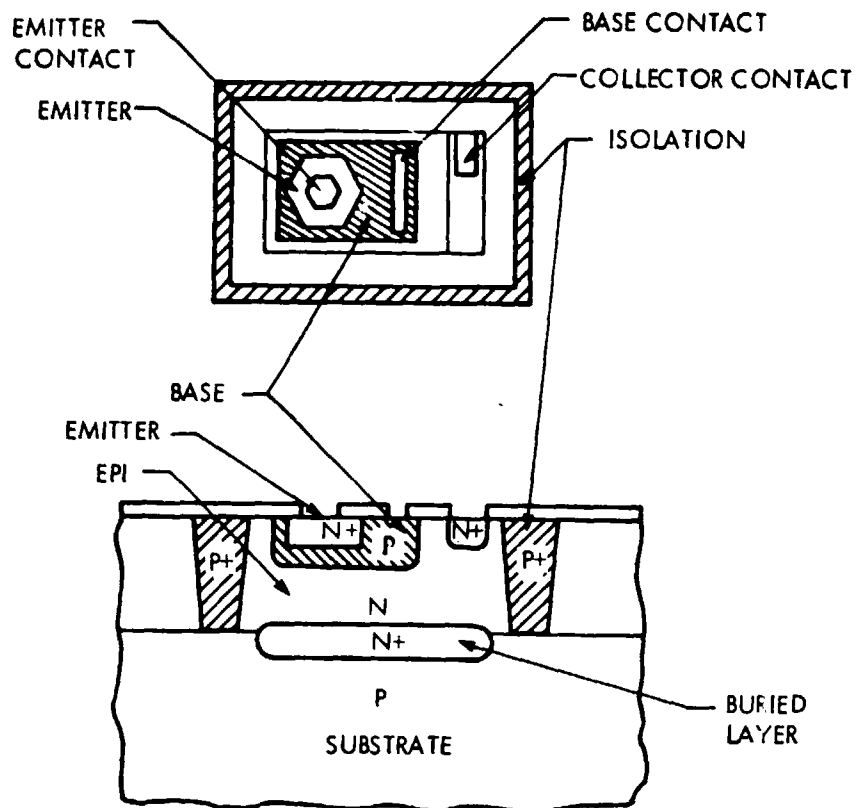
Figure 2-17. NPN Transistor Geometry
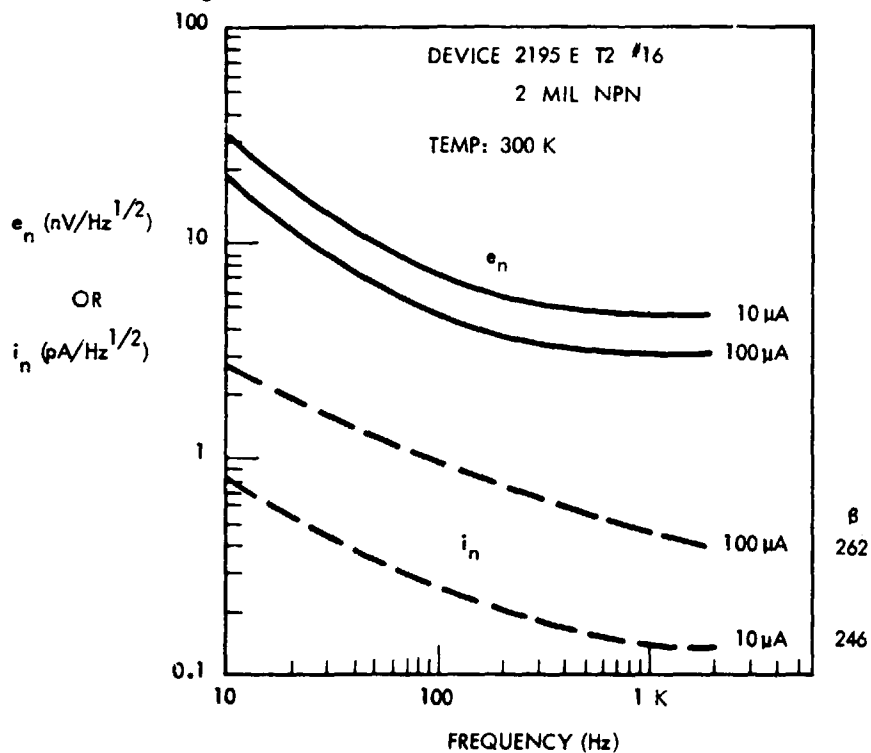
Figure 2-18. Noise Performance of NPN Transistor at 300 K
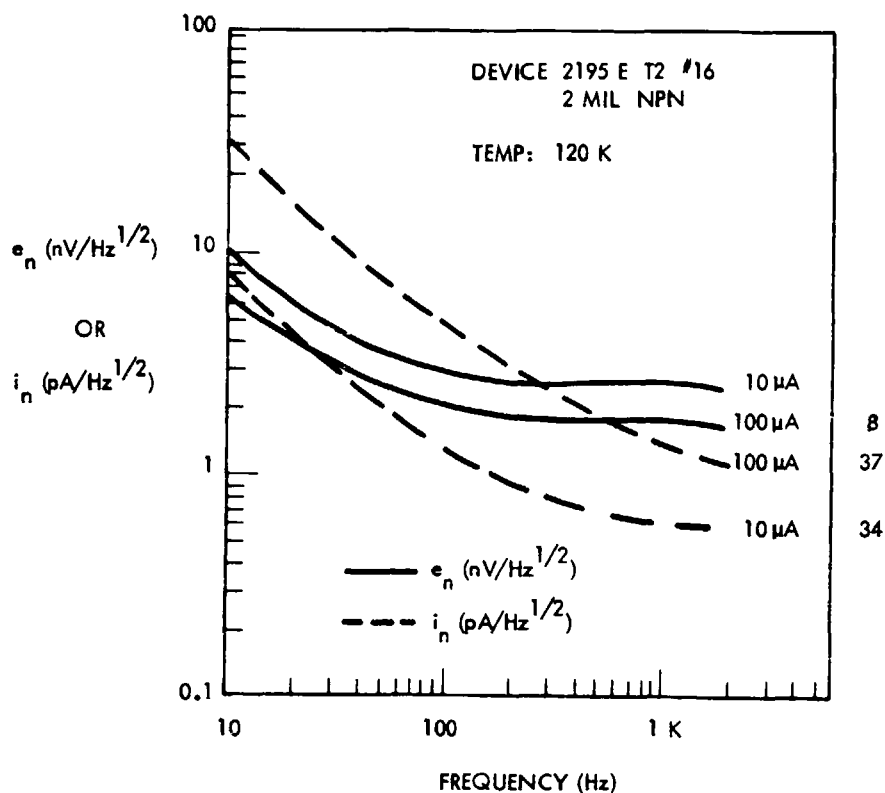
Figure 2-19.   Noise Performance of NPN Transistor at 120 K
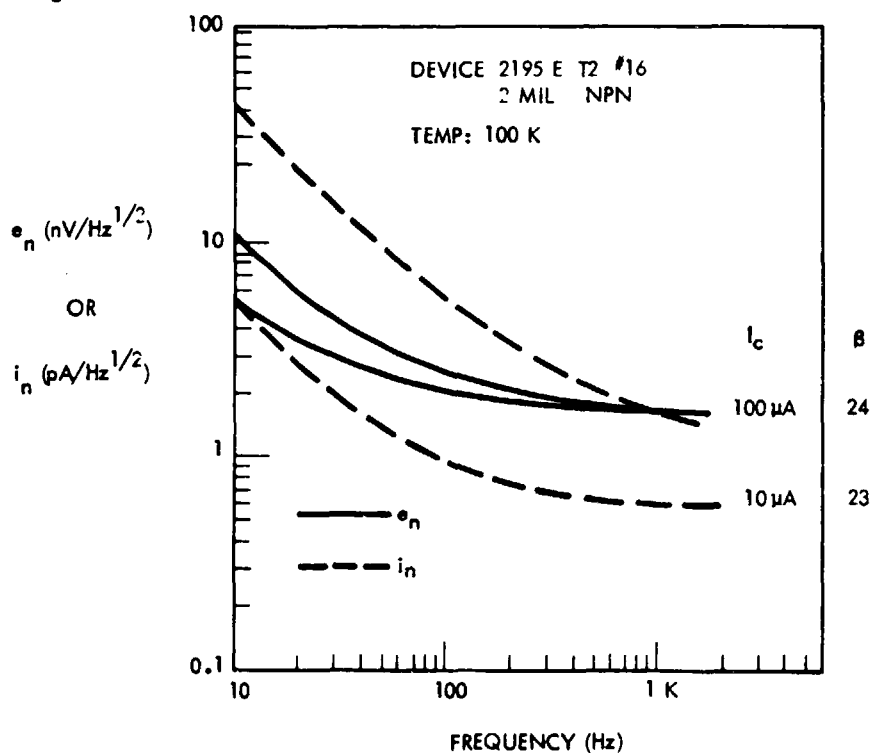
Figure 2-20.   Noise Performance of NPN Transistor at 100 K
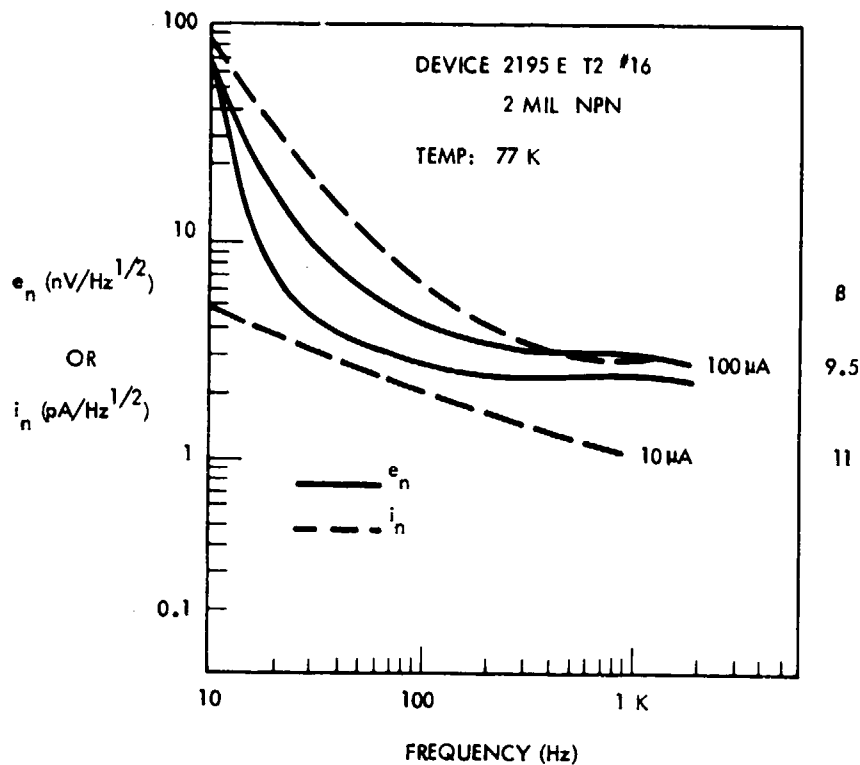
Figure 2-21. Noise Performance of NPN Transistor at 77 K

Figure 2-22 shows noise voltage and noise current vs temperature at 50 Hz and 500 Hz for another 2 mil NPN. The general trend is for noise voltage to decrease with decreasing temperature, while the noise current increases. These observations are precisely what is expected. Recall the voltage noise and current noise equations for the bipolar transistor given in Section 1.2.1. The noise voltage term decreases because the base resistance decreases with lower temperature and because of the lower dynamic emitter resistance. Also since the transistor beta decreases with lower temperature, more base current is required, generating higher current noise. At a low enough temperature the simple model is not valid, as demonstrated by a rapid increase in both the voltage and current noise. The optimal operating point for TIRA is just above 100 K before the voltage and current noise begin to increase rapidly.

2.2.2.4   Discussion of Results

The total buffer noise i_T is given by

$$i_T^2 = i_n^2 + e_n^2/R_o^2$$

8103-07   2-30
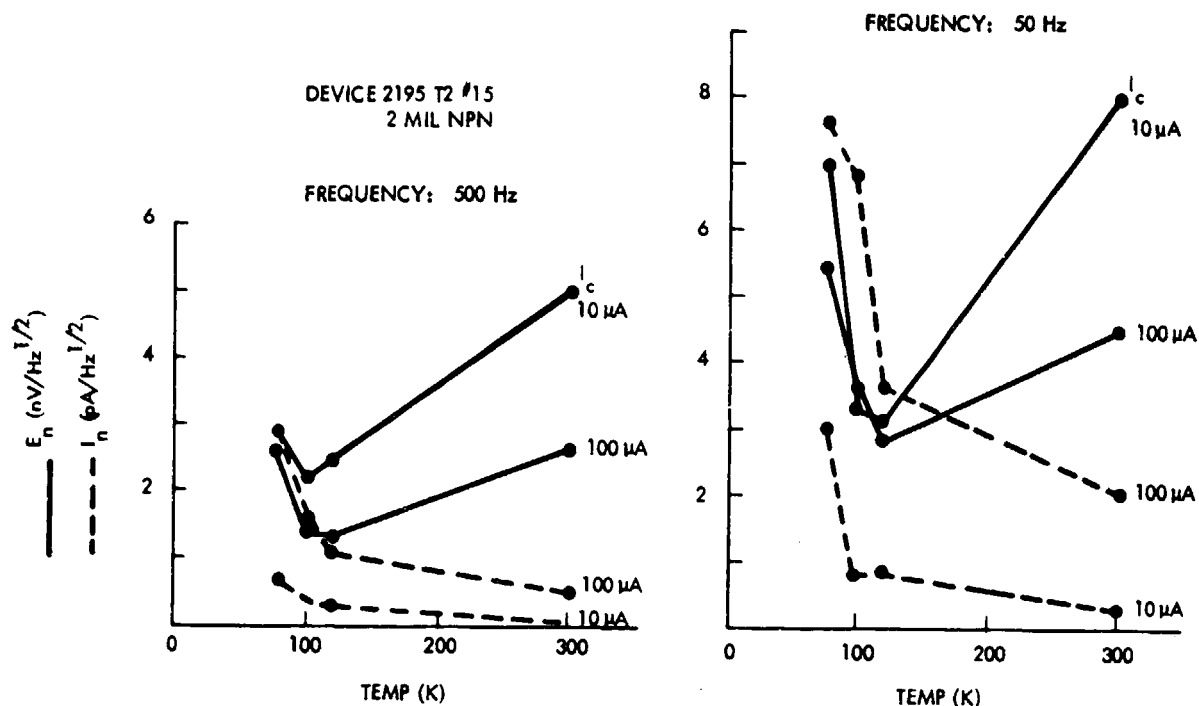
Figure 2-22. Transistor e_n, i_n Versus Temperature

where R_0 is the detector dynamic resistance. For acceptable performance from 500 Ω detectors, the requirements are:

$$e_n < 2.5 \text{ nV/Hz}^{1/2}; \quad i_n < 5 \text{ pA/Hz}^{1/2}.$$

These devices easily meet these requirements at 500 Hz and almost meet them at 50 Hz. For 150 Ω detectors, the requirements are:

$$e_n < 0.75 \text{ nV/Hz}^{1/2}; \quad i_n < 5 \text{ pA/Hz}^{1/2}$$

The 2 mil NPN's do not meet this requirement. One of the two vertical PNP's did. The reason for this result is almost certainly that the NPN's have a higher base resistance, which generates thermal noise and also generates noise due to the noisy base current flowing through it. An NPN made by the same process but with a different geometry for lower base resistance would give a better e_n, thus allowing lower resistance detectors.

8103-07   2-31

Near the end of the contract, some multiple emitter NPN devices fabricated with the Honeywell standard linear bipolar process became available for testing. Since these devices were complete circuits rather than test chips, extraordinary steps were taken to isolate single devices for testing. These transistors did show, as expected, much lower base resistance ($< 50 \, \Omega$ at 300 K) than the single emitter devices. The noise voltage at low temperatures was as low as 0.7 mV/Hz$^{1/2}$ at 100 µA collector current. These devices demonstrated that the basic multiple emitter design is capable of the required performance level. Unfortunately, this particular batch of devices showed higher base noise current than the earlier batch on both single and multiple emitter devices, which might be due to processing variations or the unusual packaging methods.

2.3   CCD REQUIREMENTS

The CCD Array is designed to multiplex the 64 channels (128 for optional design 2) to readout in a serial manner. The CCD chip will be mounted on top of the bipolar buffer substrate as shown in Figure 1-1, and electrically connected to the buffers using TELs. Because the CCD will be mounted on top of the bipolar substrate, additional contacts must be supplied on the surfaces of the CCD to the substrate. The CCD input structure will be an AC gate coupled circuit as shown in Figure 1-3 . The on-chip coupling capacitor C_C must be at least three to five times the capacitance of the input gate and shielded from the substrate to guarantee good coupling efficiency. A preliminary layout scheme for the input circuit is shown in Figure 2-23. For the 64 channel design the CCD input channel will be designed on less than 4 mil centers, to accommodate metal interconnect lines directed around the active chip array. The charge capacity of the CCD will be 1.0×10^8 electrons. The 128 channel design option must fit within 2 mil centers and have the same charge capacity. Figure 2-24 illustrates a possible design for the 128 channel CCD. In both designs the control gate area should be as large as possible (80 µm)^2 to minimize 1/f noise and should be fabricated so as to minimize leakage current across the source diffusion to substrate.

A two phase buried channel shift register will be used to multiplex the input channel. Both the fat zero and output structure must be configured to fit within the length of the chip. Maximum clock rate is 100 kHz.

8103-07   2-32
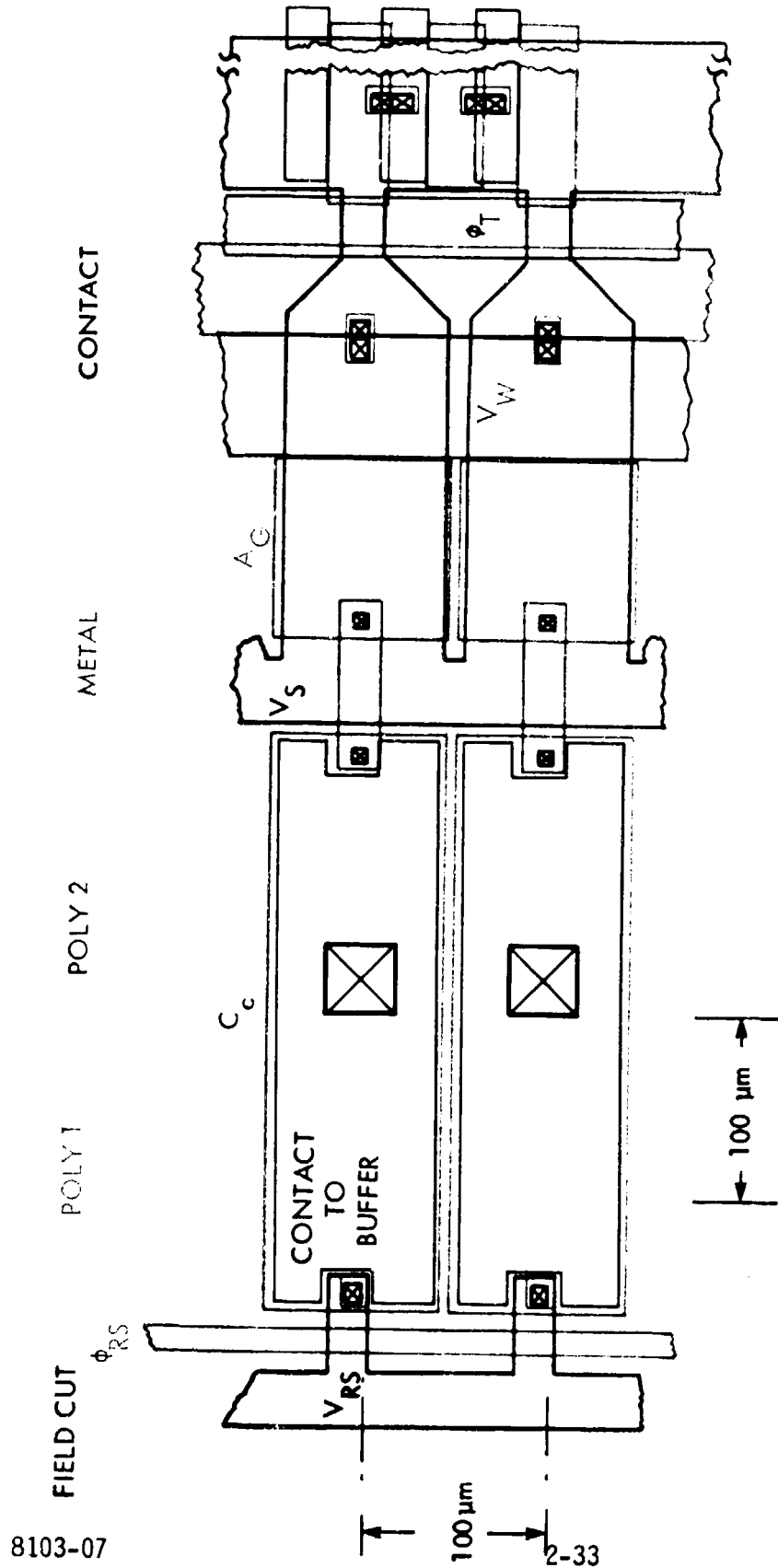
Figure 2-23. TIRA CCD Layout for Hybrid Design

8103-07

2-33

FIELD CUT   POLY 2   METAL CONTACT
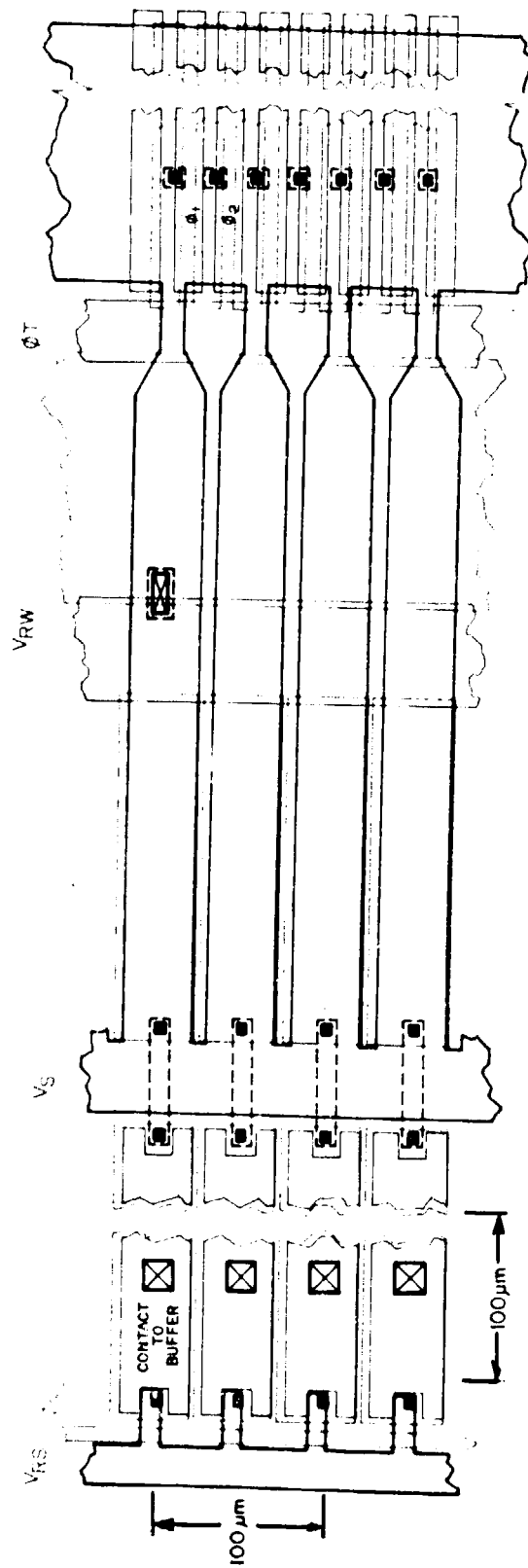
Figure 2-24. TIRA CCD Layout for Optional Design With 128 Channel per Model

SECTION 3
SYSTEMS CONSIDERATIONS

3.1 SYSTEM REQUIREMENTS

TIRA is designed for two classes of missions: an advanced LANDSAT
Low Earth Orbit (LEO) Satellite and a Synchronous Earth Observing Satellite
(SEOS). Orbital characteristics for LEO are assumed to be similar to current
LANDSAT orbits, as indicated in Figure 3-1. Pushbroom scanning along the
orbital track results from the satellite velocity, traversing the ground at
6.77 km/s. The SEOS orbit as shown in Figure 3-2 is geostationary; since there
is little relative velocity between satellite and ground, the satellite or
instrument must be slewed (at about 0.002°/s) to effect a scan.

The sensor system requirements used in the TIRA study are listed in
Table 3-1. Starred (*) parameter values were specified by GSFC; the others
were derived or resulted from the system design study. For either mission, the
focal plane array consists of one thousand 100 x 100 μm elements. Each element
for LEO has to resolve 120 m, requiring an instantaneous field-of-view (IFOV)
of

$$\frac{120 \text{ m}}{705 \text{ km}} = 0.17 \text{ mr}; \tag{3-1}$$

the IFOV is 0.023 mr for the SEOS 800 m resolution. As a result, the optical
focal length for the LEO and SEOS systems are, respectively,

$$f = \frac{a}{IFOV} = 59 \text{ cm and } 448 \text{ cm} \tag{3-2}$$

where a is the detector element width.

- CIRCULAR ORBIT
- SUN SYNCHRONOUS
    - /DESCENDING NODE AT 9:30 AM
- 705 km ALTITUDE
- 98.2° INCLINATION
- 98.6 MINUTE PERIOD
- 6.77 km/s PROJECTED GROUND VELOCITY
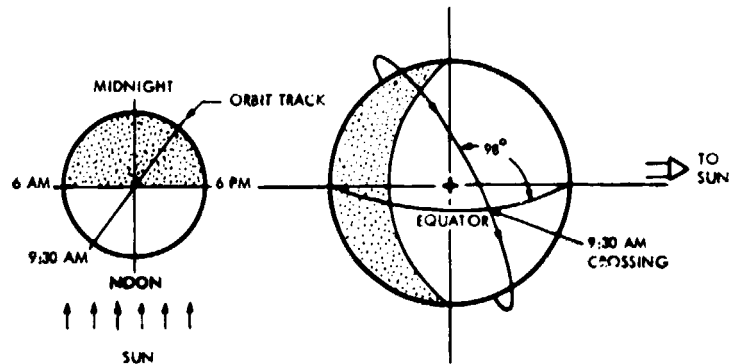
Figure 3-1. LEO Orbital Parameters

- GEOSTATIONARY

    (EQUATORIAL ORBIT WITH ORBITAL PERIOD
    ≈ 24 HOURS, i.e., FOLLOWS THE ROTATION
    OF EARTH)

- 35,900 km ALTITUDE

- SCAN MOTION CREATED BY SPACECRAFT SLEW

    - MAXIMUM RATE ≈ 0.6 s/RESOLUTION ELEMENT
      (0.002°/s)

CONSTANT
NO-SUN
DIRECTIONS

SUN
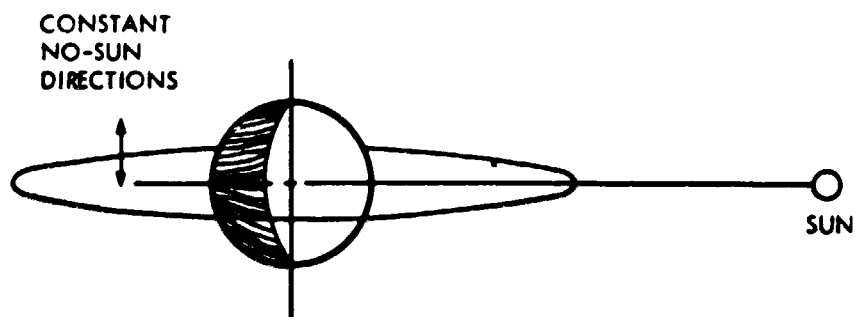
Figure 3-2. SEOS Orbital Parameters

3-2

8103-07

Table 3-1. TIRA SENSOR REQUIREMENTS

GIVEN/DERIVED	LEO	SEOS
Sensor Altitude	*705 km	35,900
Ground Resolution	*120 m	*800 m
Detector IFOV	0.17 mr	0.023 mr
	2.89×10^{-8} ster	4.97×90^{-10} ster
Number of Detectors	*1000	*1000
Swath Width	*120 km	*800 km
Sensor FOV	9.74°	1.32°/s
Projected Ground Velocity	6.77 km/s	--
Maximum Scan Rate	--	0.002°/s
Sensor Dwell Time	17.8 ms	*600 ms
Samples/Dwell Time	2	2
Integration Time	8.9 ms	300 ms
Time-Bandwidth Product	1	1
Noise Bandwidth	106 Hz	2.2 Hz
Spectral Bandwidth	*10.5 to 12.5 μm	*10.5 to 12.5 μm
Detector Dimension	*100 x 100 μm	*100 x 100 μm
Array Temperature	105 K	105 K
Sensor Efficiency	0.2	0.2
Focal Length	58.8 cm	448.4 cm
F-number (Baseline)	3	3
Aperture Diameter (Baseline)	20 cm	1.49 m
Aperture Area (Baseline)	324 cm^2	1.75 m^2
Required NER (W/cm^2-sr)	9.2×10^{-6}	9.2×10^{-6}
N_{TDI}	2	2
D* Required (cm-Hz$^{1/2}$/W) With Baseline Optics	8.06×10^9	1.39×10^9

The dwell time, the time to traverse one resolution element, is fixed for SEOS at 600 ms and derived for LEO from the projected ground velocity of 6.77 km/s to be 17.8 ms. In order to prevent blurring, the signal must be sampled twice per resolution element; thus the integration times are half the dwell times.

3-3

8103-07

Mission sensitivity requirements are expressed in terms of the Noise Equivalent Radiance (NER), defined as the scene radiance required to yield an S/N of one at the sensor output. The GSFC requirement of a minimum S/N of 5, for an inband input of 0.046 mW/cm^2-sr, requires an NER of:

$$\frac{(4.6 \times 10^{-5} \text{ W/cm}^2\text{-sr})}{5} = 9.2 \times 10^{-6} \text{ W/cm}^2\text{-sr} \qquad (3\text{-}3)$$

The array D* requirements can be derived from the NER as a function of sensor optical and electrical parameters:

$$D^* \text{ (Required)} = \frac{(A_D \, \Delta f / N_{TDI})^{1/2}}{\eta \, \Omega \, A_0 \, \text{NER}} \qquad (3\text{-}4)$$

where A_D = detector area (cm^2)

Ω = detector IFOV (STER)

f = focal length (cm)

Δf = noise bandwidth (Hz)

N_{TDI} = number of time delay and integration elements

η = $\eta_0 \eta_B \eta_E$ = system efficiency

η_0 = optics transmittance

η_B = efficiency of detector-blur spot correlation

η_E = electronics efficiency

A_0 = effective optical aperture area (cm^2)

NER = noise equivalent radiance (W/cm^2-sr)

The noise bandwidth is:

$$\Delta f = 1/t_I \qquad (3\text{-}5)$$

where t_I is the integration time.

At this level of detail, a sensor efficiency of η = 0.2 is a good estimate. Two TDI elements have been selected for TIRA, not so much for added sensitivity, as for tolerance to channel outages. The optics recommended (see

3-4

8103-07

Section 3.2) have F-numbers of 2.89 for LEO and 3.0 for SEOS. The aperture diameters and areas for LEO and SEOS are 20 cm/324 cm^2 and 1.49 m/1.75 m^2. Calculating the D* requirements from the parameters above results in 8.06 x 10^9 and 1.39 x 10^9 cm-Hz$^{1/2}$/W for LEO and SEOS, respectively.

The modulation transfer function (MTF) requirements are discussed in Section 3.3. Chopper issues are covered in Section 3.4. The TIRA array will be cooled to 105 K; temperature tradeoffs and cooling methods are discussed in Section 3.5.

3.2   TIRA OPTICS

Optical designs suitable for the LEO and SEOS missions have been generated. The parameter values of Table 3-1 for detector size, IFOV, and total FOV were used together with the following additional constraints on the design: the sensors should have a flat focal surface, the optics should contain no refractive elements, and an intermediate focal plane should be provided for a chopper. These goals were met for the SEOS design. The LEO design has a refractive aspheric plate; however, it has minimal dispersive effect because it has no optical power.

The system F-number (and therefore the aperture diameter) was chosen to be as low as possible, consistent with the flat field requirement and acceptable image quality. Because of the extremely different optical requirements, separate designs were needed for each mission. The designs are described in the following sections.

3.2.1   LEO Design

The LEO optical system parameters are shown in Table 3-2. The wide FOV and small IFOV suggest using a Schmidt telescope. In order to have an intermediate image and no field curvature, confocal parabolas were combined with a Schmidt-Cassegrain telescope. Two views are shown in Figures 3-3 and 3-4. The Schmidt-Cassegrain departs from the classical configuration in which both mirrors are concentric about the aperture stop (aspheric plate) in order to make the system more compact and the image more accessible. The

3-5

8103-07
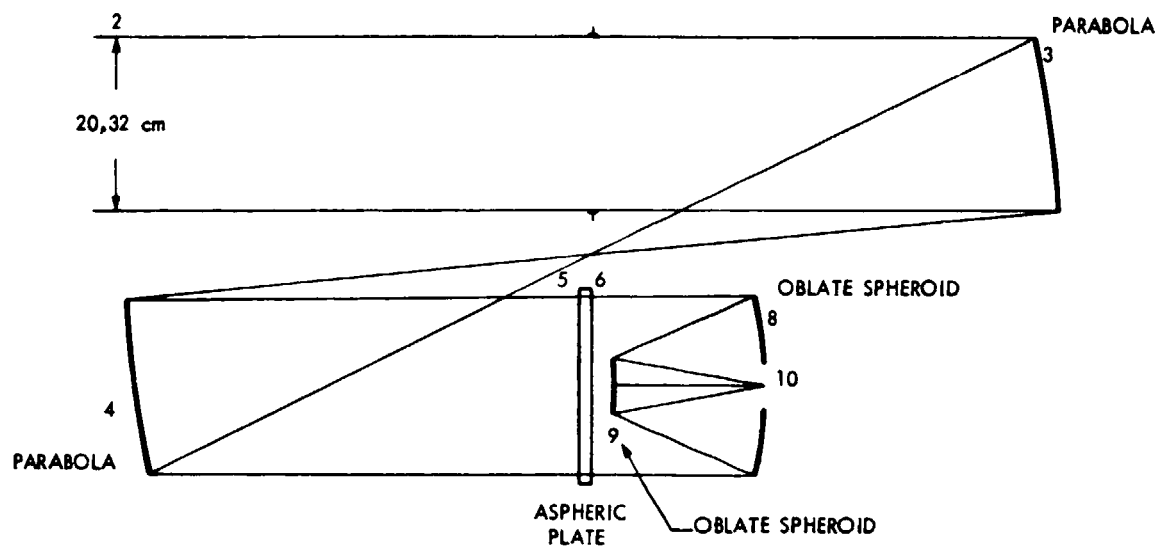
Figure 3-3. LEO Design, Y-Z View
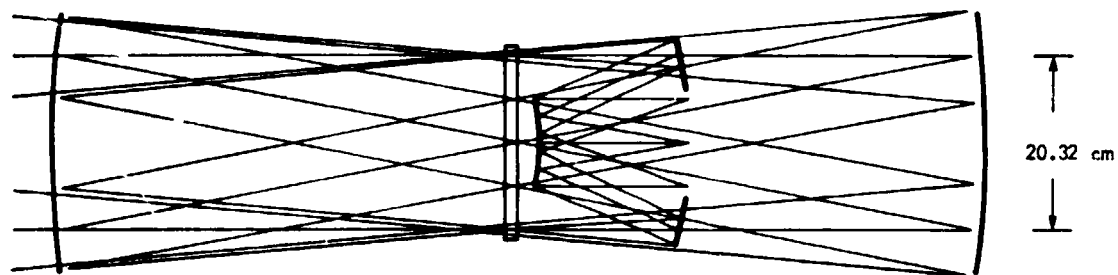
Figure 3-4. LEO Design, X-Z View

Table 3-2. LEO OPTICAL SYSTEM PARAMETERS

Focal Length	58.8 cm
Entrance Pupil Diameter	20.32 cm
F-Number	2.89
FOV	±4.87°
Detector IFOV	0.17 mr
Wavelength Range	10.5 to 12.5 μm

Schmidt-Cassegrain telescope will not cover the FOV unless it is used on axis as shown.

Table 3-3 gives the LEO design optical prescription in the standard ACCOS V format. Surface numbers are indicated in Figure 3-3. Table 3-4 gives the geometrial blur size as a function of field angle. The blur is smaller than the detector IFOV over the entire array FOV.

3.2.2 SEOS Design

The SEOS telescope has a collecting aperture approximately five feet in diameter, and a 1.32° FOV. The optical parameters are shown in Table 3-5. Because of the large aperture and relatively small FOV, a Cassegrain type telescope with relay mirrors was selected. Two views are shown in Figures 3-5 and 3-6. The system F-number and relay magnification were chosen to give a flat field without an extremely long telescope. Table 3-6 gives the SEOS design optical prescription. Table 3-7 gives the geometrical blur size as a function of field angle. The telescope is diffraction limited over the entire array FOV.

The Itek report "Requirements and Concept Design for Large Earth Survey Telescope for SEOS," written April 1975 for GSFC, was examined in order to determine its applicability to the present requirements. The design was not used because it has refractive elements and a curved image surface. It also has an intermediate focal plane that is much larger than the final image, which would require an unacceptably large chopper.

Table 3-3. OPTICAL PRESCRIPTION FOR THE LEO [.SIGN

```
LENS UNITS ARE INCHES

 REF OBJ HT                 REF AP HT   OBJ SURF  REF SURF  IMG SURF
-0.874887E 09 (  5.00 DG)    4.00000       0         6         10
```

EFL	BF	F/NBR	LENGTH	GIH
-23.1490	6.9569	-2.89	46.0000	-2.0275

WAVL NBR	1	2	3	4	5
WAVELENGTH	11.50000	10.50000	12.50000	0.	0.
SPECTRAL WT	1.0000	0.5000	0.5000	0.	0.

BASIC LENS DATA

SURF	CV	RD	TH	MEDIUM	RN	DF
0	0.	0.	0.100000E 11	AIR		
1	0.	0.	0.	AIR		
2	0.	0.	46.000000	AIR		
3	-0.022804	-43.852000	-43.852000	RFFI		
4	0.022804	43.852000	21.326000	RFFI		
5	0.	0.	0.600000	MATI GERM	4.002271	0.904
6	0.	0.	1.055000	AIR		
7	0.	0.	6.945000	AIR		
8	-0.050398	-19.842000	-6.945000	RFFI		
9	-0.096006	-10.416000	6.956927	RFFI		
10	0.	0.	0.	AIR		

REFRACTIVE INDICES

SURF	N1	N2	N3	N4	N5	ABBF
5	4.002271	4.002748	4.001945	1.000000	1.000000	3734.747283

CC AND ASPHERIC DATA

SURF	CC	AD	AE	AF	AG
3	-1.00000E 00				
4	-1.00000E 00				
6	0.	2.11239E-05	-1.77699F-07	1.58958E-08	-3.02054E-10
8	1.29076E 00				
9	2.47430E 00				

TILT AND DEC DATA

SURF	TYPE	YD	XD	ALPHA	BETA	GAMMA
1	DEC	0.	0.00000			
2	DEC	0.	-0.00000			
3	DEC	-6.00000	0.			
5	DEC	-6.00000	0.			

CLEAR APERTURES AND OBSTRUCTIONS

SURF	TYPE	CAY	CAX
6	CIRCLE	4.0000	
7 (OB)	ELLIPSE	1.2000	2.0000
8 (OB)	RECTANGLE	1.0000	2.5000

APERTURE STOP AT SURF 6

EVALUATION MODE IS FOCAL

CONTROL WAVELENGTH IS 1

PRIMARY CHROMATIC WAVELENGTHS ARE 2 - 3

SECONDARY CHROMATIC WAVELENGTHS ARE 2 - 1

8103-07

Figure 3-5. SEOS Design, Y-Z View.

Figure 3-6. SEOS Design, X-Y View.

3-9

Table 3-4. LEO OPTICAL DESIGN BLUR CHARACTERISTICS

Field Angle (°)	90% Geometrical Blur Size	
	Tangential (mr)	Sagittal (mr)
0.0	0.042	0.042
2.5	0.057	0.063
3.5	0.079	0.084
4.0	0.142	0.133

Table 3-5. SEOS OPTICAL SYSTEM PARAMETERS

Focal Length	448.40 cm
Entrance Pupil Diameter	149.35 cm
F-Number	3.00
FOV	± 0.66°
Detector IFOV	0.023 mr
Wavelength Range	10.5 to 12.5 μm

3.3   MODULATION TRANSFER FUNCTION (MTF)

The TIRA system MTF called for in the specification is the product of the detector MTF, optics MTF, and the CCD MTF. The MTF of the system employing the optics presented in Section 3.2 can meet the requirements at the high frequency $(2 \cdot FOV)^{-1}$, is marginal at the middle frequency $(3 \cdot IFOV)^{-1}$ and fails to satisfy the requirement at the low frequency $(4 \cdot IFOV)^{-1}$ (Table 3-8).

To meet the MTF specifications, the optics system must be made to resemble that of the thematic mapper from which the specification was derived. Unfortunately, such an optical design would also require a curved focal plane and would almost certainly use refracting elements. We have presented alternative optical designs as a means to understand the tradeoffs which will be available for the utilization of the TIRA focal plane.

3-10

Table 3-6. OPTICAL PRESCRIPTION FOR THE SEOS DESIGN

LENS UNITS ARE INCHES

REF OBJ HT		REF AP HT	OBJ SURF	REF SURF	IMG SURF
-0.874887E 09 (	5.00 DG)	4.00000	0	6	10

EFL	BF	F/NBR	LENGTH	GIH
-23.1490	6.9569	-2.89	46.0000	-2.0275

WAVL NBR	1	2	3	4	5
WAVELENGTH	11.50000	10.50000	12.50000	0.	0.
SPECTRAL WT	1.0000	0.5000	0.5000	0.	0.

BASIC LENS DATA

SURF	CV	RD	TH	MEDIUM	RN	DF
0	0.	0.	0.100000E 11	AIR		
1	0.	0.	0.	AIR		
2	0.	0.	46.000000	AIR		
3	-0.022804	-43.852000	-43.852000	RFFI		
4	0.022804	43.852000	21.326000	RFFI		
5	0.	0.	0.600000	MATI 'GERM	4.002271	0.904
6	0.	0.	1.055000	AIR		
7	0.	0.	6.945000	AIR		
8	-0.050398	-19.842000	-6.945000	RFFI		
9	-0.096006	-10.416000	6.956927	RFFI		
10	0.	0.	0.	AIR		

REFRACTIVE INDICES

SURF	N1	N2	N3	N4	N5	ABBF
5	4.002271	4.002748	4.001945	1.000000	1.000000	3734.747383

CC AND ASPHERIC DATA

SURF	CC	AD	AE	AF	AG
3	-1.00000E 00				
4	-1.00000E 00				
6	0.	2.11239E-05	-1.77699E-07	1.58058E-08	-3.02054E-10
8	1.29076E 00				
9	2.47430E 00				

TILT AND DEC DATA

SURF	TYPE	YD	XD	ALPHA	BETA	GAMMA
1	DEC	0.	0.00000			
2	DEC	0.	-0.00000			
3	DEC	-6.00000	0.			
5	DEC	-6.00000	0.			

CLEAR APERTURES AND OBSTRUCTIONS

SURF	TYPE	CAY	CAX
6	CIRCLE	4.0000	
7 (OB)	ELLIPSE	1.2000	2.0000
8 (OB)	RECTANGLE	1.0000	2.5000

APERTURE STOP AT SURF 6

EVALUATION MODE IS FOCAL

CONTROL WAVELENGTH IS 1

PRIMARY CHROMATIC WAVELENGTHS ARE 2 - 3

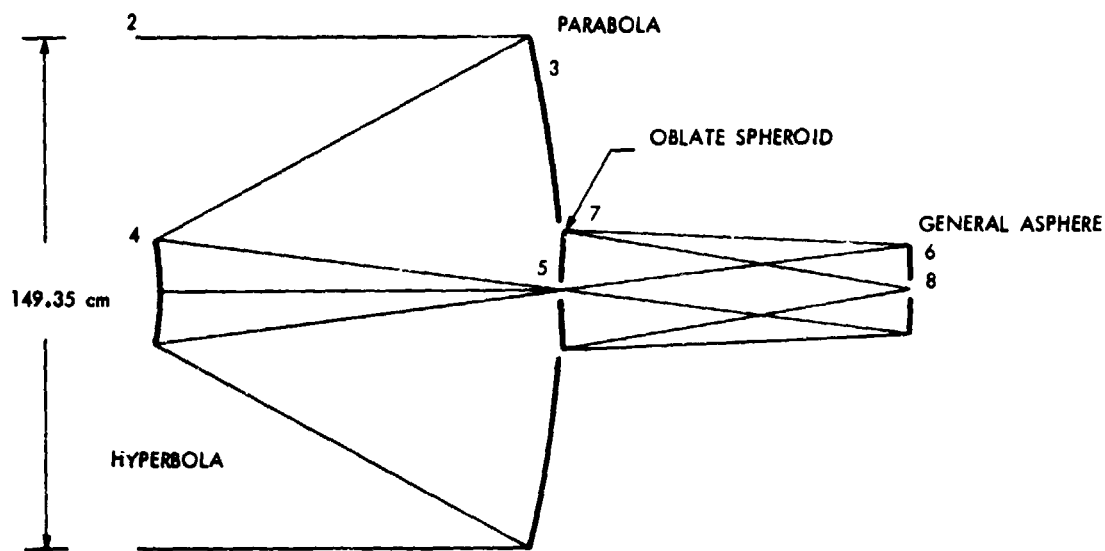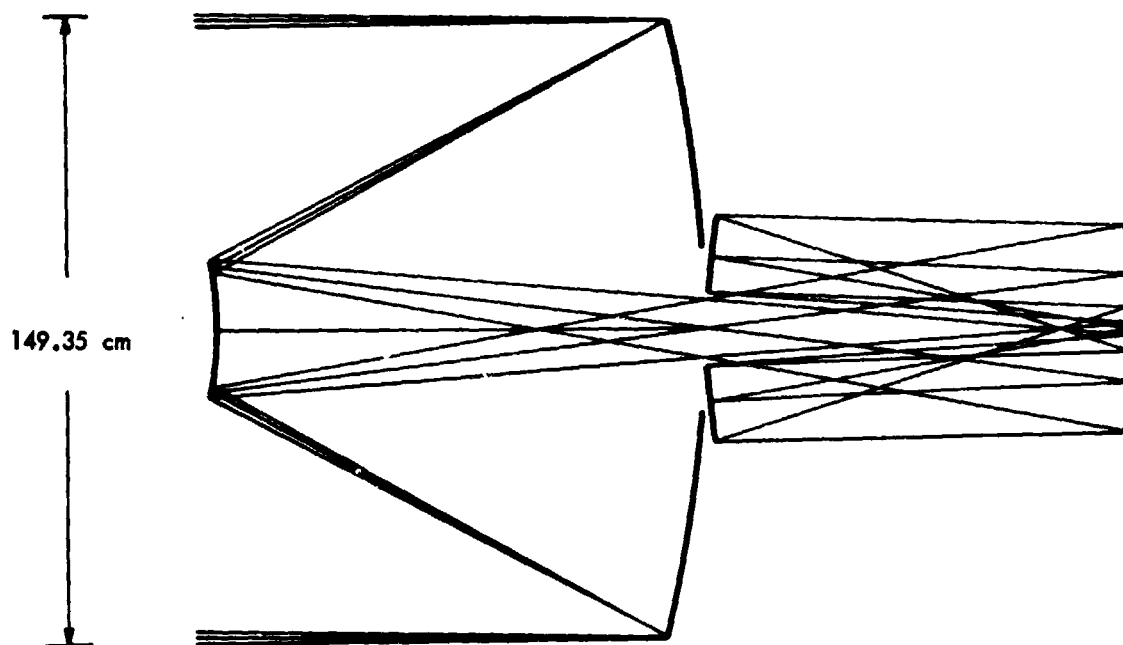SECONDARY CHROMATIC WAVELENGTHS ARE 2 - 1

3-11

Table 3-7. SEOS Optical Design Blur Characteristics

Field Angle (°)	90% Geometrical Blur Size	
	Tangential (mr)	Sagittal (mr)
0.0	0.001	0.001
0.33	0.001	0.001
0.46	0.001	0.002
0.66	0.001	0.002

Table 3-8. MTF CONTRIBUTIONS

Spatial Frequency		$\frac{1}{4 \cdot IFOV}$	$\frac{1}{3 \cdot IFOV}$	$\frac{1}{2 \cdot IFOV}$
Detector		0.90	0.83	0.64
CCD		0.99+	0.99+	0.99+
Optics	LEO Horizontal	0.83	0.77	0.67
	LEO Vertical	0.78	0.70	0.56
	Diffraction Limited (F/3)	(0.88)	(0.85)	(0.77)
	SEOS Horizontal	0.86	0.81	0.71
	SEOS Vertical	0.82	0.76	0.65
Square Mod Factor		1.7	1.10	1.16
MTF Product	LEO Horizontal	0.8	0.7	0.5
	LEO Vertical	0.75	0.64	0.42
	Diffraction Limited	(0.85)	(0.78)	(0.57)
	SEOS Horizontal	0.83	0.74	0.53
	SEOS Vertical	0.79	0.69	0.48
Required MTF		0.85	0.70	0.35

3-12

8103-07

The system MTF is calculated by combining the MTFs of the subsystems:

$$\text{MTF}(\text{system},f) = \text{MTF}(\text{detector},f) \times \text{MTF}(\text{optics},f) \times \text{MTF}(\text{CCD},f)$$

where f is spatial frequency. The individual subsystem contributions are each discussed below.

3.3.1   Detector MTF

The detector MTF is a simple sinc function:

$$\text{MTF}(\text{detector},f) = \frac{\sin(\pi a f)}{\pi a f}$$

where a is the detector dimension and has the value 100 μm.

3.3.2   Optics MTF

The MTF (optics,f) is found by means of a computer analysis of the proposed optical system. For comparison, we also calculated the MTF of an ideal, diffraction limited (i.e., no obscurations) optical system, having the same F-number as the proposed system:

$$\text{MTF (Diffraction Limited)} = \frac{2}{\pi} \left[\cos^{-1}\frac{f}{f_c} - \frac{f}{f_c} \left(\sin \cos^{-1}\frac{f}{f_c} \right) \right]$$

where
$$f_c = \frac{1}{\lambda F\text{-number}}; \quad \lambda = \text{average wavelength} = 11.5 \ \mu m$$
and
F-number = 3.

3.3.3   Electronics MTF

The contribution of the CCD can be expressed as

$$\text{MTF (CCD},f) = \frac{n \sin (\pi a f \ t_i/t_d)}{\pi a f \ t_i/t_d}$$

8103-07

where η = charge transfer efficiency = 0.99+

          t_i = CCD integraion time

          t_d = detector dwell time

        $A(f)$ = aliasing effect

The quantity
$$\frac{\sin(\pi a f t_i / t_d)}{\pi a f t_i / t_d} \approx 1$$

since the integration time will be on the order of microseconds and the dwell time is in milliseconds. In addition, $A(f) = 1$, that is, aliasing has almost no effect since the sample rate $1/t_i$ is so much faster than $1/t_d$ the high frequency limit for the signal information. Therefore, a good approximation is that the MTF (CCD,f) is 1 at all frequencies of interest.

3.3.4   System MTF

The results in Table 3-8 show that both the LEO and SEOS systems meet the requirements at the high frequency; the SEOS system is within 10% or better at the lower frequencies. To meet the specification at all frequencies we can work backwards to show that the optical design would have to have the following characteristics:

       F-number = F/1.4   Diffraction

       focal length = 59 cm (LEO)/448 cm (SEOS)   Limited

       diameter = 42 cm (LEO)/320 cm (SEOS)   System

as discussed earlier. The choices between fast/slow F-number, large/small aperture diameter, curved/flat focal plane, reflective/refractive design will have to be made when a sensor system using the TIRA focal plane is designed. The tradeoffs between the two cases discussed here are summarized in Table 3-9.

8103-07

Table 3-9. COMPARISON OF OPTICS DESIGNS

Small Aperture	Large Aperture
• Cannot meet the current MTF spec	• Can meet the current MTF spec
• Focal length = 59 cm (LEO) = 448 cm (SEOS)	• Same focal lengths
• F-number = 2.9 (LEO) 3.0 (SEOS)	• F-number = 1.4 (Diffraction Limited System)
• Aperture diameter = 20 cm = 150 cm (SEOS)	• Aperture diameter = 42 cm (LEO) = 320 cm (SEOS)
• Flat focal plane	• Curved focal plane
• No refractive elements	• Probably refractive elements
• Required D* = 8×10^9 (LEO) = 1.4×10^9 (SEOS)	• Required D* = 1.7×10^9 (LEO) = 0.3×10^9 (SEOS)

3.4 CHOPPERS

The basic requirements for the TIRA chopper are to modulate the incoming radiation by chopping a direct path to the focal plane, and to provide optical paths for radiation from two individual calibration sources to reach the focal plane. A tuning fork chopper which, in addition to the usual modulating function, will also serve as a two faceted mirror, seems best suited to these functions.

A sketch of the configuration for the chopper is shown in Figure 3-7. The length of the vanes is governed by the length of TIRA's focal plane as imaged at the chopping plane, which is about 4 in. To minimize the risk associated with the fabrication of a 4 in. chopper, two 2 in. choppers mounted back to back (master/slave) and synchronized to the same chopping frequency can be used (Figure 3-8). Such a scheme has been used successfully in the

8103-07

1 OPEN
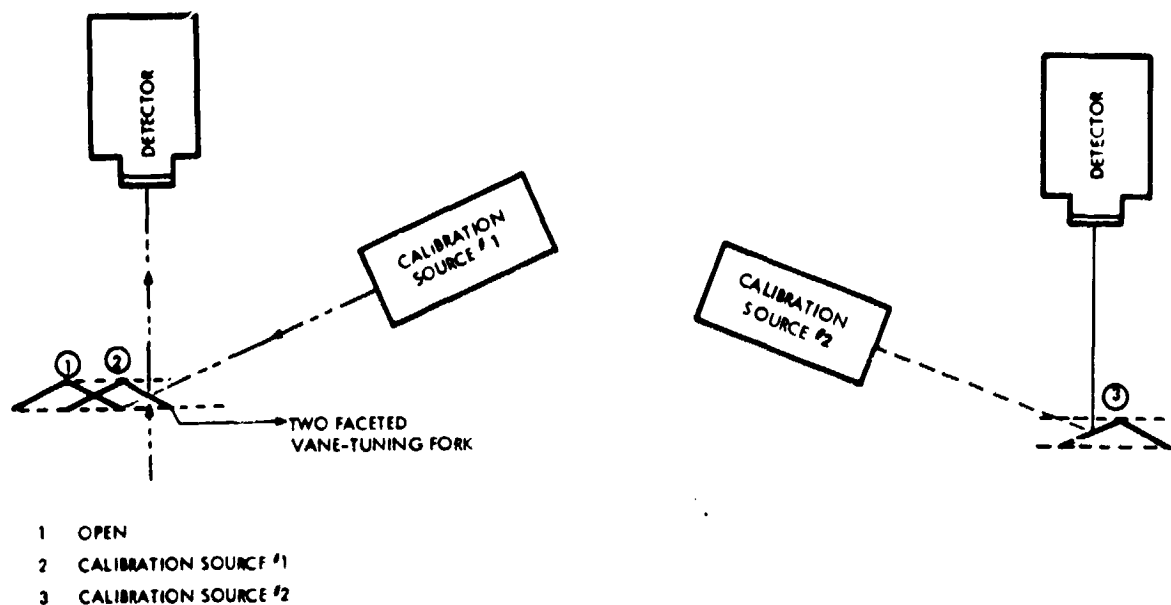2 CALIBRATION SOURCE #1
3 CALIBRATION SOURCE #2

Figure 3-7. A two-faceted chopper tine can be used to introduce
the calibration radiance.
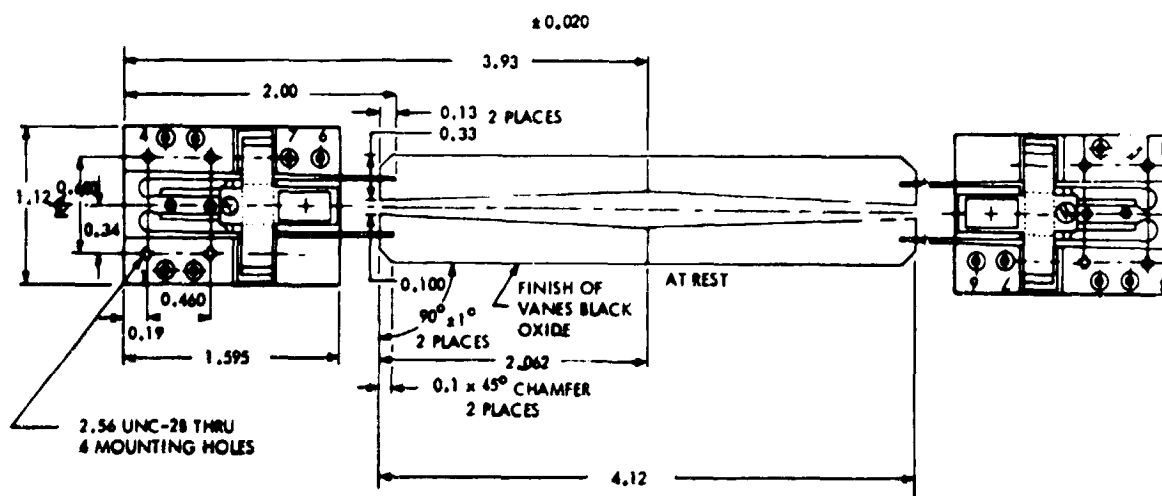
Figure 3-8. Back-to-Back Choppers Can be Synchronized to
Reduce the Required Tine Length.

3-16

8103-07

past. The choice of vane material will be governed primarily by the requirement that the two facets of the vane act as IR reflecting mirrors, and by the requirement to minimize weight yet maximize stiffness.

The chopping frequency to be used will be influenced by the opening space required and by the length of the vanes. Table 3-10 shows typical chopping frequencies for a given aperture and vane length. Because of the two faceted vane/mirror and the desire to have a uniform closing and opening of the chopper, the use of only one vane with a dummy load attached to the other tine may prove to be the best configuration for this application. Careful consideration will be given to the heat flow characteristics and the device geometry in order to minimize heat input to the vanes.

Table 3-10. FREQUENCY VS OPENING APERTURE FOR TIRA TYPE CHOPPER

TYPICAL FREQUENCY Hz	APERTURE mm (IN)	TINE AMPLTUDE mm (IN)
1000	1.2 (0.047)	0.6 (0.024)
800	2.0 (0.079)	1.00 (0.040)
600	2.5 (0.10)	1.25 (0.050)
500	3.2 (0.13)	1.6 (0.063)
400	5.0 (0.20)	2.5 (0.10)
300	5.8 (0.23)	2.9 (0.12)
200	8.0 (0.31)	4.0 (0.16)
150	10.0 (0.39)	5.0 (0.20)
100	10.0 (0.39)	5.0 (0.20)
50	10.0 (0.39)	5.0 (0.20)
30	10.0 (0.39)	5.0 (0.20)

3.5 FOCAL PLANE COOLING

The cooling specification of the TIRA focal plane requires operation at 105 K for up to a five year lifetime in either a LEO or a GEO orbit. As

8103-07

discussed earlier, the anticipated heat rejection of a 1 x 1000 element focal plane (16, 64 element modules) is currently estimated at < 140 mW, with dissipation through the collector resistors as the primary heat source. Designing for increased R_0 will help to reduce this load somewhat. With the addition of parasitics the final heat load used to size the cooler would be on the order of 200 mW. For either design providing 2 x 1000 elements (back-to-back modules or 2 detectors per module) the focal plane heat load will rise to < 280 mW, and the total load to about 340 mW.

The requirement to cool the detector focal plane reliably for 5 years in a space application at cryogenic temperatures immediately focuses attention on the use of a radiant cooling concept. For the GEOS configuration, the current passive radiator technology is more than adequate to fulfill the program requirements for cooling capacity, temperature range, and lifetime. Devices such as the Lockheed RM20A, a single stage system capable of providing 1 W of cooling capacity at 100 K is a candidate design. The RM20A is 1970 technology, so that improvements in coatings, insulation materials, and thermal characterization data should assure satisfactory performance for a future TIRA mission.

For the SEOS configuration, the adequacy of radiative cooling will depend upon the hour angle of the sun synchronous orbit selected. Terminator orbits provide sufficient solid angle to cold space so that 105 K can be maintained for a TIRA sensor. As the noon/midnight orbit is approached, the cooling constraints are more severe and will have to be addressed by future programs to design a TIRA sensor. However, the technology is improving. A new series of compact radiant coolers, developed by SBRC, will be used on the Thematic Mapper (TM). The TM cooler can provide 138 mW of cooling capacity at 88 K with a relatively small opening (52 cm^2 x 24 cm long) and the cooler weighs only 11 kilograms.

At this time, alternative cooling technologies have demonstrated lifetimes much too limited for TIRA. However, development of a magnetically mounted mechanical cooler may well achieve demonstrated long life on a time scale suitable for examination in a TIRA sensor program.

8103-07

3-18

3.6 COLD SHIELD

The cold shield reduces the background flux incident on the focal plane from the 300 K earth background and the 300 K sensor background; therefore the detector background noise is reduced. For TIRA, the detectors' predominant noise sources are the thermally generated carriers and the preamplifiers, not the background flux. Since the background noise is not a constraining factor in meeting the required sensitivity, (Table 3-11), a cold shield is not needed to help meet the sensitivity specifications; however, a shield might be considered for a TIRA sensor as a redundancy measure.

Table 3-11. EFFECT OF COLD SHIELD ON DETECTOR SENSITIVITY

D* (BLIP, F/3 OPTICS):		
Without Cold Shield	=	0.67×10^{11} cm-Hz$^{1/2}$/W
With Cold Shield	=	4.4×10^{11} cm-Hz$^{1/2}$/W
D* (REQUIRED, F/3 OPTICS):		
LEO	=	8.06×10^{9} cm-Hz$^{1/2}$/W
SEO	=	1.4×10^{9} cm-Hz$^{1/2}$/W

3.7 SYSTEMS SUMMARY

The thrust of the TIRA Phase I study was to design the focal plane array. However, system studies were included to investigate whether the LEO and SEOS missions would impose conflicting requirements on the focal plane design, to determine whether any specifications would result in unachievable requirements, and to insure that a sensor could be designed at a later time utilizing the TIRA focal plane design. The subsystems which were singled out as central to achieving a TIRA sensor capability were optics, system MTF, chopping (with calibration insertion), and focal plane cooling.

The conclusions resulting from these system studies are:

8103-07

- A single focal plane design will satisfy both mission configurations.

- Optical designs are are available which will meet the mission goals.

- MTF can be traded with optical complexity in a future study.

- A chopping mechanism can be devised which will modulate radiation to a 4 inch focal plane as well as insert two calibration sources at the required frequencies for chopping and calibration.

- Radiative cooling technology should be suitable for a future TIRA sensor in either mission configuration.

- Cold shielding is not a requirement but may be desirable.

3-20

APPENDIX A
1/f NOISE IN (Hg,Cd)Te PHOTODIODES

Reprinted from

A-1

8103-07

APPENDIX A

1/f Noise in (Hg, Cd)Te Photodiodes

STEPHEN P. TOBIN, MEMBER, IEEE, SHIGESATO IWASA, AND TIMOTHY J. TREDWELL

Abstract — In this article we present results of experiments to characterize 1/f noise in $Hg_{0.7}Cd_{0.3}Te$ n^+-on-p junction photodiodes. Under zero-bias voltage conditions, the photodiodes display no 1/f noise, even in the presence of large photocurrents. Under reverse-bias voltage operation, 1/f noise is observed. In these experiments, the 1/f noise was measured as a function of temperature, diode bias voltage, and photon flux. Since these parameters varied the relative contributions of the various current mechanisms, the diode current mechanism responsible for 1/f noise was isolated. It was found that 1/f noise is independent of photocurrent and diffusion current but is linearly related to surface generation current. It is proposed that 1/f noise in reverse-biased (Hg, Cd)Te photodiodes is a result of modulation of the surface generation current by fluctuations in the surface potential.

I. INTRODUCTION

EXCESS low-frequency noise, or 1/f noise, has been an area of extensive investigation in a wide variety of semiconductor devices. Reduction of 1/f noise is especially critical for infrared detectors due to the low frame rates at which many infrared imaging systems operate. The variable-bandgap semiconductor (Hg, Cd)Te has found wide applications as a photoconductor [1] for detection of 2-5-μm and 8-14-μm infrared radiation, due to its high electron mobility, long minority-carrier lifetime, and ease of preparation of low car-

rier concentration boules. Excess low-frequency noise in (Hg, Cd)Te photoconductors has been investigated by van der Ziel [2], who found a correlation between 1/f noise and the presence of grain boundaries, and Broudy [3], who related 1/f noise to surface potential variations and generation-recombination noise.

Recently, (Hg, Cd)Te photodiodes have been developed for both the 2-5-μm [4], [5] and the 8-14-μm [6] spectral regions. Because of the high impedance, low power dissipation, and linearity of photodiodes, high-density electronically scanned imaging arrays using (Hg, Cd)Te photodiodes are being developed [7]. However, 1/f noise in HgCdTe photodiodes has not previously been investigated.

The current noise generated by a photodiode consists of a number of components, including shot noise due to photogenerated current, shot noise and thermal noise due to thermally generated (dark) current, and 1/f noise. With the exception of 1/f noise, the noise mechanisms are well understood [8] and are predictable from the device characteristics. The shot-noise current due to a photocurrent I_ϕ is given by $i_n^2 = 2qI_\phi$. For a diode limited by diffusion current, the noise is the sum of the shot noise of the forward current $I_D \exp(qV/kT)$ and the shot noise due to the reverse current $-I_D$

$$i_n^2 = 2qI_D(\exp(qV/kT) + 1).$$

For depletion-layer generation-recombination current, the noise is the sum of the noise due to the generation current $I_G(V)$ and the noise due to the recombination current $I_R(V)$

$$i_n^2 = 2q(I_G(V) + I_R(V)).$$

The exact form of I_G and I_R depend, of course, on the junction profile, the trap energy, and cross sections. The measured

noise current of (Hg, Cd)Te photodiodes at frequencies above the $1/f$ "knee" is equal to the noise calculated from the above expressions.

$1/f$ noise has been extensively investigated in silicon p-n junctions and MOS transistors. In 1953, McWhorter [9] measured $1/f$ noise in semiconductor filaments and suggested that the $1/f$ noise originated in trapping of carriers by surface states. Later, Noble and Thomas [10] found experimentally that exposure of germanium filaments to various atmospheres resulted in variations in low-frequency noise and suggested that atmospheric exposure altered surface trapping by affecting the surface potential. Watkins [11] found that surface treatment affected $1/f$ noise in germanium junctions and Atalla [12] observed similar effects in silicon junctions. The first quantitative investigation of the correlation between surface-state density and $1/f$ noise was made by Sah and Hielscher [13]. A number of investigators have since related $1/f$ noise in MOS transistors to charge trapping in surface states [14]-[17]. The first direct demonstration of the relationship between surface states and $1/f$ noise in p-n junctions was made by Hsu et al. [18]-[20]. In these experiments, a correlation between surface-state density and diode $1/f$ noise was observed in silicon gated diodes.

Preliminary investigations of $1/f$ noise in $Hg_{0.6}Cd_{0.4}Te$ photodiodes [4] had shown that the photodiodes displayed no $1/f$ noise to at least 0.1 Hz when operated under zero-bias conditions. This has since been confirmed on a large number of devices covering the 2- to 5 μm spectral region (gap energies from 0.62 to 0.25 eV) over a wide temperature range. The diodes display no $1/f$ noise even under strong infrared illumination under zero-bias conditions. Since in most applications the diode current is amplified by a low-impedance amplifier, an illuminated diode remains unbiased and no $1/f$ noise is observed. Under certain conditions requiring low capacitance or high dynamic impedance, reverse bias may be required. Under reverse bias, $1/f$ noise is observed. The objective of the experiments reported herein was to isolate the mechanism responsible for the $1/f$ noise under reverse-bias operation.

II. EXPERIMENT

The photodiodes used in these experiments were fabricated from p-type $Hg_{0.7}Cd_{0.3}Te$. The (Hg, Cd)Te boule was grown by the controlled solidification technique. Wafers were cut, lapped, polished, and etched to remove all damage, then passivated with a layer of ZnS. Junctions were formed by ion implantation of 100-keV boron ions. Contact holes were etched through the passivation and indium contacts made to the n^+ side of the junction. Gold was used for the p-side backside contact. The photomask used to define the junction implant contained diode areas from 1.29×10^{-5} cm^2 to 4.8×10^{-4} cm^2. This allowed separation of bulk-related current generation (which increases as the junction area) and surface-related current generation (which increases as the junction perimeter).

The experimental arrangement for the noise current measurements consisted of a low noise bias supply for the diode, a low noise current-sensitive preamplifier, an additional preamplifier stage, and a Fourier-transform spectrum analyzer. The diode arrays were mounted in a variable-temperature cryostat
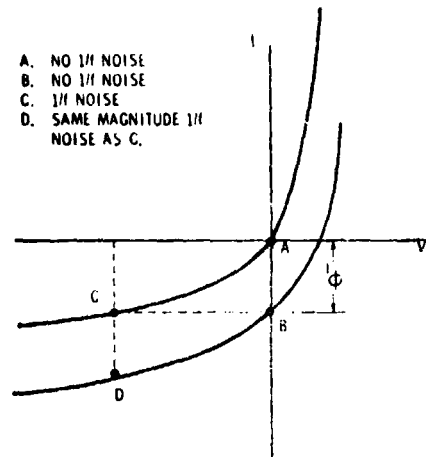

Fig. 1. Effect of background flux on (Hg, Cd)Te photodiode $1/f$ noise.

in which modifications had been made to eliminate microphonics. Noise current was normally measured from 2 to 2000 Hz.

The experiments consisted of measuring the $1/f$ noise as a function of photon flux, diode temperature, and diode bias voltage. By varying these parameters, the relative contributions of various current generation mechanisms (photocurrent, diffusion current, depletion-layer generation current, and surface generation current) could be varied and the mechanism(s), if any, related to $1/f$ noise isolated.

III. EXPERIMENTAL RESULTS

A. $1/f$ Noise and Photocurrent

The effect of current generated in (Hg, Cd)Te photodiodes by infrared illumination is illustrated in Fig. 1. At zero bias and without any illumination (A) no $1/f$ noise is observed. When photocurrent is generated by exposing the junction to background infrared radiation (B), the total noise is observed to increase due to the added shot noise of the photocurrent I_ϕ ($i_n^2 = 2qI_\phi$) but no $1/f$ noise is observed. When the junction is reverse biased without illumination (C), $1/f$ noise is observed. When the diode is reverse biased and illuminated by background radiation (D), the total noise increases due to the added shot noise of the photocurrent. However, no additional $1/f$ noise is observed.

The absence of $1/f$ noise at zero applied bias in the presence of large photocurrents has been verified for (Hg, Cd)Te photodiodes for a number of devices and over a wide range of temperatures. The result indicates that the $1/f$ noise is not simply related to the total current in the diode, but rather depends on the mechanism by which the current was generated. $1/f$ noise originating in metal-semiconductor contacts or in current flow through the diode are thus ruled out, as these mechanisms would result in $1/f$ noise independent of the means by which the diode current was generated.

B. $1/f$ Noise and Dark Current

In order to determine if any relationship exists between $1/f$ noise in reverse-biased diodes and dark current, both $1/f$ noise and dark current were measured on a number of photodiodes on the same chip. The noise current data were obtained at

(a)

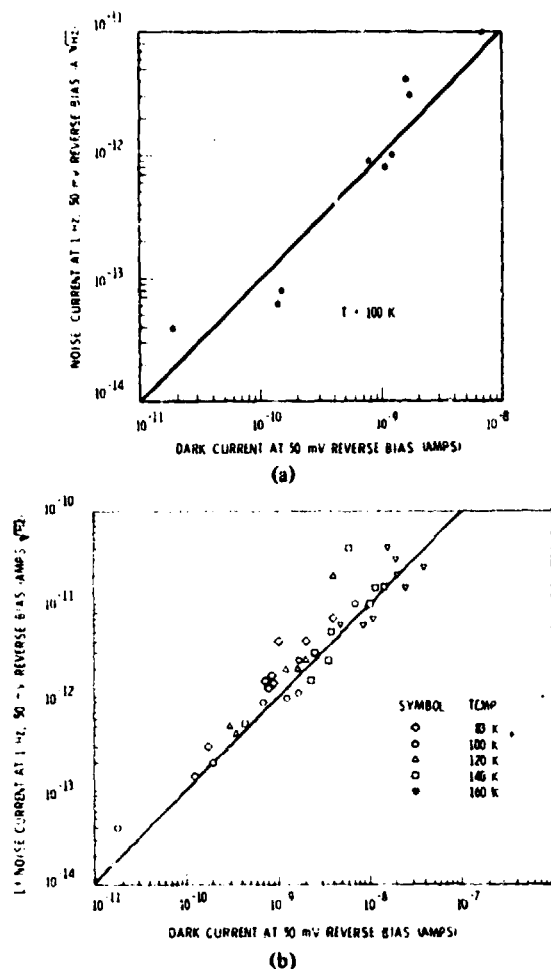| SYMBOL	TEMP
◊	80 K
o	100 K
▲	120 K
□	146 K
●	160 K

(b)

Fig. 2. (a) 1/f noise current (1 Hz, -50 mV) versus dark current (-50 mV) at 100 K, showing linear dependence. (b) 1/f noise current as a function of dark current, for a range of temperatures.

50-mV reverse bias over a frequency range of 2 Hz to 2 kHz. The 1/f noise component is expressed as $i_n = I_{1/f} f^{-1/2}$ where $I_{1/f}$ is the 1/f noise current extrapolated to 1 Hz. The dark current was also measured at 50-mV reverse bias.

The relationship between 1/f noise and dark current is shown in Fig. 2(a) for a diode temperature of 100 K. The data indicate a linear relationship between 1/f noise current and dark current of the form

$$i_n(f) = \alpha I^\beta f^{-1/2} \qquad (1)$$

where α and β are empirical parameters. The data are fit with $\alpha \simeq 1 \times 10^{-3}$ and $\beta = 1$.

Similar data for these diodes have been obtained at temperatures from 80 to 246 K. The linear relationship between dark current and 1/f noise current was observed to hold for temperatures between 80 and 180 K. For temperatures above 180 K. which correspond to the onset of significant diffusion current as opposed to surface or junction depletion-layer generation currents, the linear relationship was no longer observed. Fig. 2(b) shows 1/f noise current as a function of dark current for the temperature range 80 to 160 K for a number of photodiodes in a single chip. Both 1/f noise and dark current were measured at 50-mV reverse bias. The data may be fit with

(1) with $\alpha = 1 \times 10^{-3}$ and $\beta = 1$. The data suggest that 1/f noise in (Hg, Cd)Te photodiodes is related to surface or bulk depletion-layer generation currents but is not related to diffusion current.

C. Temperature Dependence of 1/f Noise

The temperature dependence of the 1/f noise current provides a means of sorting out which thermal generation mechanisms are related to 1/f noise. Fig. 3(a) shows dark current as a function of temperature for a $Hg_{0.7}Cd_{0.3}Te$ photodiode. The dark current was measured at 50-mV reverse bias. At temperatures above 180 K, the diode dark current is predominantly diffusion current

$$I_D = Aq \sqrt{\frac{kT}{q} \frac{n_i^2}{N_A}} \sqrt{\mu_e/\tau_e}$$

where n_i is the intrinsic carrier concentration, N_A is the acceptor concentration in the n^+-p junction, and μ_e and τ_e are the minority carrier electron mobility and lifetime. Below 180 K, the diode dark current is proportional to n_i, indicating either depletion-layer or surface generation current. The depletion-layer generation current is given by

$$I_G = \tfrac{1}{2} qAn_i Wf(b)/\sqrt{\tau_{n0}\tau_{p0}}$$

where W is the depletion layer width, A the junction area, τ_{n0} and τ_{p0} the electron and hole lifetimes, and $f(b)$ a parameter depending on trap energy and junction parameters. The surface generation current in a short surface channel [21] is given by

$$I_s = 2qn_i s_0 A_s$$

where A_s is the surface area effective in generation (diode perimeter times surface channel length) and s_0 is the surface generation velocity. The diodes in these experiments ranged in area from 1.29×10^{-5} cm^2 to 4.8×10^{-4} cm^2, allowing separation of surface and bulk depletion-layer generation currents. The dark current at reduced temperatures was observed to increase in proportion to the junction perimeter rather than the junction area, suggesting that surface generation was predominant in these devices.

At even lower temperatures, below the surface generation regime, some of the diodes displayed a temperature-independent surface leakage current.

The temperature dependence of the 1/f noise current (also measured at 50-mV reverse bias) is shown in Fig. 3(a). At temperatures below 180 K, where the diode dark current is predominantly surface generation current ($I_D \propto n_i$), the 1/f noise current displays the same temperature dependence as the dark current ($i_n \propto n_i$). The magnitude of the 1/f noise is related to the magnitude of the dark current by (1). At temperatures above 180 K, the junction dark current is predominantly diffusion current ($I_D \propto n_i^2$). The 1/f noise, however, continues to display the temperature dependence of the surface generation current ($i_n \propto n_i$). Additional data obtained from other devices at temperatures between 190 and 246 K are shown in Fig. 4. Again, the dark current is proportional to n_i^2 (diffusion current) while the 1/f noise is proportional to n_i.

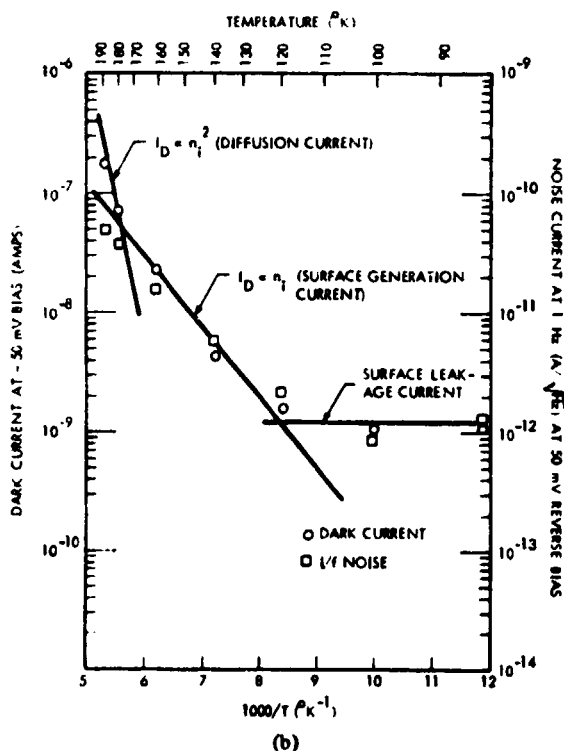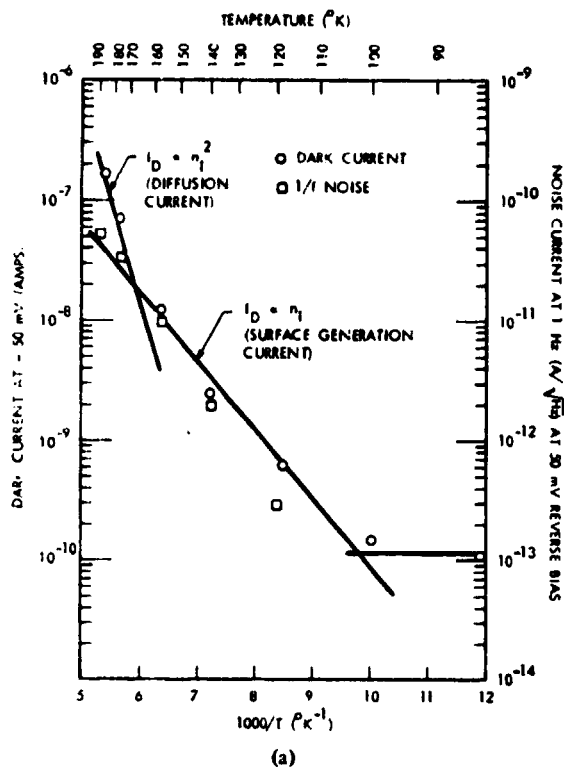The temperature dependence of the dark current and 1/f

(a)

(b)

Fig. 3. (a) Temperature dependence of dark current and $1/f$ noise current, Element 4. (b) Temperature dependence of dark current and $1/f$ noise current, Element 2.

noise for a photodiode which displayed significant surface leakage is shown in Fig. 3(b). At temperatures between 120 and 180 K, the diode dark current was predominantly surface generation current ($I_D \propto n_i$). The $1/f$ noise also increased as n_i. At temperatures above 180 K, the diode dark current was
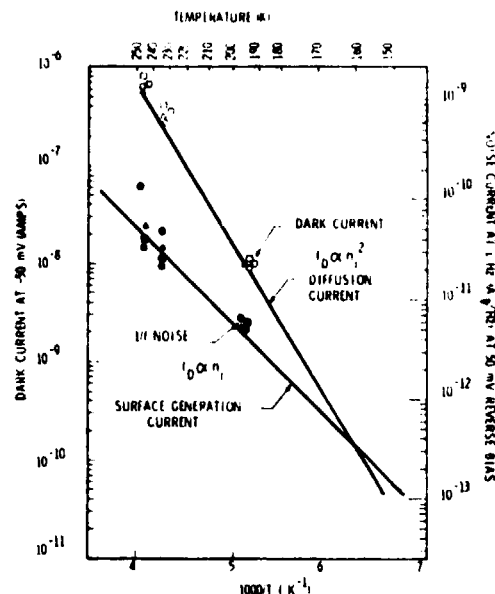

Fig. 4. Temperature dependence of dark current and noise current, for several elements of an array. $1/f$ noise does not depend on diffusion current.

predominantly diffusion current ($I_D \propto n_i^2$); the $1/f$ noise, however, continued to vary as n_i. At temperatures below 120 K, the junction dark current consisted of a temperature-independent surface leakage; the $1/f$ noise displayed the same temperature dependence as the dark current, suggesting that $1/f$ noise is related to surface leakage as well as generation current. Data of dark current and $1/f$ noise as functions of temperature were obtained from a number of other devices in the same array; these data display the same features as the two examples shown in Fig. 3. In all cases, the $1/f$ noise was found to be related to the surface generation and leakage current components of the dark current by (1).

D. Bias Voltage Dependence of $1/f$ Noise

The bias voltage dependence of $1/f$ noise has been examined in detail on a few $Hg_{0.7}Cd_{0.3}Te$ photodiodes. Data were obtained by measuring both dark current and $1/f$ noise at several reverse biases. At temperatures above 180 K, the photodiode dark current was predominantly diffusion current and the dark current-voltage relationship $I = I_s [\exp(qV/kT) - 1]$ was observed. At lower temperatures, where the dark current varied in temperature as n_i, the current-voltage relationship was more complex; at small reverse biases and moderate temperatures the relationship was approximately $I = I_0 [\exp(qV/2kT) - 1]$; at larger reverse biases and at low temperatures, a resistive leakage current was observed. At temperatures where diffusion current was unimportant ($T < 160$ K), the $1/f$ noise was found to vary with reverse bias in the same manner as the dark current. This linear relationship between $1/f$ noise and dark current is shown in Fig. 5(a) for a $Hg_{0.7}Cd_{0.3}Te$ photodiode at 77 K. The data, obtained by measuring both $1/f$ noise and dark current at a number of reverse biases, suggest that $1/f$ noise depends on bias only through the dependence of dark current on reverse bias. This behavior was observed on all devices tested.
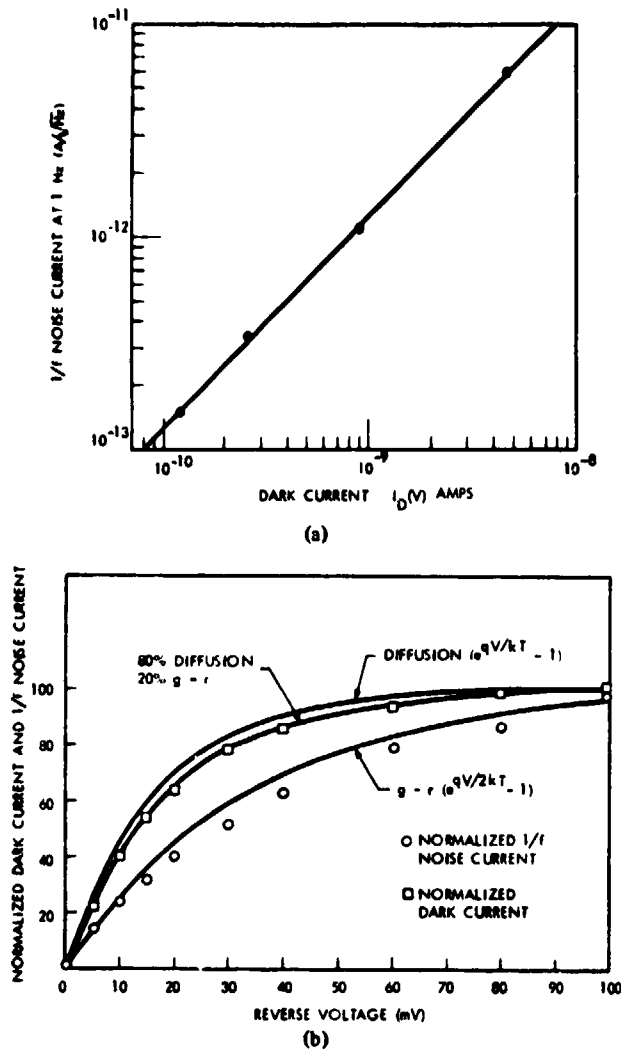
Fig. 5. (a) 1/f noise current as a function of dark current for a (Hg, Cd)Te photodiode at 77 K. Dark current was varied by varying reverse bias; both dark current and 1/f noise were measured at several reverse biases. (b) Dark current and 1/f noise current as a function of reverse bias, for a (Hg, Cd)Te photodiode at 193 K. Dark current is predominantly (~80 percent) diffusion current.

At temperatures above 180 K, diffusion current is predominant and the voltage dependence of the 1/f noise is different than that of the dark current.

Figure 5(b) shows 1/f noise and dark current as functions of bias voltage for a $(Hg_{0.7}Cd_{0.3})Te$ photodiode at 193 K. The dark current, which is mostly composed of diffusion current, displayed an exp $(qV/kT) - 1$ bias dependence. The 1/f noise current, however, displayed a bias dependence of approximately exp $(qV/2kT) - 1$. This latter bias dependence is associated with surface or depletion-layer generation current. This bias dependence of the 1/f noise suggests that only the surface generation current component of the total dark current is related to the 1/f noise.

IV. DISCUSSION

We have measured 1/f noise in (Hg, Cd)Te photodiodes as a function of temperature, diode bias, dark current, and photon flux. By varying each of these parameters, the relative con-

tributions of each of the various current mechanisms could be varied, allowing those mechanisms associated with 1/f noise to be isolated. The 1/f noise was found to be independent of photocurrent over a wide range of photon flux levels at several diode biases. These data rule out 1/f noise mechanisms such as contact noise which would be independent of the origin of the diode current. The dependence of 1/f noise on dark current was measured over a wide temperature range on devices with various junction areas. At low temperatures, where surface generation and leakage current were predominant, a linear relationship between 1/f noise and dark current was observed. At higher temperatures, where diffusion current is predominant, the correlation no longer holds. The temperature dependence of 1/f noise was also determined. The temperature dependence of the 1/f noise was found to be the same as the temperature dependence of the surface generation and leakage currents. At elevated temperatures, where diffusion current was predominant, the 1/f noise continued to follow the temperature dependence of the surface generation current. The bias dependence of the 1/f noise was examined. At temperatures where diffusion current is not important, the 1/f noise displays the same bias dependence as the dark current. At higher temperatures, where diffusion current is predominant, the bias dependence of the 1/f noise appears to follow the bias dependence of the surface generation component of the dark current. All the data obtained in these experiments could be fit by a simple relationship between 1/f noise and dark current

$$i_n(f, V, T) = \alpha I_s(V, T) f^{-1/2}$$

where I_s is the surface generation and leakage current. The coefficient α was approximately 1×10^{-3} for all devices tested to date. We conclude that 1/f noise in (Hg, Cd)Te photodiodes varies with diode bias, temperature, and dark current only through the dependence of the surface current on these parameters. Because of the surface-limited dark current on these devices, it was not possible to determine what, if any, role junction depletion-layer generation current may play in 1/f noise.

A similar relationship between surface generation-recombination current and 1/f noise was observed in silicon gated diodes by Hsu. Hsu proposed a model in which the current fluctuations are a result of modulation of the surface generation current by fluctuations in surface potential. The data on these (Hg, Cd)Te photodiodes could be explained by such a model. However, a better understanding of the nature of the surface-channel current and its dependence on surface potential in (Hg, Cd)Te photodiodes is required. The significant similarities between the behavior of 1/f noise in (Hg, Cd)Te photodiodes and its behavior in silicon surface-channel FET's and gated diodes suggests that further investigation into interface properties of (Hg, Cd)Te and their relationship to junction behavior will be fruitful.

REFERENCES

[1] A recent review of HgCdTe detector technology, with references, was presented by M. B. Reine and R. M. Broudy at the 21st S.P.I.E. Technical Symposium, San Diego, CA, August, 1977.
[2] H. I. Hanafi and A. van der Ziel, Solid-State Electron., vol. 21, p. 1019, 1978.

[3] R. M. Broudy, "Study to improve the low frequency noise characteristics of (Hg, Cd)Te detectors." Final Tech. Rep. (Apr. 1971–Aug. 1973), NASA Contract No. NAS1-10682.

[4] T. J. Tredwell, "Advances in 2 to 5-μm (Hg, Cd)Te photodiodes," in *1976 Int. Electron Devices Meeting Proc.* (Washington, DC, Dec. 1976).

[5] T. J. Tredwell, *Opt. Eng.*, vol. 16, p. 237, 1977.

[6] A. Sood and T. Tredwell, in *1978 Int. Electron Devices Meeting Proc.*, (Washington, DC, Dec. 1978).

[7] R. Broudy, M. Gurnee, S. Iwasa, T. Tredwell, and J. White, "IR/CCD hybrid focal planes," *S.P.I.E. Proc.*, vol. 132, "Utilization of infrared detectors," 1978.

[8] See, for example, A. van der Ziel and E. Chenette, in *Advances in Electronics and Electron Devices*, vol. 46, L. Marton, Ed. New York: Academic Press, 1978.

[9] A. L. McWhorter, "1/f noise and germanium surface properties," in *Semiconductor Surface Physics* (U. Penn., 1957) p. 207.

[10] V. E. Noble and J. E. Thomas, *J. Appl. Phys.*, vol. 32, p. 1709, 1961.

[11] T. B. Watkins, *Proc. Phys. Soc.*, vol. 73, p. 59, 1954.

[12] M. M. Atalla, E. Tannenbaum, and E. J. Scheibner, *Bell Syst. Tech. J.*, vol. 38, p. 749, 1959.

[13] C. T. Sah and F. H. Hielscher, *Phys. Rev. Lett.*, vol. 17, p. 956, 1966.

[14] L. M. Terman, *J. Solid State Electron.*, vol. 5, p. 285, 1962.

[15] E. H. Nicollian and H. Melchior, *Bell Syst. Tech. J.*, vol. 46, p. 1055, 1967; and vol. 46, p. 2019, 1967.

[16] H. Prier, *Appl. Phys. Lett.*, vol. 10, p. 3611, 1967.

[17] S. Christensson, I. Lundstrom, and C. Svensson, *Solid-State Electron.*, vol. 11, p. 797, 1968; and vol. 11, p. 813, 1968.

[18] S. T. Hsu, *Solid-State Electron.*, vol. 13, p. 1451, 1970.

[19] —, *Appl. Phys. Lett.*, vol. 12, p. 287, 1968.

[20] —, *Solid-State Electron.*, vol. 13, p. 843, 1970.

[21] F. R. Pierret, *Solid-State Electron.*, vol. 17, p. 257, 1974.

APPENDIX B

CURRENT MECHANISMS AND 1/f NOISE IN 8 to 12 μm n$^+$ on p (Hg,Cd)Te PHOTODIODES

Reprinted from

1980 International Electron Devices Meeting Technical Digest

B-1

8103-07

APPENDIX B

CURRENT MECHANISMS AND 1/f NOISE IN 8-12 μm n+ ON p (Hg,Cd)Te PHOTODIODES*

R.J. Briggs, J.W. Marciniec, P.H. Zimmermann, and A.K. Sood

Honeywell Electro-Optics Center

2 Forbes Road

Lexington, Massachusetts 02173

ABSTRACT

Process improvements have enabled fabrication of boron-implanted 8-12 μm n+ on p $Hg_{0.8}Cd_{0.2}Te$ junction photodiodes with reduced generation-recombination (G-R) current and 1/f noise. In this paper the current-voltage characteristic (I-V) is successfully modeled for the first time in (Hg,Cd)Te using the temperature dependence of diffusion and G-R currents. The photodiode area dependence indicates that the G-R current is surface in nature and described by a depletion surface recombination velocity, measured at $S_0 = 2 \times 10^6$ cm/s. Using this I-V modeling technique to quantitatively determine S_0, improvements reduced S_0 to 4×10^4 cm/s. Detector bias has a strong effect on 1/f noise, with minimum 1/f noise occuring at zero bias. Correlation of this 1/f noise in 3-5 μm (Hg,Cd)Te photodiodes with surface G-R was recently reported. Present 8-12 μm (Hg,Cd)Te photodiodes are shown to have a similar correlation over the S_0 range observed.

INTRODUCTION

$Hg_{1-x}Cd_xTe$ junction photodiodes are being developed for use in hybrid mosaic focal arrays for a wide variety of applications both for 3-5 μm and 8-14 μm. While most attention has been given to devices with cut-off wavelengths between 3-5 μm for operation at a temperature around 190K, devices with cut-off wavelength of 8-12 μm and longer are beginning to receive increased emphasis for operation at 70K and lower temperatures.

Recent work on the photovoltaic devices for 8-12 μm applications has shown it is possible to obtain bulk diffusion current limited performance down to 80K (1,2,3,4). For temperatures below 80K, however, these photodiodes show a deviation in the current-mechanism from diffusion to either generation-recombination (G-R) or or some form of surface leakage (5,6). The G-R current mechanism can either be in the depletion region away from the surface, in which case it will be classified as "bulk generation-recombination", or be where the junction terminates at the surface, in which case it is classified as the "surface generation-recombination" current. This paper presents theoretical and experimental analysis indicating that the G-R

currents in present photodiodes originate in the space charge region near the surface.

PHOTODIODE FABRICATION

The photodiodes were fabricated from bulk grown p-type $Hg_{1-x}Cd_xTe$ wafers with 0.216 < x < 0.227. The fabrication details have been discussed elsewhere (6).

PHOTODIODE DIFFUSION AND G-R CURRENTS

Currents resulting from several mechanisms may limit n+ on p photodiode performance for any given temperature and cutoff wavelength. Although the forward and reverse currents cancel for the mechanism at zero bias, the associated noise does not (7). At higher temperatures performance may be limited either by diffusions of thermally generated current, bulk space G-R currents, or surface G-R currents. This section demonstrates how to distinguish the three currents using their characteristic temperature, voltage, and area dependences.

At higher temperatures the dominant current arises from diffusion of thermally generated electronics from the p-side of the junction and thermally generated holes from the n-side to the junction. This so-called diffusion current is proportional to the number of minority carriers on each side of the junction. Since the volume from which diffusion current may arise is much larger on the p-side than on the n-side and the number of minority carriers is much larger, the diffusion currents for n+ on p photodiodes are almost all from the p-side. The diffusion current I_D and zero bias impedance R_0 can be expressed in the planar approximation as (8):

$$I_D = I_S (e^{qV/kT}-1) \qquad (1)$$

$$I_S = A_J \frac{q^2}{kT} \frac{n_i^2}{N_A} \frac{\mu_e}{L_e} \qquad (2)$$

$$R_0 (diff) = \frac{kT}{qI_S} \qquad (3)$$

where A_J = junction area

n_i = intrinsic carrier concentration

N_A = acceptor concentration

L_e = minority carrier electron diffusion length

μ_e = minority carrier electron mobility

τ_e = minority carrier lifetime

A second current mechanism results from thermal generation and recombination (G-R) of electron-hole pairs in the region of the junction between the n and p-sides which is depleted of both types of minority carriers. The so-called space charge G-R current is proportional to the intrinsic carrier concentration n_i. This G-R current and associated limitation to R_0 is given by (9):

$$I_{GR} = I_0 \frac{2 \sinh (qV/2kT)}{\sqrt{1 - V/V_{bi}}} f(b) \qquad (4)$$

$$R_0(\text{G-R}) = \frac{kT}{q I_0 f(b)} \qquad (5)$$

where

$$b = e^{-qV/kT} \cosh \epsilon_t \qquad (6)$$

$$f(b) = \int_0^\infty \frac{du}{1 + 2bu + u^2} \qquad (7)$$

and

$$I_0 = \frac{n_i W_0 A_J}{\tau_0} \frac{kT}{V_{bi}} \qquad (8)$$

or

$$I_0 = n_i S_0 W_0 P \frac{kT}{V_{bi}} \qquad (9)$$

for depletion layer or surface g-r, respectively. Here V_{bi} is the depletion built in voltage, W_0 is the depletion width as zero bias, $\tau_0 = \sqrt{\tau_{no} \tau_{po}}$ is the effective depletion layer lifetime, P is the junction perimeter and S_0 is the surface recombination velocity inside the depletion region where it intersects the semiconductor surface. For the most effective G-R center, at zero bias $b = \cosh \epsilon_t = 1$, and $f(b) = 1$.

The temperature dependences of both current mechanisms are almost entirely due to the intrinsic carrier concentration. Since R_0A (G-R) $\propto n_i^{-2}$, performance should be limited by

diffusion currents at higher temperature and at somewhat lower temperatures by generation-recombination currents. Since $n_i \propto \exp (-Eg/2kT)$ the transition temperature between diffusion current and G-R current limitation is inversely proportional to device cutoff wavelength λ_{co}.

PHOTODIODE AREA DEPENDENCE

Careful analysis of the area dependence of photodiode currents should allow separation of bulk from perimeter effects, specifically, separation of depletion layer G-R from surface G-R. Figure 1 shows a graph of $(R_0A_J)^{-1}$ vs the P/A_J ratio for all elements of a variable area diode array having 10.6 μm at 80 K.

The data in the figure has been modeled using the equation (10,11)

$$(R_0 A_J)^{-1} = (R_0 A)^{-1}_{\text{Bulk}} + \frac{q n_i S_0 W_0}{V_{bi}} \frac{P}{A_J} \qquad (10)$$

to separate the bulk from the surface currents, where the notations are as already defined. The intercept of the graph indicates a bulk contribution to R_0A of 9 ohm-cm^2; the slope indicates a depletion surface recombination velocity of $S_0 = 1.7 \times 10^6$ cm/sec. The temperature dependence of the various elements can be modeled at higher temperature by diffusion current. Extrapolation of this diffusion limit to 80 K gives an R_0A of 9 ohm-cm^2, consistent with the intercept in Figure 1. Hence, the bulk
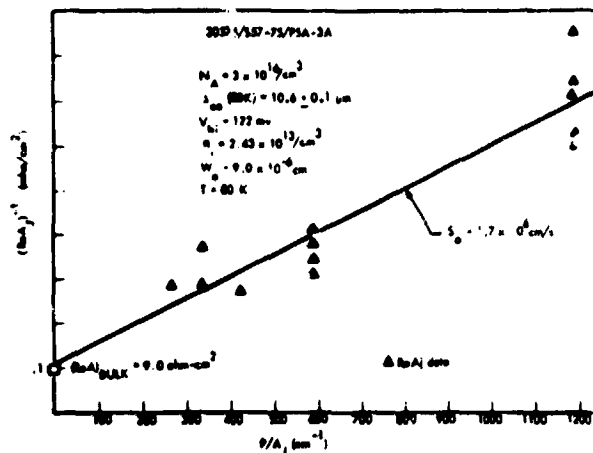

Figure 1. Graph of $(R_0A_J)^{-1}$ vs. (P/A_J) for all elements of a 10.6 μm variable area photodiodes array at 80 K. Intercept indicates bulk contribution to R_0A of 9 ohm-cm^2 and slope indicates $S_0 = 1.7 \times 10^6$ cm/s.

currents in this array at 80 K are due to diffusion current and the G-R currents are almost entirely a surface G-R.

DIODE CURRENT-VOLTAGE MODELING

In the preceding section successful separa-
tion of bulk G-R from surface G-R was demon-
strated. In this section it will be shown that
careful modeling of photodiode current vs. volt-
age (I-V) curves should allow unambiguous sepa-
ration of diffusion currents from generation-
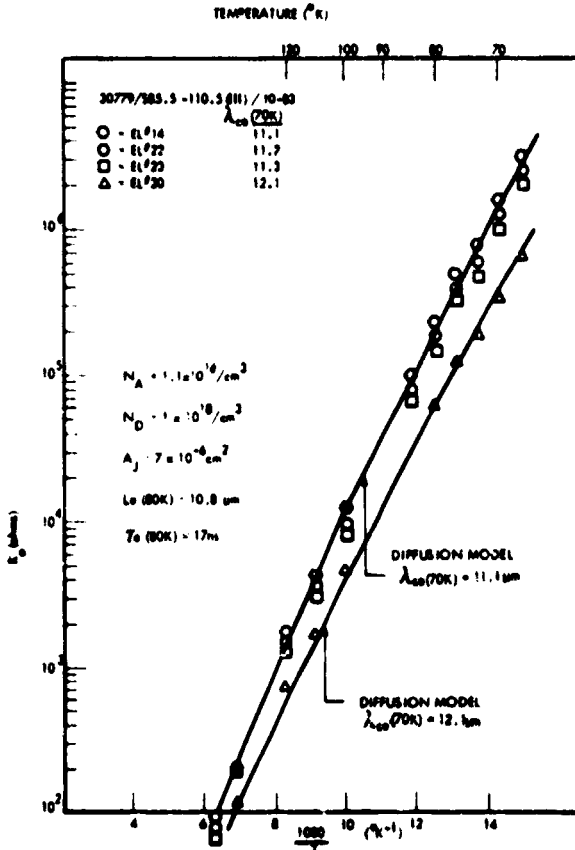recombination currents. Figure 2 shows the

Figure 2. Temperature dependence of R_O for
four elements of a photodiode array
diffusion limited down to almost 65
K. R_O falls off monotonically with
wavelength.

temperature dependence of R_O for four elements
from a small area photodiode array. These are
the first reported diodes of this wavelength
which are diffusion limited down to such a low
temperature, nearly 65 K in this case. Figure 3
shows I-V modeling for element #23 of the array
at 70 K and 80 K. The model consists of a sum
of diffusion and G-R currents:

$$I = I_s(e^{qV/kT}-1) + I_o \frac{e^{qV/2kT}-e^{-qV/2kT}}{\sqrt{1-V/V_{bi}}} f(b) \quad (11)$$
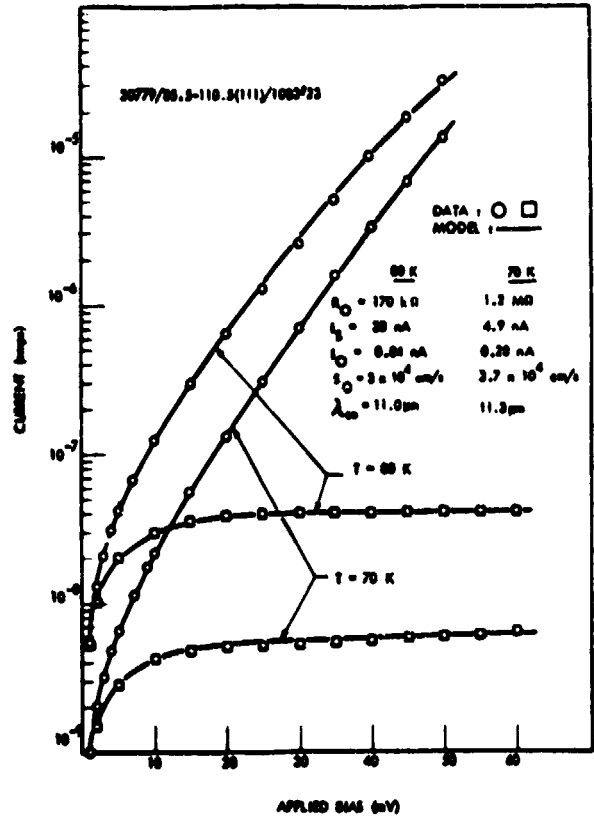

Figure 3. Forward and reverse I-V characteris-
tics at 70 K and 80 K for element #23
of the array shown in Figure 2.
Modeling parameters indicated.

As indicated in the figure, at 70 K the I-V
characteristic is fit using I_s = 4.9 nA and
I_o = 0.28nA to describe the diffusion and G-R
currents, respectively. The G-R current is
interpreted as surface G-R with an associated
depletion surface recombination velocity of S_O
= 3.7 x 10^4 cm/s.

PHOTODIODE 1/f NOISE

The noise sources associated with a photo-
diode are Johnson noise due to the junction
resistance R_O, background induced noise cur-
rent, and 1/f noise i_f, giving total noise
density of

$$i_n^2/\Delta f = \frac{4kT}{R_O} + 2nq^2 \psi_B A + i_f^2/\Delta f \quad (12)$$

where ψ_B is the background flux, k is Boltz-
man's constant, and Δf is the bandwidth.

The detector bias has a strong effect on 1/f noise, with minimum 1/f noise at zero bias (12). Figure 4 shows a typical noise current spectrum at 70 K for a 11.7µm small area photodiode. Quantitative values for the various performance parameters are given in Table I for comparison with other arrays. Recent experiments of 1/f noise in 3-5µm $H_{1-x}Cd_xTe$ photodiodes (12) demonstrated a direct correlation between surface leakage current and the 1/f noise current density. Figure 5 shows this correlation for the 8 to 14µm photodiodes shown in the previous figure. The correlation is given by:

$$i_f = \alpha(I_L)^\beta f^{-1/2} \qquad (13)$$

where $\alpha \approx 10^{-3}$, $\beta = 1$, and I_L is the surface G-R or surface leakage current at the diode voltage of operation.
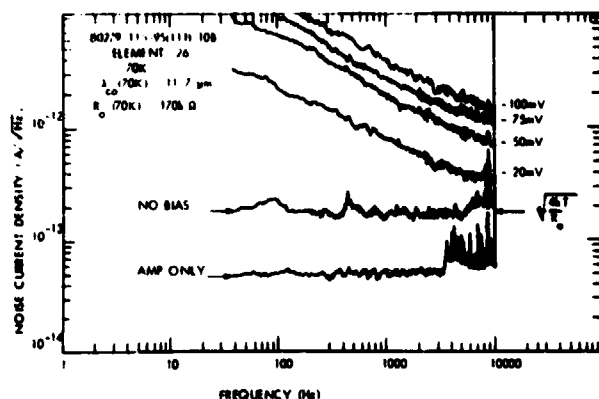

Figure 4. Noise current spectrum for a photodiode having $\lambda_{co} = 11.7\mu m$ at 70 K. The magnitude of the 1/f noise is consistent with the surface G-R associated with $S_0 = 1.7 \times 10^6$ cm/s.
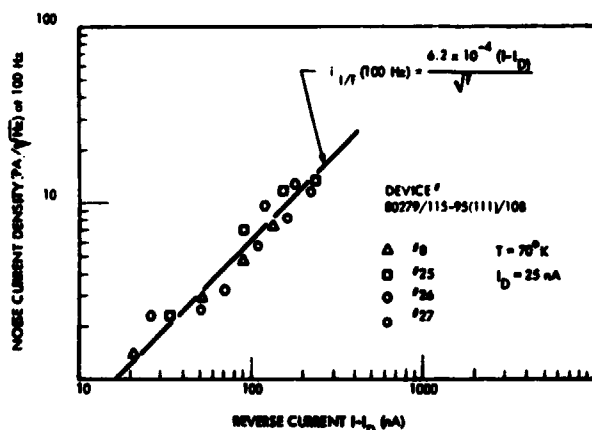

Figure 5. Linear correlation of 1/f noise with surface G-R current at 70 K for four elements of the array in Figure 4.

Figure 6 shows a typical noise current spectrum at 70 K for the small area photodiode characterized in Figures 2 and 3. No 1/f noise is observed at zero bias or even at 20 mV reverse bias. At larger reverse biases classical 1/f noise, characterized by $i_n \propto 1/f$, is evident. Such low 1/f noise is consistent with the surface G-R currents for $S_0 = 3.7 \times 10^4$ cm/s. Quantitative values for the performance parameters are given in Table I.

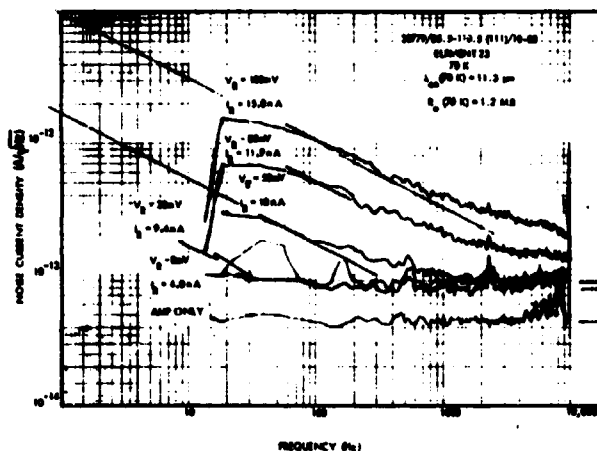Figure 6. Noise current spectrum for a photodiode having $\lambda_{co} = 11.3\mu m$ and $R_0 = 1.2M\Omega$ at 70 K. No 1/f noise is observed for -20mV bias. This low 1/f noise is consistent with the surface G-R associated with $S_0 = 4 \times 10^4$ cm/s.

Table 1

T = 70 K

ARRAYS	λ_{co} (µm)	R_0	I_s (nA)	I_0 (nA)	S_0 (cm/s)	i_n (nA/$\sqrt{Hz}$)
80279/115-95(111)100 #26	11.7	170 Ω	11	11.3	1.7×10^6	7.5
30779/60-95(111)/4-42 #1	11.0	1.3 MΩ	7.6	3.6	4.1×10^5	0.90
30779/85.5-110.5(111)/10-83 #23	11.3	1.2 MΩ	4.9	0.28	3.7×10^4	0.17

*Noise current density taken at 100 Hz and at a reverse bias of 50 mV.

IMPROVEMENTS IN SURFACE G-R

Once surface G-R was determined to be the principal G-R current source, I-V modeling was used to quantitatively determine S_0 for various processing variations. Table I shows the measured and modeled parameters at 70 K for three arrays of about the same wavelength which demonstrate successful reduction in surface G-R and associated depletion surface recombination velocity from $S_0 = 1.7 \times 10^6$ cm/s down to $S_0 = 4 \times 10^4$ cm/s. The measured 1/f noise in these arrays is reduced by almost exactly this same factor. This is consistent with the correlation of 1/f noise with surface G-R as given by Equation 13.

C-2

In conclusion, photodiode diffusion and generation-recombination currents have been unambiguously separated in $Hg_{0.8}Cd_{0.2}Te$ using the characteristic temperature dependence (R_0 vs T) and current dependence (I vs. V). The area dependence was successfully utilized to distinguish bulk G-R from surface G-R. Analysis indicated that the G-R currents in present diodes are surface in nature and described by a depletion surface recombination velocity S_0. The I-V modeling technique was used to quantitatively determine S_0 for photodiode arrays fabricated using processing variations. Reductions in S_0 from 1.7×10^6 cm/sec to 4×10^4 cm/sec were demonstrated.

Noise spectra were presented for the first time for 8-12 μm photodiodes at zero bias and under various levels of reverse bias, demonstrating the strong bias dependence of 1/f noise. A near linear correlation of the magnitude of 1/f noise with surface G-R, similar to that reported for 3-5 μm photodiodes, was shown to hold also for 8-12 μm photodiodes. The photodiodes having reduced surface G-R, and thus lower S_0, exhibited lower 1/f. The magnitude of the 1/f noise was found to scale in direct proportion to S_0, consistent with the correlation determined.

Photodiodes diffusion limited down to 65 K and having $S_0 = 4 \times 10^4$ cm/s and $\lambda_{co} = 11.3$ μm at 70 K were demonstrated. No 1/f noise was observed for reverse bias up to 20 mV. Since proper coupling of focal planes to charge coupled devices may require diode operation at even larger reverse bias, still further reduction in S_0 is needed to reduce the 1/f noise more.

REFERENCES

*   Work supported in parts by NRL Contract N00173-78-C-0145 and NV&EOL Contract DAAK70-78-0152.

1. Sood, A.K. and T.J. Tredwell, IEEE Electron Device Meeting, Extended Abstract p. 434 (1978).

2. Sood, A.K., J.W. Marciniec, and M.B. Reine, Naval Research Laboratory Final Report Contract No. N00173-78-C-0145 (1979).

3. Wang, C.C., et al., IEEE Trans. On Electron Devices ED-27, 154 (1980).

4. Sood, A.K., D.L. Polla, and R.E. Longshore, to be published (1980).

5. Sood, A.K. and S.P. Tobin, IEEE Electron Device Letters EDL-1, 12 (1980).

6. Tobin, S.P., R.J. Briggs, J.W. Marciniec, P.H. Zimmermann, A.K. Sood, and M.B. Reine, Device Research Conference, Cornell University, 23-25 June 1980.

7. Van der Ziel, A., Advances in Electronics and Electron Devices, Vol. 46, Edited by L. Marton, Academic Press (New York, 1978), p. 313.

8. Shockley, W., Bell System Tech. J. 28, (1949).

9. Sah, C.T., R.N. Noyce, and W. Shockley, Proc. IRE 45, 1228 (1957).

10. Leistiko, O., and C.A. Bittman, Sol. State Elec. 16, 1321 (1973) reported $S_0 = 10^6$ cm/s for $GaAs_{0.6}P_{0.4}$ using this technique.

11. Stringello, G.B., J. Vac. Sci. Technol. 13, 908 (1976) reported $S_0 = 5 \times 10^5$ cm/s to 1.7×10^5 cm/s for GaP using this technique.

12. Tobin, S.P., S. Iwasa, T.J. Tredwell, IEEE ED-27, 43 (1980).